UNIVERSITY OF OKLAHOMA

GRADUATE COLLEGE

SOUTH PACIFIC ATMOSPHERIC INTERNAL VARIABILITY AND ITS ROLE IN EL NIÑO-SOUTHERN OSCILLATION

A THESIS

SUBMITTED TO THE GRADUATE FACULTY

in partial fulfillment of the requirements for the

Degree of

MASTER OF SCIENCE IN METEOROLOGY

By

YUJIA YOU
Norman, Oklahoma
2018

SOUTH PACIFIC ATMOSPHERIC INTERNAL VARIABILITY AND ITS ROLE IN EL NIÑO-SOUTHERN OSCILLATION

A THESIS APPROVED FOR THE
SCHOOL OF METEOROLOGY

BY

_____
Dr. Jason Furtado, Chair

_____
Dr. Elinor Martin

_____
Dr. Michael Richman

Acknowledgements

First and foremost, I owe my deepest gratitude to my advisor, Dr. Jason Furtado, for offering me the opportunity to study at the University of Oklahoma, for his constant patience, guidance, support and encouragement throughout my master studies. I learned a lot from the numerous discussions we have had, which helped me to think in a more comprehensive way. Many thanks also go to the faculty and staff at SoM, I really enjoyed the past two years here.

My immense appreciation also goes to my undergraduate advisor, Dr. Xiaojing Jia from Zhejiang University, for teaching me the statistical methods when I was new to the climate science. In her research group, I first learned how to address research questions and think independently.

I also thank my other committee members Dr. Elinor Martin and Dr. Michael Richman, for their insightful advice and discussions on my research. Thanks also go to members of Applied Climate Dynamics Group. Although we focus on very different topics, their works broaden my horizons and develop my interests in new research areas.

Last but not least, I thank my parents, for unconditional support throughout the years and always being there.

Table of Contents

List of Tables

List of Figures

Abstract

Accurate long-range seasonal prediction of the El Niño-Southern Oscillation (ENSO) phenomenon is of critical importance to predict regional and global climate anomalies. The overarching goal of this work is to seek the extratropical precursors for ENSO events with a focus on the South Pacific. More specifically, this work investigates the impacts of the South Pacific atmospheric internal variability on the occurrence, intensity, evolution, and flavors of ENSO events in the context of the coupled atmosphere-ocean system.

In general, both the tropically forced and intrinsic atmospheric variability in the South Pacific features a large-scale meridional sea level pressure (SLP) dipole with anomalies out-of-phase between the middle and high latitudes. The dipole is termed the South Pacific Oscillation (SPO) in the present thesis. The internal component of the SPO initiates the South Pacific Meridional Mode (SPMM), which acts as an effective conduit transmitting the extratropical wind and sea surface temperature (SST) anomalies (SSTA) into the central-eastern equatorial Pacific via the wind-evaporation-SST (WES) feedback. Modulated by the seasonal cycle of the oceanic mixed layer depth and the lower amplitude of the mean seasonal cycle in the Southern Hemisphere, the WES feedback involved with the SPMM is most effective during the austral summer, providing a favorable timing for the SPMM to prime an ENSO event. The SPMM-induced anomalies in the central-eastern tropical Pacific interfere constructively or destructively with the contemporaneous western tropical anomalies driven by the North Pacific Meridional Mode (NPMM) to shape the occurrence, evolution, amplitude, and potentially the longitudinal position of the maximum SSTA associated with ENSO events. Both the Pacific meridional modes are most efficient at triggering ENSO events

when the subsurface equatorial Pacific Ocean is preconditioned with the anomalous heat content buildup. The NPMM and SPMM during the austral winter (February-May) operate as skillful predictors for the boreal winter SSTA in the Pacific basin.

Despite considerable improvements to long-lead forecasts of ENSO activity over the past decades, the model prediction of the ENSO flavor is constrained to about one-to-two season lead time. Our results indicate that the austral winter SPO appears to be a primary source contributing to uncertainty in ENSO forecasts and provides important implications for the seasonal prediction of the ensuing ENSO flavors. Specifically, the spatial structure and amplitude of the austral winter SPO are considerably regulated by atmospheric intrinsic process, which affects the strength of the South Pacific subtropical high, forces stochastic zonal wind stresses and regulates discharge of the ocean heat content in the eastern equatorial Pacific. Although the wind stress relevant to the internal variability decays rapidly, it initiates coupled instability that grows into ENSO-like structure by the Bjerknes feedback. Given that internal variability is, by definition, unpredictable even with a perfect model, the austral winter SPO might serve as a natural limit for ENSO prediction.

Collectively, the current study highlights the importance of the South Pacific atmospheric internal variability and provides potential enhancements to understand and predict ENSO events. The findings contribute to the existing literature on the connection between North Pacific and ENSO to include the South Pacific. Although this thesis primarily focuses on the interannual variability, the role of the SPMM in Pacific decadal variability and its connection to ENSO under anthropogenic climate change warrant future investigations.

Chapter 1: Introduction

1.1 ENSO Predictability

The El Niño-Southern Oscillation (ENSO) phenomenon is the leading mode of coupled variability of the tropical ocean-atmosphere system on interannual timescales (e.g., *Hoskins and Karoly* 1981; *Alexander et al.* 2002; *Barsugli and Sardeshmukh* 2002; *Liu and Alexander* 2007; *Trenberth and Smith* 2009). The warm phase of ENSO features positive sea surface temperature (SST) anomalies (SSTA) in the central-eastern tropical Pacific, weakened easterly trade winds, and a flattened equatorial thermocline. In and around the tropical Pacific, ENSO-induced teleconnections impact and alter the Walker circulation, while stationary Rossby wavetrains excited by the tropical upper-level divergence from the anomalous convection dominate the extratropical response in both hemispheres. Hence, ENSO is considered an important source for seasonal predictability of temperature and precipitation regimes worldwide. Nonetheless, seasonal climate predictions based on ENSO are subject to substantial uncertainties because of the presence of the inherently unpredictable atmospheric noise in the mid-high latitudes (e.g., *Deser et al.* 2017; *Lee et al.* 2018) and the great diversity in ENSO events (e.g., location and amplitude of the maximum SSTA; *Capotondi et al.* 2015a).

The event-to-event difference in ENSO intensity and spatial pattern is reflected in the associated tropical atmospheric heating profiles and global teleconnections (e.g., *Ashok et al.* 2007; *Weng et al.* 2009). Commonly, ENSO events are classified into two general types based on longitudinal location of the maximum tropical SSTA: eastern-Pacific (EP) and central-Pacific (CP) events (*Kao and Yu* 2009; *Kug et al.* 2009; *Yu and Kim* 2010, 2011; *Capotondi et al.* 2015a), although several studies proposed that ENSO

flavors come in a non-discrete continuum and can be considered as different combinations of the two types (e.g., *Johnson* 2013; *Karnauskas* 2013). Different terms have been used to describe the CP type, including "dateline El Niño" (*Larkin and Harrison* 2005), "El Niño Modoki" (*Ashok et al.* 2007), and "warm pool El Niño" (*Kug et al.* 2009). The EP type is also termed "cold tongue El Niño" and "canonical El Niño" (*Kug et al.* 2009). The conventional EP events appear to be a basin-wide coupling phenomenon during which the SSTA typically appear in the far eastern tropical Pacific attached to the coast of South America. On the contrary, during CP events, the SSTA extend from Baja California southwestward to the central-western equatorial Pacific and thereafter remain and amplify *in situ* (*Kao and Yu* 2009; *Kug et al.* 2009; *Yu and Kim* 2010).

Consequently, a comprehensive understanding of ENSO dynamics and its predictability is of both scientific and practical importance. Current theoretical explanations of ENSO split with regard to its predictability limit. Theories such as the delayed oscillator (*Suarez and Schopf* 1988) and the discharge-recharge oscillator (*Jin et al.* 1997) emphasize the consequences of the slowly evolving ocean dynamics and hence interpret ENSO as a self-sustained, unstable oscillatory mode with potentially highly-predictable time scales of up to 2 years. Conversely, other theories consider ENSO as a stable (or damped) mode triggered by or interacting with stochastic processes. These random disturbances, for which the decorrelation timescale is fairly short, fundamentally limit the predictability of ENSO (e.g., *Penland and Sardeshmukh* 1995; *Chang et al.* 1996; *Moore and Kleeman* 1999; *Thompson and Battisti* 2000, 2001). Moreover, when considering dynamical model predictions, despite considerable

improvements to long-lead forecasts of ENSO activity over the past decades, poor long-range seasonal forecast skill in terms of the ENSO occurrence and amplitude still exists during the boreal spring prior to an event. This poor skill is termed the "spring prediction barrier" in the literature (e.g., *Jin et al.* 2008; *Barnston et al.* 2012; *Lai et al.* 2017) and possibly arises because the boreal spring features the climatologically weakest Walker Cell and weakest tropical Pacific zonal SST gradient upon which even the smallest perturbation can rapidly intensify (e.g., *Kleeman and Moore* 1971; *Latif et al.* 1994). Additionally, the prediction of the types of ENSO remains limited to less than one-season lead time since the forecast models suffer from a common systematic bias whereby the SSTA associated with the EP ENSO shifts westward with increasing lead time (e.g., *Hendon et al.* 2009; *Zhao and Hendon* 2009).

1.2 Intrinsic ENSO Precursors

The relatively poor prediction skill of ENSO from dynamical models advocates the essential role of the atmospheric intrinsic/stochastic variability in driving ENSO variability. Note the internal variability in the current study refers to internal variability of the atmosphere that is independent of (direct) tropical Pacific forcing. Several stochastic forcings that potentially drive ENSO include westerly wind bursts (e.g., *Fedorov* 2002; *Vecchi et al.* 2000; *Chen et al.* 2015), the Madden-Julian Oscillation (e.g., *Gebbie et al.* 2007), tropical oceanic instability waves in the eastern Pacific Ocean (e.g., *An* 2008), and extratropical North Pacific atmospheric variability (e.g., *Vimont et al.* 2003a; *Chang and Vimont* 2004; *Nakamura et al.* 2006, 2007).

On time scales longer than 10 days, extratropical atmospheric circulation variability is organized into large-scale patterns driven primarily by internal nonlinear

dynamical processes (*Wallace and Gutzler* 1981; *Feldstein* 2000). These random fluctuations are white in time but not necessarily in space. Increasing observational and modeling evidence suggests that the North Pacific Meridional Mode (NPMM; Figure 1.1) acts as an effective conduit through which extratropical North Pacific atmospheric variability finally impacts the tropical Pacific (*Vimont et al.* 2001, 2003a, b; *Chiang and Vimont* 2004; *Anderson* 2007; *Chang et al.* 2007; *Alexander et al.* 2010; *Di Lorenzo et al.* 2015). Initiated by sea level pressure (SLP) variations associated with the North Pacific Oscillation (NPO; *Rogers* 1981; *Linkin and Nigam* 2008) during the boreal winter and spring, the NPMM features warm (cool) subtropical SSTA and the weakened (strengthened) trade winds during its positive (negative) phase. The NPMM evolves through a positive feedback between the wind-induced evaporation and the underlying SSTA. This thermodynamical coupling, referred to as the wind-evaporation-SST (WES) feedback (*Xie and Philander* 1994), enhances the southwestward propagation of the subtropical SSTA and wind anomalies from the North-central Pacific into the western-central equatorial Pacific in the boreal spring and early summer (i.e., the seasonal footprinting mechanism; e.g., *Vimont et al.* 2001, 2003a, b) and charges/discharges the equatorial Pacific upper ocean heat content [i.e., the trade wind charging (TWC) mechanism; e.g., *Anderson et al.* 2007; *Anderson and Perez* 2015]. Unlike ENSO, the NPMM does not require ocean dynamics explicitly for its existence. However, equatorial oceanic Kelvin waves triggered by the NPMM forcing are the fundamental mechanism responsible for further ENSO development (*Thomas and Vimont* 2016).

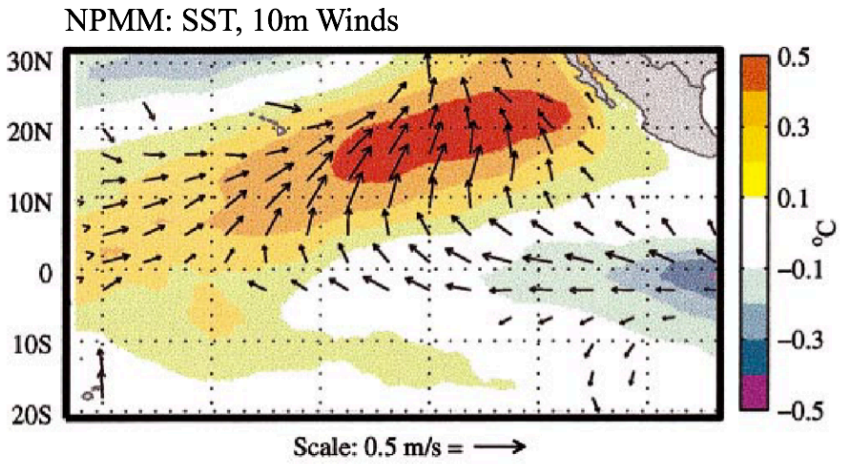

Figure 1.1 The spatial structure of the North Pacific Meridional Mode. SSTA (°C) and surface wind (m/s) fields are shown in shading and vector, respectively. Adapted from Figure 1 in *Chiang and Vimont* (2004).

The NPMM thus carries important implications for predicting the onset and occurrence of ENSO events. *Chang et al*. (2007) indicated that more than 70% of the historical El Niño events during 1958-2000 were preceded by extreme NPMM positive episodes in the boreal spring. Conversely, this fact implicitly hints that not all extreme NPMM episodes guarantee an ENSO event. *Larson and Kirtman* (2014, 2015) found large ensemble spread and little skill in ENSO forecasts using the NPMM as the sole predictor in dynamical models. Contradictory results also exist in terms of the role of the NPMM in predicting the ENSO flavors. Some studies suggest the NPMM is more effective in initiating CP ENSO events (e.g., *Vimont et al.* 2014), while other works found no such preference (e.g., *Ding et al.* 2015a; *Di Lorenzo et al.* 2015).

A plausible explanation for the ENSO prediction failure based on the NPMM is the interference between the various ENSO precursors. The antecedent and concurrent conditions in the tropical Pacific and subtropical South Pacific have been reported to interfere constructively or destructively with the NPMM-induced tropical Pacific

anomalies (e.g., *Anderson* 2007; *Alexander et al.* 2010; *Su et al.* 2014; *Min et al.* 2015). Notably, the potential influence of the South Pacific anomalies is supported by the optimal structure (OS) of ENSO events (Figure 1.2; e.g., *Penland and Sardeshmukh* 1995; *Alexander et al.* 2008). When the OS is specified as the initial condition (Fig. 1.2a), the SSTA field evolves into a mature ENSO event 7 months later (Fig. 1.2b). The OS bears strong resemblance to the NPMM structure in the North Pacific sector, but also shows a large loading in the subtropical South Pacific.

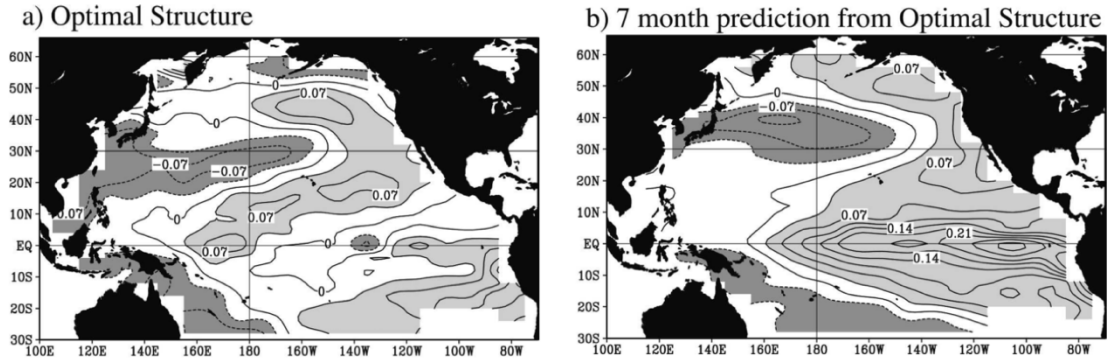

Figure 1.2 (a) The SSTA optimal structure that evolves into (b) a mature ENSO event in 7 months. Contour internal is 0.07. The units are arbitrary. Adapted from *Alexander et al.* (2008). See also *Penland and Sardeshmukh* (1995).

While previous studies focused on the *response* of the South Pacific circulation to the tropical forcing (e.g., *Mo and Higgins* 1998; *Mo* 2000; *Mo and Paegle* 2001; *Kidson and Renwick* 2002), emerging climate literature now emphasizes the *impact* of the South Pacific variability on tropical Pacific climate variability across multiple timescales, either via oceanic tunnels (*van Loon and Shea* 1985; *Luo et al.* 2003; *Tatebe et al.* 2013; *Imada et al.* 2016) or atmospheric bridges (*Matei et al.* 2008; *Okumura* 2013; *Zhang et al.* 2014a; *Ding et al.* 2015b*,* 2017; *DiNezio et al.* 2017; *Meehl et al.* 2017).

Recently, *Zhang et al.* (2014a) identified the South Pacific Meridional Mode (SPMM), for which the spatial structure is similar to OS in the South Pacific, using atmospheric general circulation (AGCM)-slab ocean models, fully coupled models, and observational datasets (Figure 1.3). In AGCM-slab ocean models, it is suggested that the South Pacific Meridional Mode (SPMM), which features SSTA in the southeastern Pacific oriented with the southeast trade winds (Fig. 1.3b) and is delineated by areal-averaged SSTA in the southeastern Pacific (i.e., their SEP index), has a stronger expression in the equatorial Pacific than the NPMM owing to the northward shift of the Intertropical Convergence Zone (*Zhang et al*. 2014b). However, the slab ocean lacks the necessary ocean dynamics required for ENSO. In fully coupled model and observation where ocean dynamics are active, obviously, one needs to disentangle the ENSO forcing from the SEP index, to bring out the unique impacts of the SPMM and the midlatitude internal variability. As shown in Figs. 1.3c-f, the SPMM structure gives more resemblance to the canonical ENSO events and the equatorward propagating feature is largely absent (not shown). The mixing is hinted by the seasonality of SEP index as well (i.e., the standard deviation of the SEP time series as a function of calendar month; Figure 1.4). The SEP is most active during the austral winter in AGCM-slab ocean models, while in coupled models and the real world it peaks in variance during the austral summer when ENSO typically matures. Therefore, under this definition, the SEP index may not be completely independent of the tropical SSTA forcing and a representative of the South Pacific extratropical internal variability in fully coupled system.

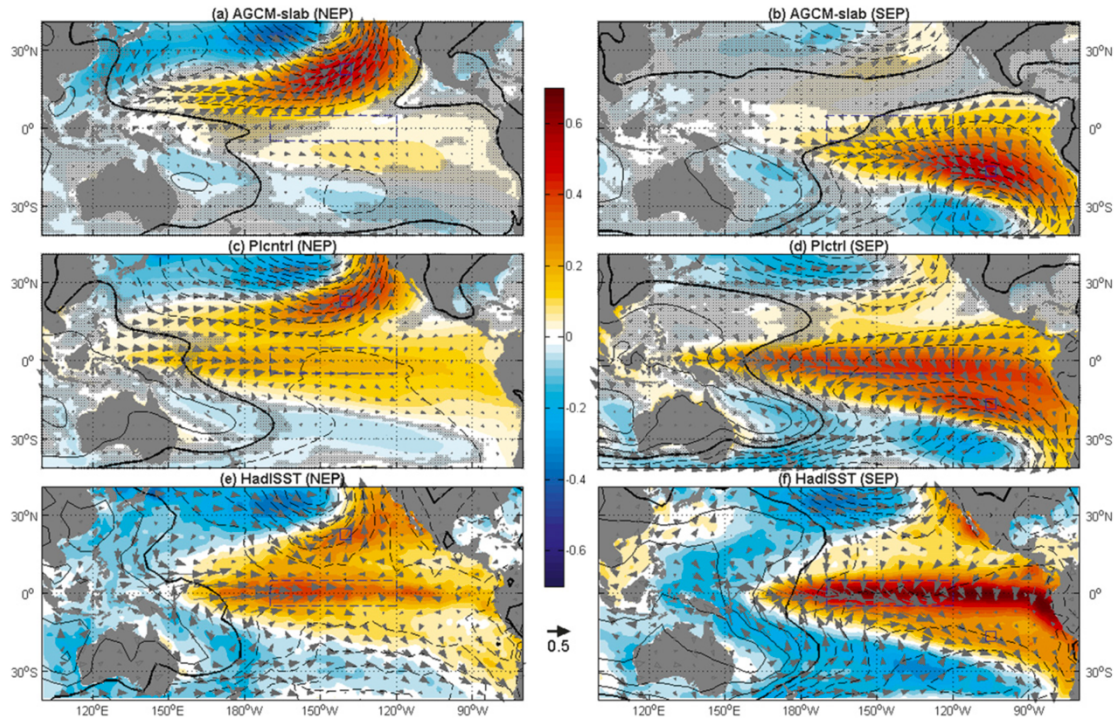

Figure 1.3 Regression of anomalous SSTA (shading), SLPA (contours), and surface winds (arrows) onto normalized SST time series averaged in the (left column) northeast (21°N-25°N, 138°W-142°W) and (right column) southeast (19°-15°S, 103°-107°W) Pacific, respectively. (a, b) The multimodel mean of 11 AGCM-slab models; (c, d) as in (a) but for the fully coupled version (preindustrial scenario), and (e, f) observation. Adapted from *Zhang et al.* (2014a).

Better understanding of how the Pacific meridional modes (PMMs) contribute to tropical Pacific interannual-to-decadal variability and how extratropical-tropical Pacific interactions will change in future climate ultimately relies on the improved simulation of PMMs by climate models (e.g., *Lin et al.* 2015; *Liguori and Di Lorenzo* 2018). Moreover, comparing and contrasting the models with reanalysis also adds fidelity to the robustness of the results and facilitates the quantification of model biases. As such, this thesis provides an additional benchmark by which to test coupled climate models for their fidelity in simulating the interannual-to-decadal Pacific variability to add to a building paradigm on the processes involved in the Pacific climate regime (e.g., *Clement et al.* 2011; *Okumura* 2013; *Di Lorenzo et al.* 2015). Hence, how the SPMM

and its connections to the tropical Pacific are simulated by the state-of-art coupled models is another focus of this thesis.

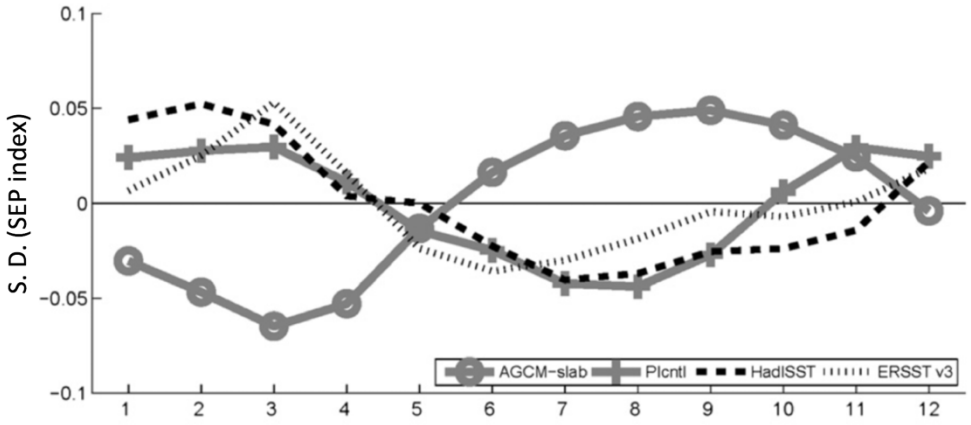

Figure 1.4 Seasonality of the SEP index in AGCM-slab models (gray lines with circles, multimodel mean), fully coupled models (gray lines with crosses, multimodel mean), and observations (Hadley Center Sea Ice and Sea Surface Temperature (HadISST) in black dashed lines and Extended Reconstructed SST version 3 (ERSSTv3) in black dotted line) expressed by the standard deviation as a function of calendar month. The mean standard deviation for all months is removed to emphasize the seasonality. Positive (Negative) values denote standard deviation exceeds (falls below) the annual mean. Adapted from *Zhang et al.* (2014a).

1.3 Outline

In general, the predictability of ENSO events relies on the existence of atmospheric or oceanic precursors preceding ENSO at some lead time. This thesis aims to explore further the South Pacific intrinsic precursor and discuss its role in ENSO variability and diversity using reanalysis and the state-of-the-art fully coupled climate models. The thesis is composed of five chapters and is organized as follows. Chapter 2 presents an overview of the major datasets and general methods common to analyses throughout the thesis. Chapter 3 focuses on the different mechanisms involved with the SPMM, how it interacts with the NPMM-induced anomalies and tropical Pacific antecedent conditions, and also tests the forecast skill of boreal winter Pacific SSTA using the PMMs in a statistical model. Chapter 4 examines the impacts of the austral

winter (i.e., June-August) South Pacific atmospheric internal variability on the development of ENSO events in both reanalysis and dynamical models used operationally for seasonal forecasting. A summary of the results and future work avenues are presented in Chapter 5.

Chapter 2: Data and Methodology

2.1 Observational Datasets

Observational datasets of atmospheric and oceanic variables used throughout the thesis are primarily from reanalysis products. For monthly-mean atmospheric fields, the National Centers for Environmental Prediction/Nation Center for Atmospheric Research (NCEP/NCAR) Reanalysis 1 (*Kalnay et al.* 1996) is utilized. The data uses a grid with horizontal resolution of 2.5° by 2.5° and spans 1948–present. Variables of interest include SLP, 10-m wind, and surface energy fluxes. SSTs over the same period are taken from the Met Office Hadley Center Sea Ice and Sea Surface Temperature (HadISST) dataset (*Rayner et al.* 2013). Subsurface ocean data come from the European Center for Medium Range Weather Forecasts (ECMWF) Ocean Reanalysis System 4 (ORA-S4; *Balmaseda et al.* 2013). In this thesis, we use the common time period among all reanalysis datasets, namely 1948–2016. Results presented are robust when using other reanalysis products [e.g., National Oceanic and Atmospheric Administration (NOAA) Extended Reconstructed Sea Surface Temperature SST v3b (Smith et al. 2008), NOAA-CIRES 20th Century Reanalysis version 2 (*Compo et al.* 2011), ECMWF 20th Century Reanalysis (ERA-20C; *Poli et al.* 2016), ERA-Interim (*Dee et al.* 2011), and Simple Ocean Data Assimilation (SODA; *Carton and Giese* 2008)]. Not only are these datasets different materially, but they also cover different time periods (e.g., ERA-Interim ranges from 1979–present and ERA-20C spans 1900-2010), indicating that our results are generally insensitive to the time period chosen for analysis.

2.2 Models

2.2.1 Coupled Model Intercomparison Project Phase 5 (CMIP5) Models

For the fully-coupled climate model employed in analyses in Chapter 3, we select monthly-mean output from twelve (12) coupled climate models from the Coupled Model Intercomparison Project Phase 5 (CMIP5; *Taylor et al.* 2012). Table 2.1 lists the models used in this study. Availability of the necessary atmospheric and oceanic model output dictated the selection of the models used in this study. Since we are interested in the inherent dynamics of the SPMM and its natural variability, we examine the pre-industrial control (piControl) experiment from CMIP5 (i.e., prescribed, non-evolving greenhouse gas concentrations and aerosols mimicking conditions prior to 1850 are the primary forcings). Because of the lack of uniform availability of surface-based winds among the models, we use 1000 hPa winds from the models as a proxy for the 10-m wind. All model oceanic and atmospheric fields from the models are regridded onto a common latitude/longitude grid using bilinear interpolation based on the reanalysis data to facilitate comparisons between models and for multi-model ensemble means. Sub-surface data are vertically interpolated onto the ORA-S4 depth coordinate, which contains 42 levels in vertical (18 of which are in the upper 200m).

2.2.2 North-American Multi-Model Ensemble (NMME) Phase-II Models

The NMME prediction system is composed of several coupled ocean-atmosphere models used to make seasonal (Phase-I) and subseasonal-to-seasonal (Phase-II) forecasts (*Kirtman et al.* 2014). The system is run in realtime but also consists of hindcasts with varying periods. These hindcasts are initialized on the first day of each month based on the observational fields and run out for one full year (365

days) to mimic the realtime forecasting process. Output available are at the sub-daily, daily-mean, and monthly-mean level.

Table 2.1 List of coupled climate models from CMIP5 analyzed in this study, along with total length of the piControl run and grid resolution (unit: degree) for each model (years). For resolution, in case of the atmospheric grid and its latitude, the tabulated resolution is only valid for the equator region. For higher latitudes deviations may occur. Ocean models have their own, finer grid. If two values are given for the latitude resolution of the ocean grid, resolution is not constant. The first value is that for the equator, the second for the poles (maximum for the two poles if different). lat(i,j) and lon(i,j) denote latitudes and longitudes defined with two indices i and j. In this case the resolution cannot simply be read out. See also the website https://portal.enes.org/data/enes-model-data/cmip5/resolution.

Institution, Country	Model acronym	Length of piControl run (years)	Atmospheric grid		Oceanic grid	
			lat	lon	lat	lon
National Center for Atmospheric Research (NCAR), United States	CCSM4	501	0.9424	1.25	lat (i,j)	lon (i,j)
Canadian Centre for Climate Modeling and Analysis (CCCma), Canada	CanESM2	296	2.7906	2.8125	lat (i,j)	lon (i,j)
Centre National de Recherches Météorologiques/Centre Européen de Recherche et Formation Avancées en Calcul Scientifique (CNRM-CERFACS), France	CNRM-CM5	850	1.4008	1.40625	lat (i,j)	lon (i,j)
Commonwealth Scientific and Industrial Research Organisation (CSIRO) in collaboration with the Queensland Climate Change Centre of Excellence (QCCCE), Australia	CSIRO-Mk3-6-0	500	1.8653	1.875	0.93, 0.95	1.875
Geophysical Fluid Dynamics Laboratory, United States	GFDL-ESM2G	500	2.0225	2	0.375, 0.5	1
National Aeronautics and Space Administration (NASA) Goddard Institute for Space Studies (GISS), United States of America	GISS-E2-R	250	2	2.5	1	1
Met Office Hadley Centre, England	HadGEM2-CC	240	1.25	1.875	0.3396, 1	1
Institute for Numerical mathematics, Russia	INMCM4	500	1.5	2	0.5	1
Atmosphere and Ocean Research Institute (The University of Tokyo)/National Institute for Environmental Studies/Japan Agency for Marine-Earth Science and Technology, Japan	MIROC5	300	1.4008	1.40625	0.5	1.40625
Institut Pierre-Simon Laplace, French	IPSL-CM5A-MR	300	1.2676	2.5	lat(i,j)	lon(i,j)
Max Planck Institute for Meteorology (MPI-M), Germany	MPI-ESM-P	550	1.8653	1.875	lat(i,j)	lon(i,j)
Norwegian Climate Centre (NCC), Norway	NorESM1-ME	252	1.8947	2.5	lat(i,j)	lon(i,j)

In this study, we employ monthly-mean output from the NMME Phase-II hindcasts over the period 1982–2010 (a common period for the models examined), with all output provided on a 1°x1° grid. As each hindcast run contains 10 ensemble members, this dataset essentially allows us to examine how atmospheric intrinsic variability impacts seasonal ENSO forecasts. Variables of interest include SLP, SST, 850 hPa winds (U_{850}; the lowest level available from all model output), oceanic subsurface temperatures (T_{sub}), and oceanic zonal (u) and vertical (w) velocity. Due to availability of all these necessary variables, only two of the NMME Phase-II models are examined in the current study: CESM1 and CanCM4 (*Merryfield et al.* 2013).

2.3 General Methodology and Statistical Techniques

This section introduces and briefly describes the main statistical techniques used throughout the thesis. For reanalysis and the CMIP5 models, data are linearly detrended first to eliminate the influence of (linear) trends on the underlying statistical and inferred dynamical relationships among variables. Monthly anomalies are obtained by subtracting the climatological annual cycle at each grid point. A 3-month running mean is applied to all fields prior to analysis.

2.3.1 Linear Regression and Composite Analysis

Linear regression used to describe the linear relationship between two time series, herein x[t] and y[t], can be written as:

$$\mathrm{y} = \hat{\mathrm{y}} + \epsilon = \mathrm{b}_0 + \mathrm{b}_1 * \mathrm{x} \tag{2.1}$$

The regression procedure chooses the regression coefficients (i.e., b_0 and b_1) which minimize the mean square error for predictions of y given observations of x:

$$\mathrm{b}_0 = \overline{\mathrm{y}} - \mathrm{b}_1\overline{\mathrm{x}} \tag{2.2}$$

$$b_1 = \frac{\sum_{i=1}^{n}(x_i - \bar{x})(y_i - \bar{y})}{\sum_{i=1}^{n}(x_i - \bar{x})^2} \tag{2.3}$$

where the overbar denotes means. b_1 represents the slope of the linear relationship, which describes the *y* change per unit of change in *x*. If *x* is normalized, then the unit of b_1 are the unit of *y* per standard deviation in *x*.

Furthermore, the fraction of the total variance of *y* explained by *x* can be measured by the square of the correlation coefficient *r*:

$$r = \frac{\sum_{i=1}^{n}(x_i - \bar{x})(y_i - \bar{y})}{\sqrt{\sum_{i=1}^{n}(x_i - \bar{x})^2 \sum_{i=1}^{n}(y_i - \bar{y})^2}} \tag{2.4}$$

The statistical significance of the linear relationship can be evaluated by a two-sided Student's *t* test with an effective degrees of freedom N^* computed as in *Bretherton et al.* (1999), i.e.,

$$t = \frac{r\sqrt{N^* - 2}}{\sqrt{1 - r^2}} \tag{2.5}$$

$$N^* = \frac{1 - r_1 r_2}{1 + r_1 r_2} \tag{2.6}$$

where *N* is the total sample size and r_1 and r_2 are the lag-1 autocorrelations of the index and field used in the particular analysis, respectively.

In general, how the variable *y* linearly evolves with respect to *x* can be assessed by simultaneous and lagged regressions. For instance, many ENSO-induced climate anomalies are, to first order, linear. Particularly, over the Pacific sector, ENSO impacts can be largely accounted for with linear wave theory and simple ray tracing in the troposphere (e.g., *Hoskins and Karoly* 1981; *Horel and Wallace* 1981; *Sardeshmukh and Hoskins* 1988; *Trenberth et al.* 1998). The variability of SSTA averaged over the tropical Pacific strip is commonly represented by the cold tongue index (CTI), defined

as the areal-averaged SSTA in 6°S~6°N and 180°~90°W (e.g., *Deser and Wallace* 1990). Thus, the variability of three-dimensional field *Y*[x, y, t] independent of the tropical SSTA forcing can be isolated by linearly regressing out the contemporaneous CTI from each grid point, i.e.,

$$\mathrm{Y[x,y,t]_{internal}} = \mathrm{Y[x,y,t]} - \mathrm{b[x,y]} * \mathrm{CTI[t]} \tag{2.7}$$

where $\mathrm{b[x,y]}$ is the regression coefficient of the CTI onto field Y.

While regression analysis is based on the assumption that the relationship between two time series is largely linear, composite analysis is not limited to this constraint. Composite in this study is implemented as follows. Suppose we want to investigate the linkage between an index *x*[t] and three-dimensional field variable *Y*[x, y, t]. Events are selected based on the values of the standardized index x such that we can define positive (sample size: n_1) and negative (sample size: n_2) extreme events based on the standardized index *x*. We then isolate the signal in *Y* associated with *x* by calculating the difference of the average of *Y* between the positive ($\overline{Y}_1$) and negative ($\overline{Y}_2$) key times. Finally, the Student's *t* test is employed to check whether the two composite samples are statistically significant different from each other:

$$\mathrm{t} = \frac{\overline{\mathrm{Y}}_1 - \overline{\mathrm{Y}}_2}{\sqrt{\frac{(\mathrm{n}_1-1)\mathrm{S}_1^2+(\mathrm{n}_2-2)\mathrm{S}_2^2}{\mathrm{n}_1+\mathrm{n}_2-2}\left(\frac{1}{\mathrm{n}_1}+\frac{1}{\mathrm{n}_2}\right)}} \tag{2.8}$$

where S_1 and S_2 denote the sample variance of *Y* in the positive and negative events, respectively.

2.3.2 EOF and MCA

Empirical Orthogonal Function (EOF; *Wilks* 2006) analysis and Maximum Covariance Analysis (MCA; *Bretherton et al.* 1992) are the two matrix methods applied

to the reanalysis and model output fields to extract the leading modes of variability/co-variability in the atmospheric and oceanic fields investigated in this thesis. EOF analysis is a statistical technique used to identify the principal (spatially orthogonal) modes of variability of a given field. The covariance matrix of the field is constructed and diagonalized, resulting in a set of eigenvalues and corresponding eigenvectors. Each eigenvector can be regarded as a spatial pattern (i.e., EOF). The temporal evolution of the spatial pattern is represented by the time series obtained by projecting the eigenvector onto the original field (i.e., the principal component (PC) time series).

By comparison, MCA is usually applied to the covariance matrix of the two data fields in order to identify pairs of coupled spatial patterns that explain as much as possible the covariance between the two variables. The MCA of the cross-covariance matrix yields two spatially uncorrelated sets of singular vectors (i.e., left and right singular vectors analogous to the EOFs, but one for each variable), with the first set of patterns representing the leading mode of co-variability between the fields, the second set as the second leading mode of co-variability, etc. Each pair of singular vectors describe a fraction of the squared covariance between the two variables. Temporal variations in each of the fields are represented with expansion coefficient time series, produced by projecting anomalies of the left (or right) field onto the leading mode of that same field. These time series are analogous to the PC time series from EOF analysis except (a) there are two sets of time series, one for each field and (b) successive expansion coefficient time series for the same field are not mutually orthogonal. Note that as EOF is applied to each field separately and the MCA is applied to the covariance matrix between two fields, the significance of the atmosphere-ocean

interaction is revealed by a strong resemblance between individual EOF and MCA modes of SSTA and SLPA. As the time series obtained by EOF and MCA has arbitrary amplitude and is dimensionless, a convenient way to present the information is by regressing the original data onto standardized values of the respective time series. For MCA, this can be accomplished either through homogeneous (i.e., regressing the left (right) field onto the right (left) expansion coefficient time series) or heterogeneous (i.e., regressing the left (right) field onto the right (left) expansion coefficient time series) regression. The spatial pattern that emerges then has units of the original data and illustrates a pattern of (co-)variability in the dataset.

Chapter 3: The South Pacific Meridional Mode and its role in the El Niño-Southern Oscillation[1]

3.1 Background and Motivation

As discussed in the Introduction, the Pacific meridional modes (PMMs) link extratropical atmospheric and oceanic anomalies to the tropical Pacific. The key physical mechanism involved with the PMMs - i.e., the wind-evaporation-SST (WES) feedback (*Xie and Philander* 1994), contains three different processes (Figure 3.1): (1) wind variations generate changes in sea surface evaporation (Fig. 3.1b), (2) surface evaporation alters the underlying SST (Fig. 3.1b), and (3) the resulting SST anomalies produce atmospheric circulation anomalies (Fig. 3.1c).

Consequently, the excitation of tropical Pacific climate variability by the PMMs is regulated by the seasonality of both midlatitude atmospheric variability and the atmosphere-ocean coupled response. For example, for the NPMM, the NPO peaks in strength during the boreal winter (*Rogers* 1981; *Linkin and Nigam* 2008) with the response of the underlying SST to the NPO-induced wind stress forcing maximizing in the boreal spring (*Vimont et al.* 2009). Taken together, the NPMM is therefore most energetic in the boreal winter/spring and thus influences the onset of ENSO events. Indeed, when the NPMM is artificially suppressed in model simulations during boreal winter/spring, the simulated ENSO substantially weakens and is no longer phase-locked to the seasonal cycle (e.g., *Chang et al.* 2007).

[1] Work in this chapter is currently under revision in *J. Climate*: You, Y., and J. C. Furtado, 2018a: The South Pacific Meridional Mode and its role in the ENSO variability and predictability. *J. Climate*., in revision.

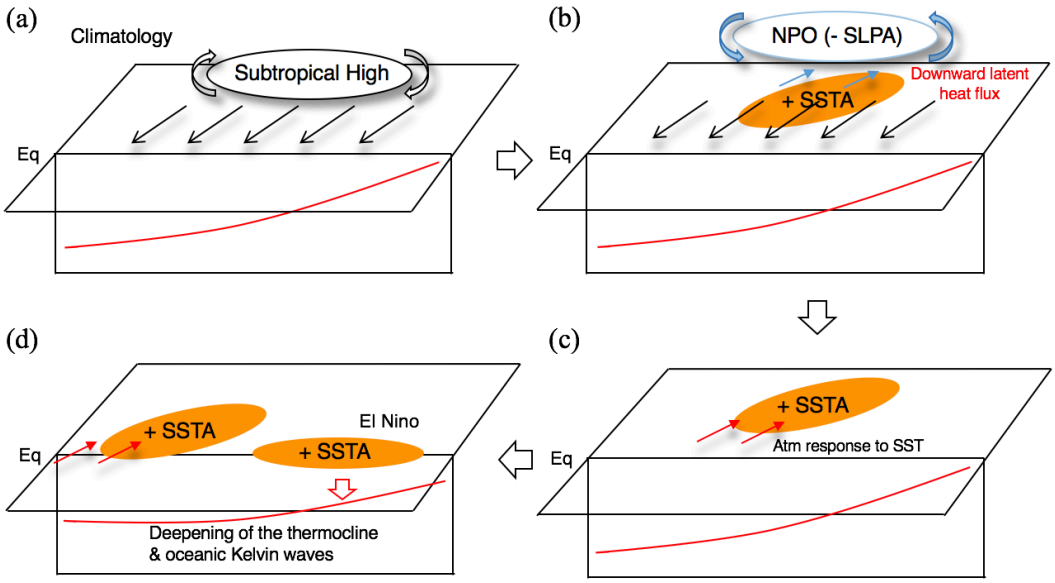

Figure 3.1 Schematic plot of how the NPMM may trigger ENSO events. (a) SLP and low-level wind climatology in the tropical and subtropical North Pacific. (b) The positive phase of the boreal winter NPO represents a weakened North Pacific subtropical high, thereby weakening the trade winds. The weakened trade winds suppress the ocean evaporation, imposing downward latent heat flux and warm underlying SSTA. (c) The NPO after boreal winter. In responses to the positive SSTA footprint and the WES feedback, an anomalous atmospheric circulation resembling the NPO-induced wind anomalies forms in the southwestern side of the SSTA footprint. (d) The subtropical anomalies propagate southwestward into the western-central tropical Pacific. The anomalies then trigger downwelling Kelvin waves to deepen the thermocline depth in the far eastern tropical Pacific and thus give rise to the onset of an El Niño event.

Hence, seasonality is of great importance when considering the role of PMMs in ENSO formation and variability. If the SPMM is akin to its northern counterpart in case of the seasonality, then we may speculate that the contribution of the SPMM to the onset of ENSO events could be trivial. Instead, several studies have documented the unique influences of the austral summer South Pacific atmospheric and oceanic variability on ENSO (e.g., *McGregor et al.* 2009a, b; *Ding et al.* 2015b; *Min et al.* 2017). In this chapter, we explore the characteristics of the SPMM in the context of coupled atmosphere-ocean system and illustrate the different mechanisms involved with

the SPMM relative to the NPMM. Results also show the role of South Pacific extratropical stochastic forcing in the various aspects of ENSO events (e.g., regulating the occurrence, evolution, amplitude, and flavors of ENSO). This work contributes to our growing understanding of how the South Pacific atmosphere and ocean interact with the tropical Pacific for multi-scale climate variability. This chapter is organized as follows. Section 3.2 documents the reanalysis datasets, model outputs, and the statistical methods employed in this study. Section 3.3 and 3.4 characterize the SPMM and its linkages with the large-scale circulation variability in both reanalysis and climate models. Section 3.5 then presents the influences of SPMM on the tropical Pacific climate, its interactions with the NPMM and tropical preconditions, and evaluates the prediction skill of a developed statistical model for the boreal winter Pacific SSTA. Discussion and conclusions of this chapter follow.

3.2 Data and Methods

In this work, we use many of the reanalysis products and CMIP5 models detailed in Chapter 2 of this thesis. In additional to the variable already mentioned, subsurface potential temperature data come from the ECMWF ORA-S4 are used to determine the 20°C isotherm (Z_{20}), a proxy for tropical thermocline depth in the tropical Pacific. Additionally, we use the Z_{20} to calculate a measure for ocean heat content, the warm water volume (WWV), defined as the depth of Z_{20} over 5°S~5°N and 120°E~80°W (e.g., *McPhaden* 2003).

To better equate and compare model statistics with the reanalysis products, we subdivide the output of each CMIP5 model into 70-year segments and then compute the necessary statistics and quantities on those 70-year segments. The model-mean is then

computed as the average of the statistics among the several sub-intervals. Finally, the multi-model ensemble (MME) mean is computed by averaging a particular statistic over all of the models, with uncertainty denoted by the unit standard deviation amongst the ensemble members.

Several statistical methods are used in this study. EOF and MCA are employed to study the variability and co-variability of atmospheric and oceanic fields, respectively (see Chapter 2). Correlation and regression are also used in this study. For observations, the significance testing for the temporal correlation and regression is done through a two-sided Student's *t* test. For the models, the significance for the regression maps is defined when at least 9 out of 12 models have the same sign as the ensemble-mean.

Lag-correlation is commonly used to identify potential precursors of a given variable (e.g., y correlates with x_1 at a certain time lag). However, other climate processes (e.g., a process x_2) may intervene with x_1 to augment/offset its relationship with y. For this purpose, we consider the variation of the correlation between x_1 and y conditioned on x_1 and x_2: i.e., $corr\_diff(x_2) = corr\ (x_1, y \mid x_1 * x_2 > 0) - corr\ (x_1, y \mid x_1 * x_2 < 0)$. Whether x_2 significantly modulates the correlation of x_1 with y is evaluated through a Monte Carlo resampling technique. For the Monte Carlo testing, we generate 10,000 normally-distributed synthetic time series (x_P) with identical length, mean, and variance as x_2 and calculate the probability density function (PDF) of $corr\_diff\ (x_P)$. The significance is then represented by the probability that $corr\_diff\ (x_2) > corr\_diff\ (x_P)$. For the models, which have a much larger sample size, we generate 70-yr x_1, x_2, y, and x_P time series randomly to produce PDFs of $corr\_diff\ (x_2)$ and $corr\_diff\ (x_P)$,

respectively. A two-tailed Kolmogorov-Smirnov goodness-of-fit test is applied to compare the two PDFs and test if they are significantly different from each other.

3.3 Characteristics of the SPMM in Reanalysis

3.3.1 Spatial Structure of the SPMM

In this study, we define the SPMM in reanalysis following the methodology of Chiang and Vimont (2004) for meridional modes – i.e., the leading MCA mode (MCA-1) of SST and 10-m wind anomalies in the subtropical South Pacific sector (35°S-10°S, 180°-70°W). Note that our domain excludes the tropical Pacific SSTA and winds to highlight the extratropical processes associated with the SPMM. Furthermore, as ENSO teleconnections are seasonally dependent, we linearly remove the contemporaneous CTI month by month from the fields prior to MCA to isolate the internal variability. The SPMM accounts for 54.1% of the total coupled variance and is significantly distinguished from higher modes based on a Monte Carlo test. Figure 3.2 summarizes the spatiotemporal features of the SPMM. In the positive phase, a northeast-southwest SLPA dipole exists between the subtropical and higher latitudes with a nodal point near 50°S (Fig. 3.2a). The northern pole of the SLPA dipole modulates the strength of the South Pacific subtropical high and therefore the climatological southeasterly trade winds, generating anomalous latent heat fluxes into the underlying ocean (Fig. 3.2a, black contours). Associated with the change in the trade winds and latent heat flux anomalies, a SSTA dipole extending toward the central-eastern equatorial Pacific forms in the subtropical South Pacific. The lag-correlation peaks when the wind expansion coefficient time series (EC-1_{wind}) leads the SST expansion coefficient time series (EC-1_{SST}) by one month ($r = 0.54$; $p < 0.05$; Fig. 3.2b), suggesting the atmosphere drives the

ocean. Intriguingly, contrary to the NPMM (*Chiang and Vimont* 2004), the month-to-month variance of the EC-1_{wind} and EC-1_{SST} indices evolve out of phase; i.e., the SST variance maximizes during austral summer while the wind variance peaks during austral winter (Fig. 3.2c).

The SPMM possesses variability ranging from seasonal to interannual and longer timescales (Fig. 3.2d), indicating that this intrinsic mode may have implications on Pacific climate variability across multiple timescales. Further comments on this multi-scale variability are reserved for the last section. Following previous studies (e.g., *Vimont* 2003a, b; *Chiang and Vimont* 2004; *Chang et al.* 2007), we use the EC-1_{wind} to delineate the SPMM in the remainder of this paper. The anomalous wind field associated with the SPMM is closely related to the mechanism needed for the generation of oceanic Kelvin waves (*Thomas and Vimont* 2016) and contains information about the atmospheric intrinsic variability as well as the feedbacks from the underlying ocean. While the SSTA field may be affected by the ENSO nonlinearity (*Chiang and Vimont* 2004). Thus, the SPMM index represents variability in the extratropical South Pacific atmosphere and ocean system. Note that changes in the analysis technique [e.g., computing the SPMM by removing the first *two* leading principal components (PCs) of the tropical Pacific SSTA prior to MCA and reasonable changes in the domain size (150°E-70°W, 5°N-45°S)] yield similar results (not shown).

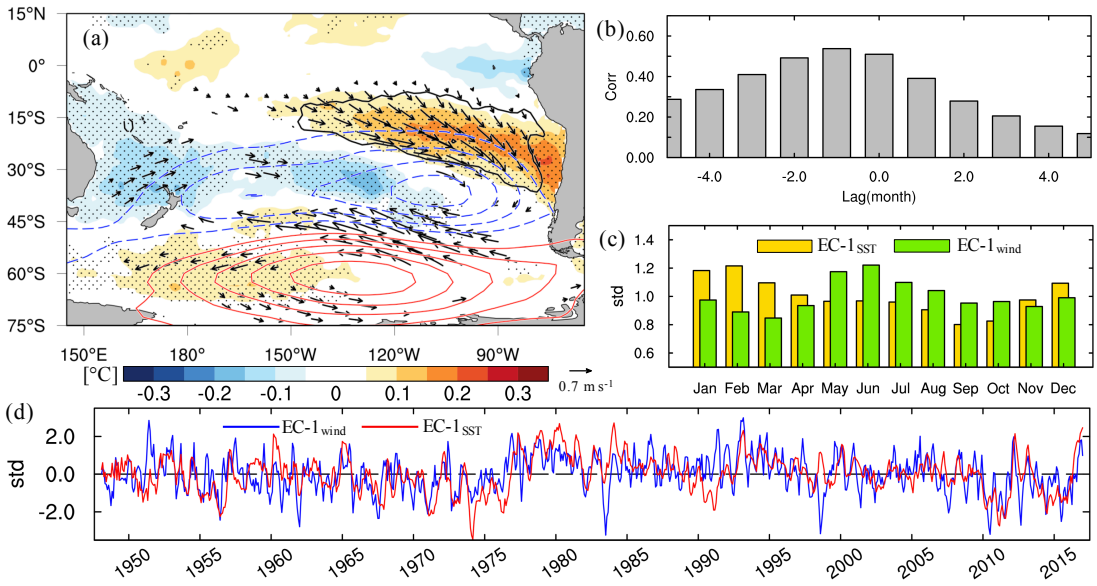

Figure 3.2 (a) Regressions of the monthly-mean SSTA (shading, °C), SLPA (blue/red contour, hPa), 10-m wind anomalies (vector, m/s) and net surface latent heat flux (black contour, W/m^2) onto the standardized monthly-mean EC-1$_{wind}$ index. Negative (positive) latent heat flux anomalies indicate anomalous heat flux into (out of) the ocean. Contour interval 0.4 hPa (blue/red line contours) and 5 W/m^2 (black contours). Reference wind vector 0.7 m/s. Positive (negative) values represented by solid (dashed) contours; zero contour omitted. Stippled areas indicate significance of SSTA at 95% level according to a two-tailed Student's *t* test. Only significant wind vectors are drawn. (b) Lag correlation between EC-1$_{wind}$ and EC-1$_{SST}$ indices (see text for details). Negative (positive) lags indicate that the EC-1$_{wind}$ leads (lags) the EC-1$_{SST}$ index. (c) The month-to-month standard deviation of the EC-1$_{wind}$ (green bars) and EC-1$_{SST}$ (yellow bars) indices. (d) The standardized EC-1$_{wind}$ (blue line) and EC-1$_{SST}$ (red line) time series.

Where does the SPMM originate, and how it is excited? To address these questions, we examine EOFs of the atmospheric and oceanic fields separately (Figure 3.3). The leading SLP (SLP-1) and SST (SST-1) modes capture 49.3% and 41.5% of the total variance respectively and are significantly distinguished from higher-order modes per the *North et al.* (1982) criteria. SLP-1 features a north-south pressure seesaw (Fig. 3.3a), similar to that in Fig. 3.2. A similar SLPA structure emerges (albeit weaker) with the SLPA structure associated with SST-1 (Fig. 3.3b). Although both modes are significantly correlated with tropical Pacific SSTA, the two single-field EOF spatial

maps share similarities with the SLPA and SSTA fields associated with the SPMM outside of the equatorial Pacific.

To further isolate the intrinsic variability in the extratropical South Pacific, we repeat the above EOF analysis but this time the CTI is linearly removed month by month from the field prior to EOF analysis. The leading residual SLPA (SLP_{res}-1; Fig. 3.3c) and SSTA (SST_{res}-1) modes (Fig. 3.3d) account for 46.0% and 25.5% of the residual variance respectively and are significantly separated from higher order modes per the *North et al.* (1982) criteria. Given similarities between the SLP-1 (SST-1) and SLP_{res}-1 (SST_{res}-1) in both the SLPA and SSTA fields outside of the tropical Pacific strip, the tropically-forced and internal components of South Pacific climate variability project onto a similar spatial pattern. Differences between the subtropical SLPA, surface wind anomaly, and SSTA patterns in the residual EOF regression fields (Figs. 3.3c-d) and those from the SPMM are minimal (Fig. 3.2a). The lag correlation between the EC-1_{wind} and the SLP_{res}-1 (SST_{res}-1) indices peaks at a lag of 0 (1) month [r = 0.92 (0.54); Fig. 3.3e], suggesting that the SPMM operates as a conduit connecting the large-scale extratropical South Pacific SLP variations to the SST field.

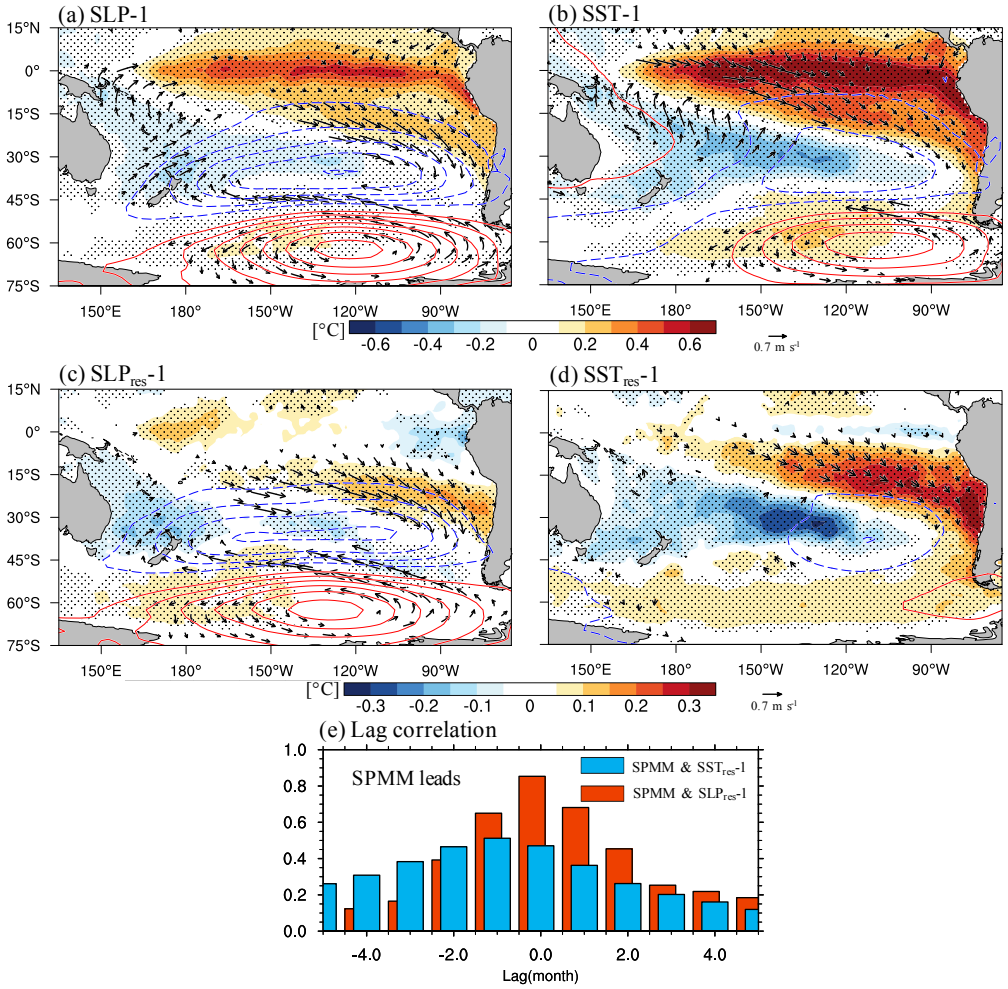

Figure 3.3 Regression of monthly-mean SSTA (shading, °C), SLPA (blue/red contour, hPa), and 10-m wind anomalies (vector, m/s) onto (a) the standardized SLP-1, (b) SST-1, (c) SLP_{res}-1 and (d) SST_{res}-1 indices (see text for details). Contour interval 0.4 hPa. Reference wind vector 0.7 m/s. Only significant (p<0.05) wind vectors are plotted. Stippling same as Fig. 3.1a. (e) Lag correlation between the SPMM and SST_{res}-1 indices (blue) and the SPMM and SLP_{res}-1 indices (red). Negative (positive) lags indicate the SPMM leads (lags) the other index.

3.3.2 Seasonality of the SPMM in Reanalysis

The spatiotemporal characteristics of the observed SPMM align well with the NPMM except that the EC-1_{wind} and EC-1_{SST} indices vary out of phase (Fig. 3.2c). To understand the physical process responsible for the out-of-phase seasonality, Figure 3.4a displays the month-to-month correlation between the EC-1_{wind} and EC-1_{SST}.

Although the MCA is designed to extract coupled modes of variability, the coupling strength experiences a distinct seasonal cycle. The contemporaneous correlation peaks during the austral summer ($r \sim 0.7$) rather than the austral winter ($r \sim 0.4$), despite wind anomalies being largest (and more variable) during the austral winter months (Fig. 3.2c; green bars). As such, factors other than the latent heat fluxes must be considered for shaping the seasonality of the SPMM SSTA field.

The spatial structures of the positive phase of the SPMM during austral summer (Fig. 3.4b) and winter (Fig. 3.4d) indicate that in both seasons, the southeasterly trade winds weaken, and anomalous latent heat fluxes enter the ocean. However, although the latent heat flux anomalies are generally stronger in magnitude during June - August (JJA; Fig. 3.4d) than during December - February (DJF; Fig. 3.4b), the JJA SSTA response is minimal over the eastern subtropical South Pacific (i.e., maximum SSTA loading center of the SPMM; Fig. 3.4d). Looking at the subsurface temperatures over the SSTA loading center (i.e., red box in Figs. 3.4b, d), the deeper mixed layer depth (MLD) during JJA appears to reduce the SSTA sensitivity to surface heat flux anomalies (Fig. 3.4e) compared to the shallower mixed layer during DJF (Fig. 3.4c). Therefore, we hypothesize that the seasonality of the MLD dictates why maximum SPMM impacts occur during austral summer rather than winter.

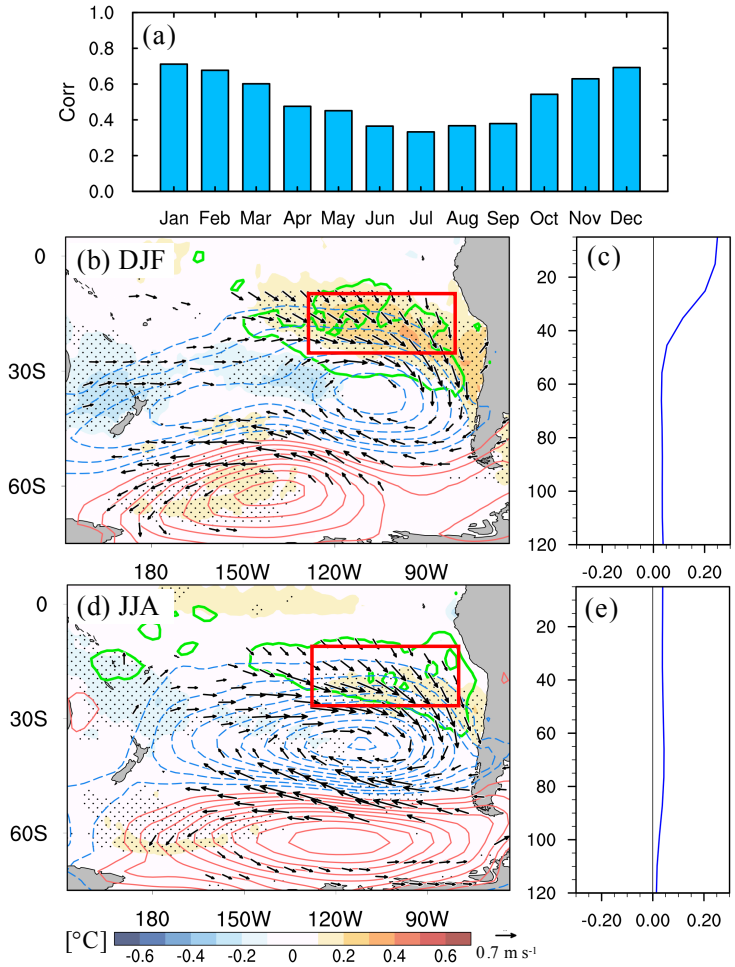

Figure 3.4 (a) Month-to-month correlation between the EC-1$_{wind}$ and EC-1$_{SST}$ indices from reanalysis. (b) Same as Fig. 1a, except for December-February (DJF). Line contour interval 0.4 hPa (blue/red contours) and 5 W/m^2 (green contours). Reference wind vector 0.7 m/s. (c) Regression of DJF ocean potential temperature anomalies (°C) as a function of depth averaged over 10°S~25°S, 130°W~80°W (red box) onto the SPMM index. (d) As in (b) but for June - August (JJA). (e) As in (c) except for JJA.

To quantitatively evaluate the effect of the MLD seasonal cycle on the SPMM, we consider the heat budget equation for the mixed layer over the red box:

$$\rho_0 c_p \int_0^{MLD} \frac{\partial T}{\partial t} = Q_{net} + Q_{ocn} = Q_{total} \tag{3.1}$$

$$Q_{net} = Q_{latent\ heat} + Q_{sensible\ heat} + Q_{shortwave\ radiation} + Q_{longwave\ radiation} \tag{3.2}$$

$$Q_{ocn} = -\rho_0 c_p \int_0^{MLD} (u\frac{\partial T}{\partial x} + v\frac{\partial T}{\partial y} + w\frac{\partial T}{\partial z})dz \tag{3.3}$$

where ρ_0 = 1020 kg/m^3 is the density of seawater, c_p = 3900 J/(kg K) is the specific heat capacity of sea water, $\partial T/\partial t$ is the tendency of the mixed layer temperature (a proxy for SST), Q_{net} is the net (radiative and non-radiative) atmospheric heat flux, and Q_{ocn} is the convergence of ocean heat transport. Here, the MLD is defined as the depth where the ocean temperature is 0.5°C less than the climatological SST (e.g., *Kara et al.* 2000). Additionally, the growth rate of the SPMM is determined by linearly regressing select variables in the heat budget equation onto the normalized monthly-mean SPMM index for each month. The contribution of various terms in (3.2) to Q_{net} (Figures 3.5a and 3.5b) highlights the dominance of the latent heat flux, which peaks during JJA when the surface wind anomalies are of largest magnitude (Fig. 3.5d). Q_{ocn} contributes minimally throughout the year (Fig. 3.5a) and hence inserts negligible influences from ocean dynamics on the growth of the SPMM. Because of the deeper mixed layer during the cold season, SSTA increase fairly rapidly from January-May and grow more slowly from JJA (Fig. 3.5c). Therefore, the South Pacific MLD likely plays an essential role in regulating the effectiveness of the air-sea coupling processes and the WES feedback associated with the SPMM. This behavior differs from the dynamics associated with the NPMM, in which both SSTA and wind anomalies peak in the late boreal winter and early boreal spring (*Chiang and Vimont* 2004; *Vimont et al.* 2009). Although the MLD and surface wind experience similar seasonality in the region affected by the NPMM, the amplitude of the mean seasonal cycle in the Southern Hemisphere is lower than the Northern Hemisphere owing to the weaker continental effects on the meridional temperature gradient (e.g., *Kiladis and Mo* 1999; *Cai and Watterson* 2002).

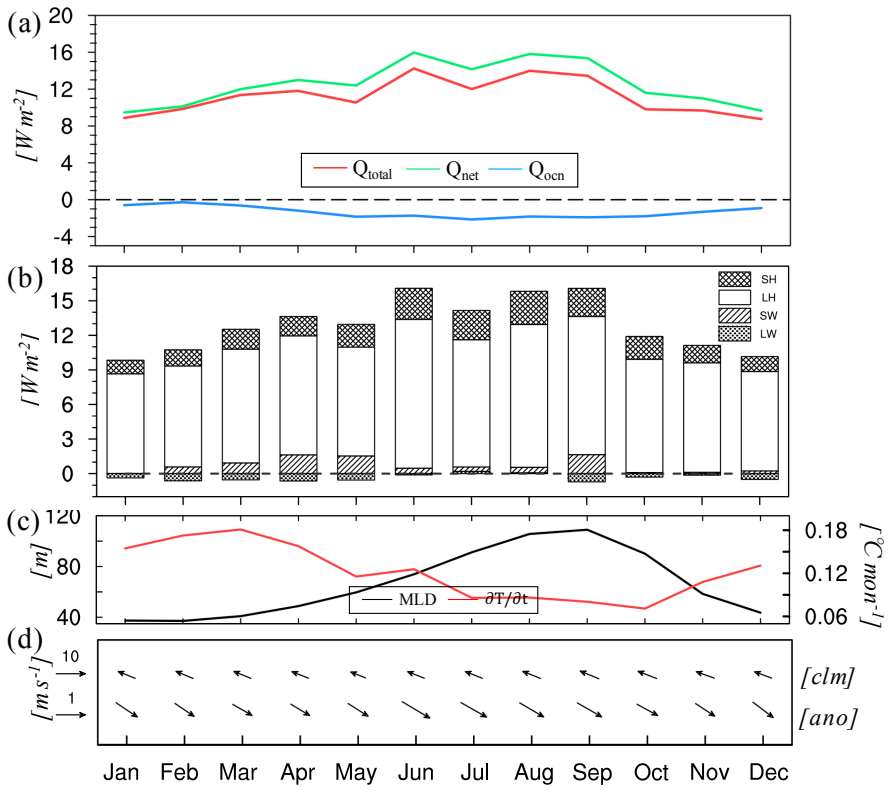

Figure 3.5 (a) Month-to-month regression of net atmospheric heat flux (Q_{net}, positive values indicate fluxes into the ocean; green line; W/m^2), convergence of ocean heat transport (Q_{ocn}, positive values indicate convergence; blue line; W/m^2) and the total heat flux (Q_{total}; red line; W/m^2) onto the SPMM index. Terms are averaged over 10°S~25°S, 130°W~80° (i.e., red box in Fig. 3). (b) Breakdown of the net atmospheric heat flux (W/m^2) regression term by month: sensible heat flux (SH), latent heat flux (LH), shortwave radiation flux (SW) and longwave radiation flux (LW). (c) Climatological mixed layer depth (MLD; black line, m) and vertically-averaged temperature tendency ($\partial T/\partial t$; red line; °C/month), calculated from the ocean heat budget equations (see text). (d) Climatological (upper vector; m/s) and anomalous (lower vector; m/s) 10-m winds within the same region. Reference vectors given and are different between climatological and anomalous winds.

3.4 The SPMM in CMIP5 Models

Given the close relationship between the SPMM and ENSO, we suggest that coupled models should have a reasonable SPMM simulation in order to exhibit realistic ENSO behavior. Hence, we next examine how well the multi-model ensemble (MME) of twelve CMIP5 models replicate the observed SPMM features. Due to the lack of observations in the South Pacific before the satellite era, the additional output from

hundreds of years of model simulations would also test the robustness of our findings from the relatively short reanalysis period. Nevertheless, when applying the same MCA procedure from Fig. 3.2 to model outputs, several CMIP5 models produce erroneous and unfamiliar patterns (e.g., CCSM4, CSIRO-MK-3-6-0, NorESM1-ME; Figure 3.6). Here, we therefore adopt a different approach to elucidate the mechanics and characteristics of the SPMM in the CMIP5 models. Instead of conducting MCA on the model fields, the anomaly fields of each model (after linearly removing the CTI from the fields) are *projected* onto the observed SPMM-related anomalous wind and SST patterns (i.e., Fig. 3.2a). Hence, the SPMM index (i.e., the time series of the anomalous low-level wind field onto the observed SPMM wind pattern) obtained in this manner represents low-level wind variability from the models that correspond to the observed SPMM structure. As such, our evaluation of the models will rely on their ability to replicate observed temporal variability and the associated physical processes associated with the SPMM.

Figure 3.7a presents the MME-mean SPMM pattern obtained by averaging the individual regression maps of the various fields onto the SPMM index for each model. The spatial pattern of the MME-mean SPMM bears strong resemblance to that from reanalysis (Fig. 3.2a) and the SPMM-like pattern also emerges in the residual EOF of the SLPA and SSTA fields, as expected from our methodology. Temporal statistics of the simulated SPMM also follow those from reanalysis, particularly the out-of-phase seasonality between the wind and SST fields (Figs. 3.7b-c). As such, the strongest (weakest) air-sea coupling in the MME occurs during DJF (JJA) (Figure 3.8a) regulated by the shallower (deeper) the MLD (Figs. 3.8c, e). The ocean heat budget in the models

reaffirms our hypothesis on the role of the MLD in modulating the WES feedback (Figure 3.9). However, the SSTA growth rate in the models is approximately half of that in reanalysis (compare Figs. 3.5c and 3.5c), possibly resulting from the overall weaker heat flux anomalies (Fig. 3.9b) compared to reanalysis (Figs. 3.9b).

Overall, the inconsistency in the leading MCA pattern (Figure 3.6) along with the deficiency in the SSTA growth rate is in need of further investigations, in particular, as to whether this is a result of a poor representation of the South Pacific atmospheric intrinsic variability or the air-sea coupling process caused by biases in background mean state (*Zhang et al.* 2014b) warrants further investigations but is beyond the scope of this paper. Despite these differences, the CMIP5 models are capable of capturing the physical processes in line with the observed SPMM, facilitating further analyses of the SPMM-ENSO relationship in the CMIP5 models.

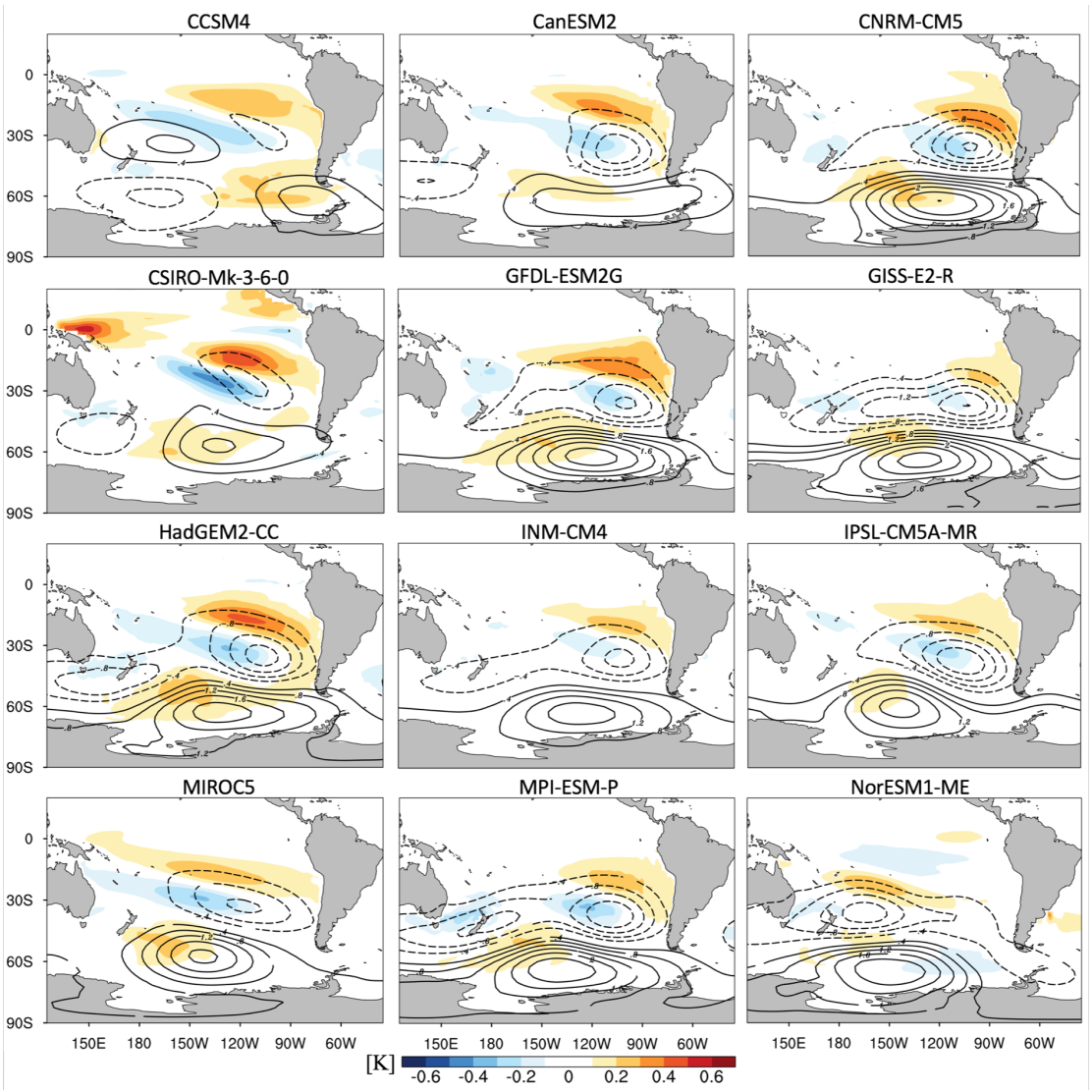

Figure 3.6 Regression maps of the monthly-mean SSTA (shading, °C), SLPA (black contour, hPa) onto the standardized monthly-mean EC-1_{wind} for each individual model. The EC-1_{wind} is obtained by MCA similar to Fig. 3.2a.

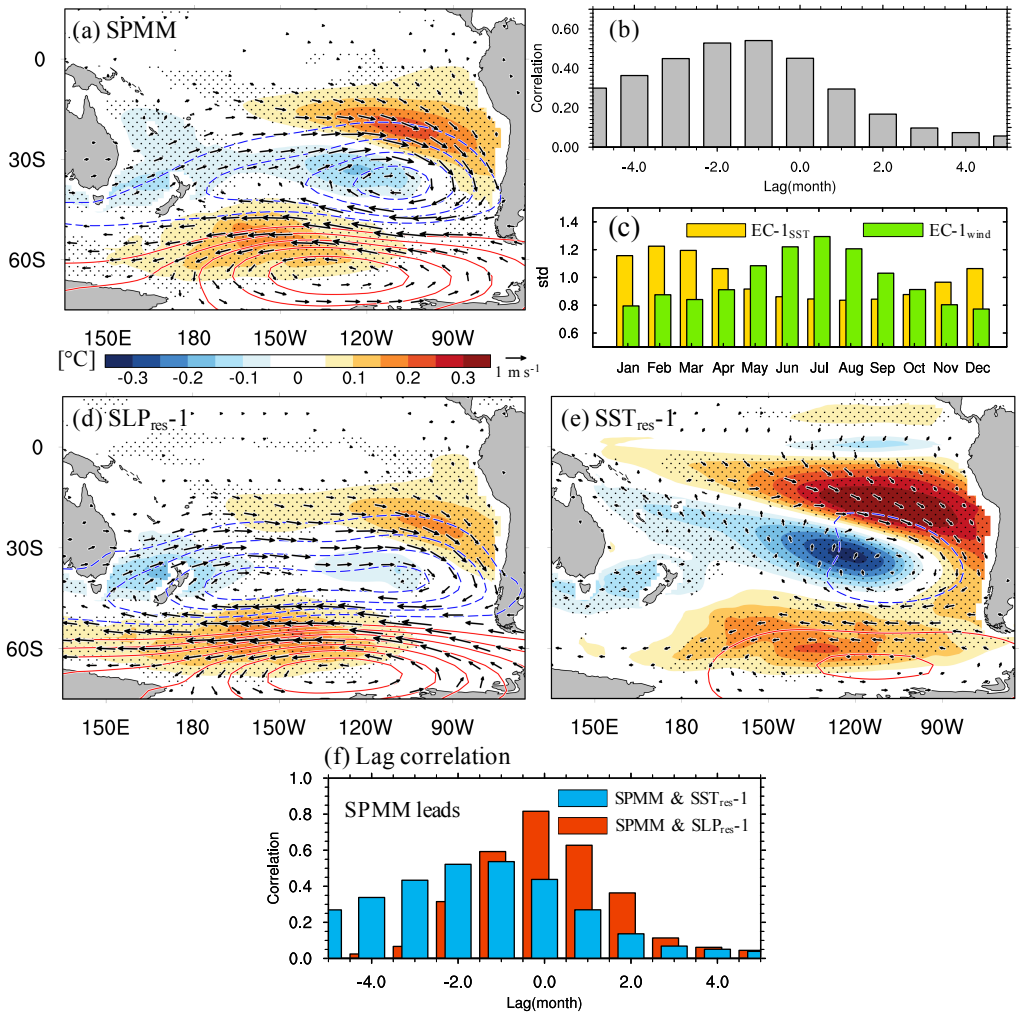

Figure 3.7 (a) The CMIP5 MME regression map of the monthly SSTA (shading, °C), SLPA (blue/red line contours, hPa), 10-m wind anomalies (vector, m/s) and net surface latent heat flux (black contour, W/m^2) onto the standardized SPMM index. Negative (positive) latent heat flux values refer to heat fluxes into (out of) the ocean. (b) As in Fig. 1b but for the CMIP5 MME. (c) As in Fig. 1c but for the CMIP5 MME. (d) As in (a) but regression of the fields onto the SLP_{res}-1 index. (e) As in (a) but regression onto the SST_{res}-1 index. (f) As in Fig. 2e but for the CMIP5 MME. Contour interval 0.4 hPa (colored contour lines) and 4 W/m^2 (black contour lines) for (a), (c), and (d). For all contours, positive (negative) values are solid (dashed) contours; zero contours omitted. Reference wind vector 1.0 m/s. Stippled areas indicate significance of SSTA when at least 9 out of 12 model have the same sign. Only significant wind vectors are drawn.

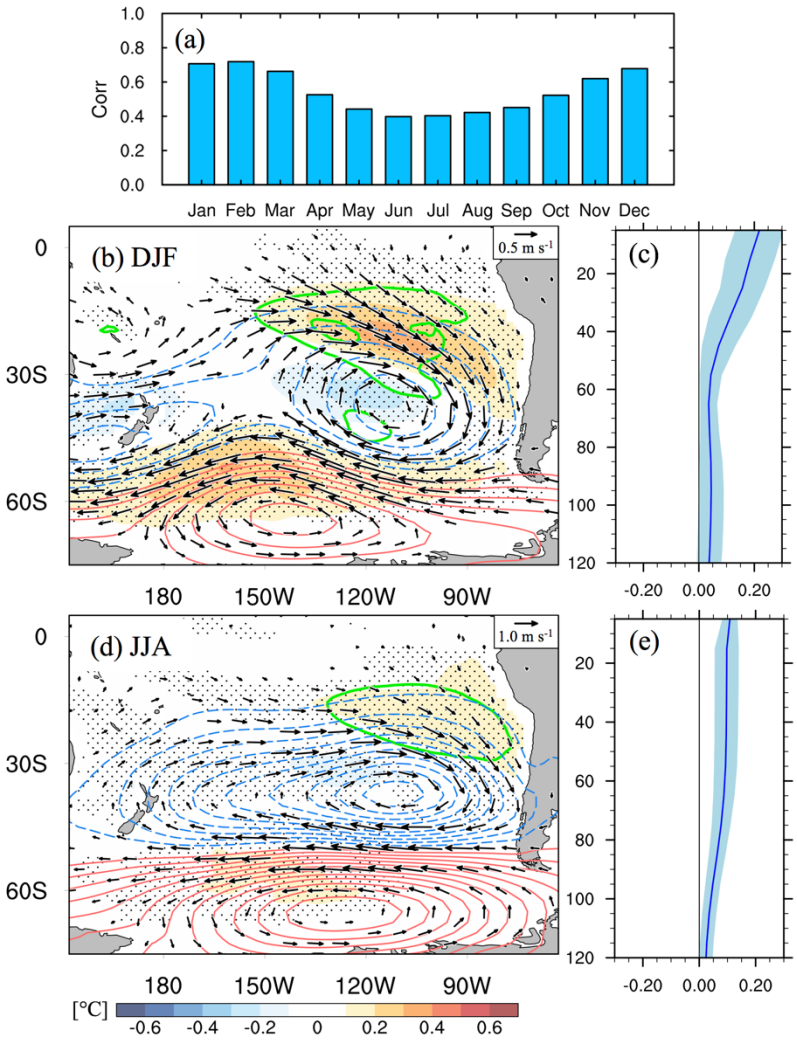

Figure 3.8 As in Fig. 3.4, but for the CMIP5 MME. (b) Line contour interval 0.2 hPa (blue/red contours) and 2 W/m^2 (green contours). Reference wind vector 0.5 m/s. (d) Line contour interval 0.2 hPa (blue/red contours) and 4 W/m^2 (green contours). Reference wind vector 1.0 m/s. Shading in (c) and (e) indicate the unit standard deviation across the models.

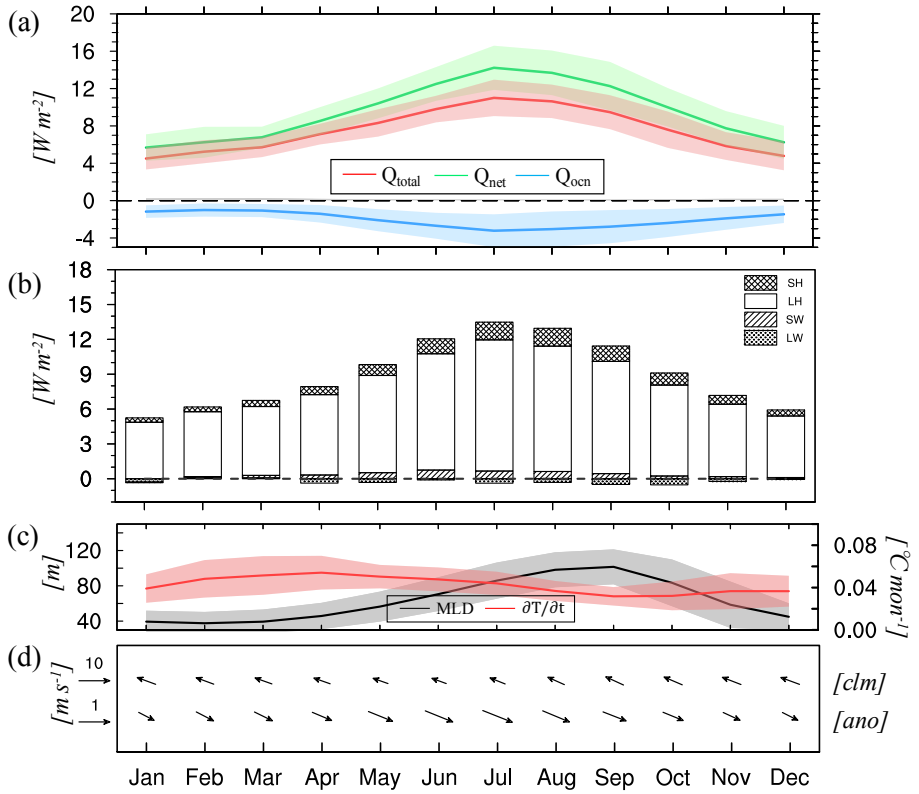

Figure 3.9 As in Fig. 3.5, but for the CMIP5 MME. Shading in (a) and (c) indicate the unit standard deviation across the models.

3.5 Linking the SPMM to Tropical Pacific Climate Variability

As discussed in Section 3.1, ENSO theories present different predictability limits for the phenomenon. In this section, we assess the roles of the PMMs versus the slowly-evolving tropical Pacific heat content for predicting ENSO events. In particular, we look to challenge the spring predictability barrier plaguing ENSO predictability studies through using both the NPMM and the SPMM. As we will show, the SPMM and South Pacific climate variability aids in extending ENSO predictability back into the boreal spring before the event.

To address this question, Figure 3.10 depicts the seasonal evolution of the Pacific atmosphere and ocean via linear regression onto the February-May (FMAM)

SPMM index ($SPMM_{FMAM}$) in reanalysis (Figs. 3.10a-d) and the MME (Figs. 3.10e-h). Here, the $SPMM_{FMAM}$ is defined EC-1_{wind} of the FMAM fields similar to that in Fig. 3.2 (Fig. 3.2d). During February-April (FMA), the SPMM-induced southeastern Pacific anomalous low-level winds and SSTA propagate northwestward into the equatorial central-eastern Pacific via the WES feedback (Figs. 3.10a-b). This perturbation triggers oceanic Kelvin waves that suppress the thermocline in the eastern tropical Pacific and promote the Bjerknes feedback that intensifies the equatorial Pacific SSTA (Figs. 3.10b-d). The CMIP5 MME mean replicates this SPMM-related evolution but with reduced magnitude (Figs. 3.10e-h). The $SPMM_{FMAM}$ index and the following winter's CTI [NDJ(+1); $CTI_{NDJ(+1)}$] are significantly correlated in both reanalysis ($r = 0.50$, $p < 0.05$; Fig. 3.11c) and in the CMIP5 MME ($r = 0.31$; Fig. 3.11g). These correlation values are comparable in magnitude to the well-identified NPMM[2] precursor ($r = 0.51$; $p < 0.05$ in reanalysis; $r = 0.31$; $p < 0.05$ in the CMIP5 MME; Figs. 3.11b, f). As such, the SPMM appears to play an important role in tropical Pacific SSTA variability in a way comparable to the more well-known NPMM pathway.

[2] The NPMM is defined as the MCA-1 of the monthly SSTA and 10-m wind anomalies over 21°S-32°N and 175°E-95°W after linearly removing the CTI from the fields (*Chiang and Vimont 2004*).

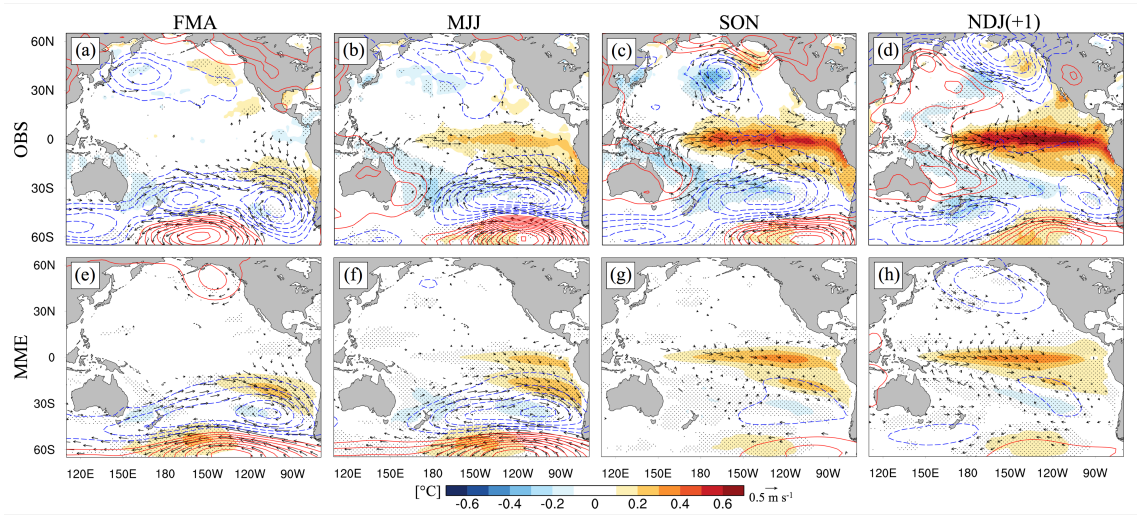

Figure 3.10 Lag-regression of (a) February-April (FMA), (b) May-July (MJJ), (c) August-October (ASO), and (d) November-January [NDJ(+1)] SSTA (shading, °C), SLPA (blue/red contour, hPa) and surface wind anomalies (vector, m/s) from reanalysis onto the $SPMM_{FMAM}$ index. (e)-(h) Same as (a)-(d) but for the CMIP5 MME. Stippling denote significance of the SSTA regression coefficients at the $p < 0.05$ level (see text for details). Line contour interval 0.2 hPa. Reference vector 0.5 m/s. Stippling indicates where the SSTA regression coefficients are statistically significant ($p<0.05$ for reanalysis; 9 out of 12 models have the same sign of the regression for the CMIP5 models).

3.5.1 Contribution of the PMMs to ENSO Diversity

Since the two PMMs are contemporaneously independent of each other (r = 0.16 in observations, r = 0.03 in MME; Figs. 3.11a, e), we next investigate how different combinations of the two phases of the PMMs (i.e., positive or negative) contribute to ENSO diversity. Here the positive (negative) phase of the PMM indicates the atmospheric and oceanic circulation patterns that favor warm (cold) ENSO events.

As shown in Figs. 3.11b-c, although the NPMM and SPMM are significantly correlated with tropical Pacific SSTA, these relationships are *conditional* - that is, they depend on the phase and amplitude of the other PMM. Specifically, when the PMMs are both positive or both negative, lagged correlations of each mode with the $CTI_{NDJ(+1)}$ are enhanced ($r \sim 0.6$ for reanalysis; $r \sim 0.5$ for the MME; Figs. 3.11b, c, f, g). However,

when the PMMs are of the opposing sign relative to each other, the lagged correlation between each PMM mode and the $CTI_{NDJ(+1)}$ drops considerably. We note, however, the change in the correlation is greater for SPMM (*corr_diff* = 0.65; $p < 0.05$) than NPMM (*corr_diff* = 0.32, $p < 0.05$; see histogram insets in Figs. 3.11b, c) in reanalysis. This is different from the CMIP5 MME where the correlation change is similar for both the NPMM and SPMM (*corr_diff* ~ 0.3, $p < 0.05$; Figs. 3.11f, g). These significant changes in the correlation of either PMM with tropical Pacific SSTA suggest that this conditional relationship merits consideration for understanding and predicting tropical Pacific variability.

The above argument is also supported from the perspective of ENSO events. To illustrate this, we plot the histogram of the $CTI_{NDJ(+1)}$ values as a function of the conditional phases of the PMMs: NPMM and SPMM of the same sign (two cases) and the NPMM and SPMM of opposite sign (two cases; Figs. 3.11d, h). The subdivisions here are done solely based on the sign of the PMMs and not on their amplitude, as we wish to preserve as many samples as possible for the histograms. For reanalysis (Fig. 3.11d), except for a few cases, more than 75% of the strongest El Niño and La Niña episodes occur when the two PMMs are of the same sign; i.e., both positive (negative) for extreme El Niño (La Niña) episodes (Fig. 3.11d). Similarly, more than 50% of the weak events ($|CTI_{NDJ(+1)}| < 1°C$) occur when the PMMs are of opposite sign.

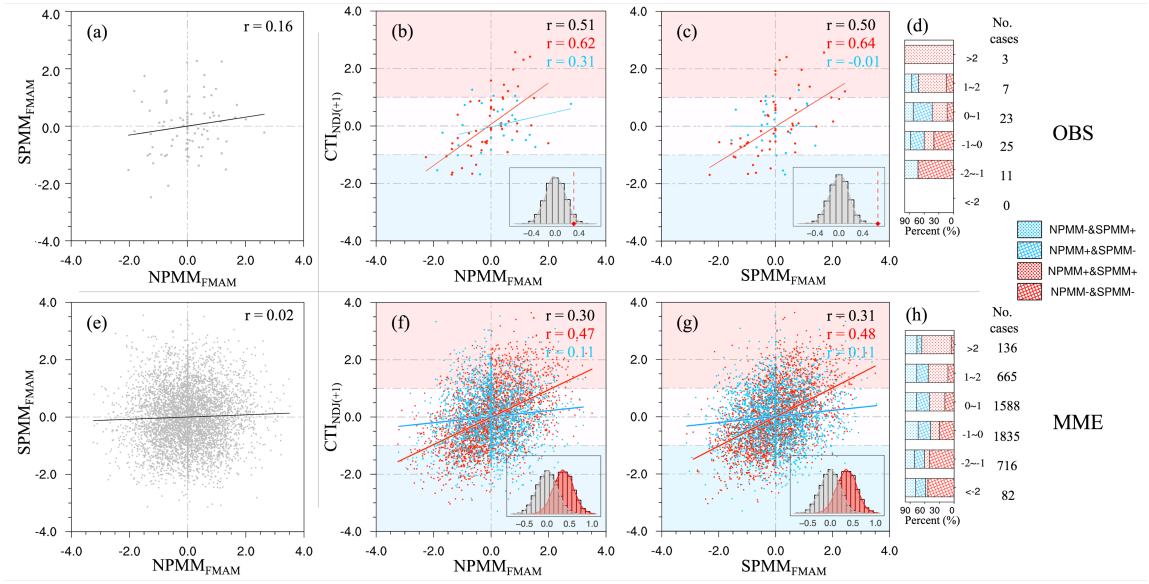

Figure 3.11 (a) Scatter plot of the $NPMM_{FMAM}$ vs. $SPMM_{FMAM}$ from reanalysis. Least-squares best fit line and correlation included. (b) Scatter plot of $NPMM_{FMAM}$ vs $CTI_{NDJ(+1)}$ from reanalysis. Red (blue) dots represent years when the $NPMM_{FMAM}$ and $SPMM_{FMAM}$ are of the same (opposite) sign. Threshold values for each case shown with the red and blue background shading. Corresponding colored lines denote the least squares fit line of the respectively-colored dots. Correlation for all points (black) and the conditional correlations for each case (red and blue) included. Inset shows the PDF of the difference in correlation coefficients between the same-signed and opposite-signed conditional correlations (i.e., red and blue; see text for details). Red dot denotes the correlation difference (i.e., red minus blue). (c) As in (b) but for the $SPMM_{FMAM}$ vs. $CTI_{NDJ(+1)}$. (d) Histogram of frequency (%) of $CTI_{NDJ(+1)}$ values for same-signed and opposite-signed NPMM/SPMM pairings (corresponding legend on far right). Total samples in each bin included. (e)-(h) As in (a)-(d) but for the CMIP5 models. For insets in (f) and (g), gray (red) PDFs represents *corr_diff*(*SPMM*) [*corr_diff*(*NPMM*)] (see text for details).

In the models, this relationship is generally reproduced (Fig. 3.11h), though the proportion of the extreme events explained by the same-signed PMMs is lower than what we find in reanalysis. One reason, of course, is the thousand-fold difference in sample size between the models and reanalysis, which factors into this wider distribution. Thus, the reanalysis results may be too separated because of the limited event numbers. Another reason for this difference between reanalysis and the CMIP5 MME is more dynamical - i.e., the models systematically underestimate of the impact of the PMMs on tropical Pacific variability, which will be discussed further shortly.

To examine how tropical Pacific variability evolves when the PMMs are of opposite sign, the conditional regression - i.e., the lag regression of atmospheric and oceanic fields onto the $SPMM_{FMAM}$ ($NPMM_{FMAM}$) index but only for times when the two PMMs are of the opposite sign (i.e., blue dots in Fig. 3.11) is applied. Figure 3.12 shows the seasonal evolution of the Pacific atmosphere and ocean related to these conditional regressions in the reanalysis (Figs. 3.12a-h) and the CMIP5 MME (Figs. 3.12i-p). During FMA, the PMMs produce their characteristic SSTA footprints in their respective hemisphere, along with modulating the strength of the trade winds (Figs. 3.12a and b). Since the thermocline feedback is hampered by the opposing anomalous wind stress forcing in the equatorial Pacific introduced by the opposite-signed PMMs, the generation and subsequent eastward propagation of oceanic Kelvin waves are suppressed, limiting SSTA growth and damping the Bjerknes feedback critical for ENSO development (Figs. 3.12b, f). Thus, the tropical Pacific SSTA remain almost unchanged spatially throughout the period (Figs. 3.12d, h). These results reaffirm our findings shown in Fig. 3.12 that skillful prediction of ENSO relies on knowing the state of both PMMs. Moreover, note that when the NPMM is accompanied by an opposite-signed SPMM, the tropical SSTA excited the NPMM forcing remain confined to the central tropical Pacific, resembling CP ENSO conditions (Fig. 3.12d). Conversely, a canonical EP-type ENSO develops when the two PMMs are in the same phase (Figure 3.13). As such, not only does the SPMM play a role in tropical Pacific dynamics, but it may also contribute to the flavor of the resulting ENSO event (i.e., CP or EP ENSO).

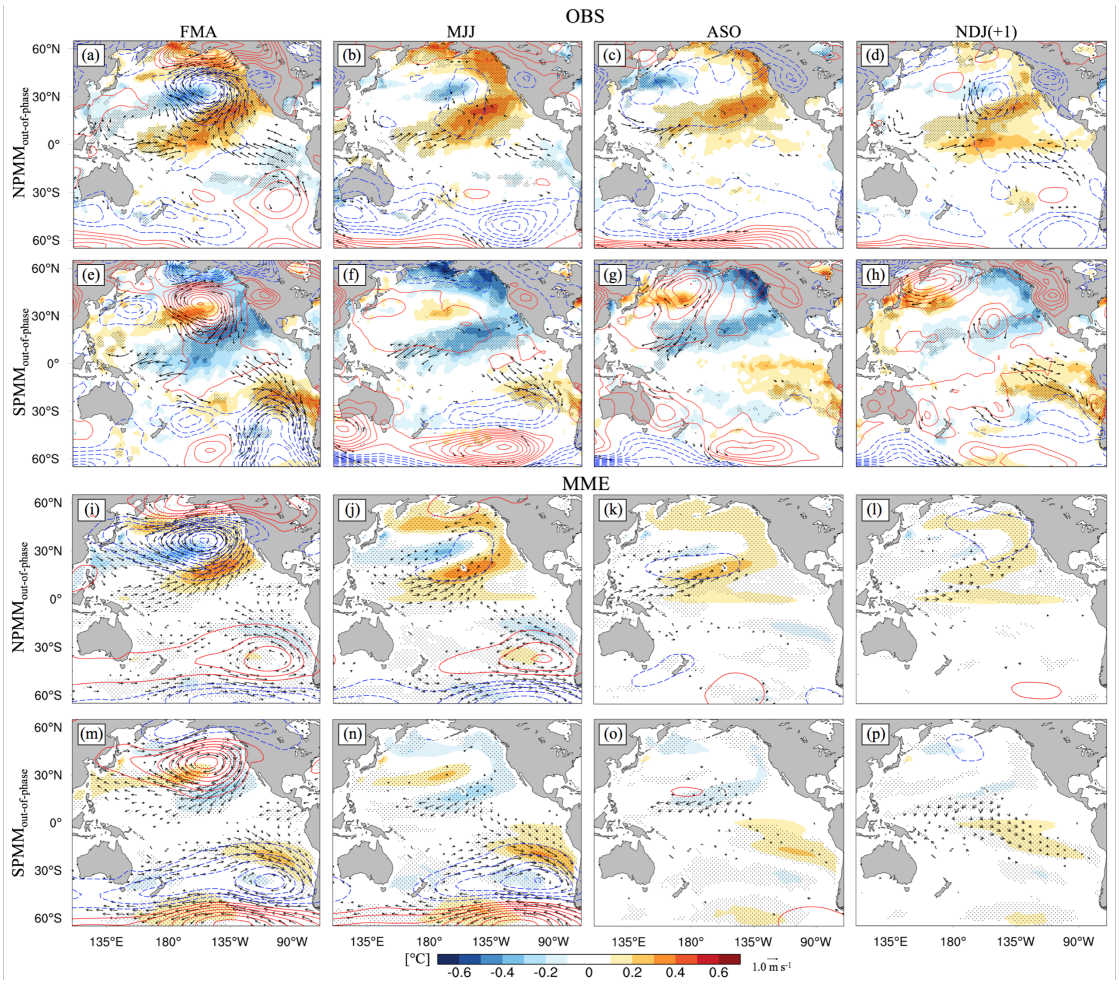

Figure 3.12 (a)-(d) Lag-regression of observed (a) February-April (FMA), (b) May-June (MJJ), (c) August-October (ASO), and (d) November-January [NDJ(+1)] SSTA (shading, °C), SLPA (blue/red contour, hPa) and surface wind anomalies (vector, m/s) onto the standardized $NPMM_{FMAM}$ index under the condition that the $NPMM_{FMAM}$ and $SPMM_{FMAM}$ indices are of the opposite sign. (e)-(h) As in (a)-(d) but regressed onto the $SPMM_{FMAM}$ index. (i)-(l) Same as (a)-(d) but for the CMIP5 MME. (m) – (p) As in (e)-(h) but for the CMIP5 MME. Line contour interval 0.2 hPa. Reference vector 1.0 m/s. Stippling indicates where the SSTA regression coefficients are considered significant ($p < 0.05$ for reanalysis; 9 out of 12 models have the same sign of the regression for the CMIP5 models).

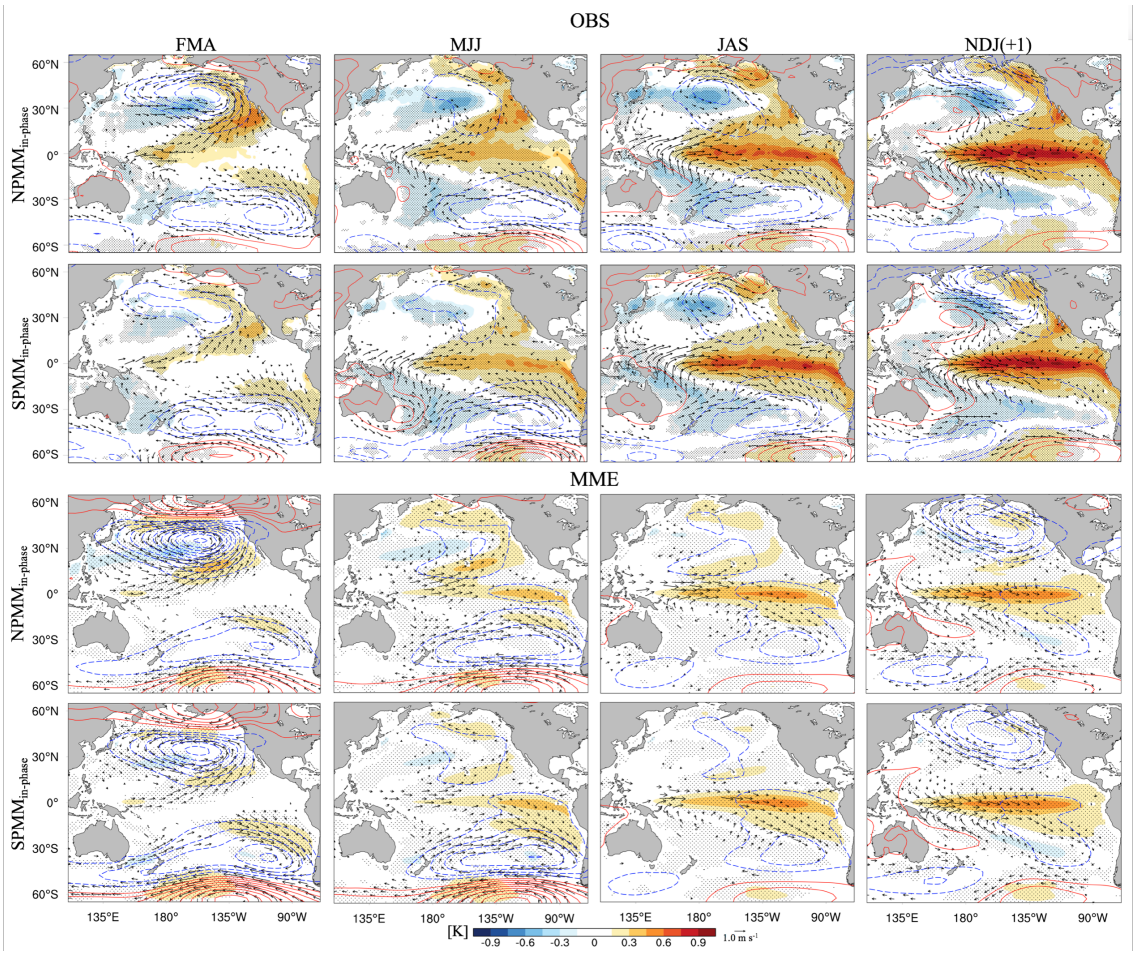

Figure 3.13 As in Fig. 3.12 except under the condition that the $NPMM_{FMAM}$ and $SPMM_{FMAM}$ are of same sign.

The CMIP5 MME yields similar evolutions during FMA and May-July (MJJ; Figs. 3.12i-j, 3.12m-n) as the reanalysis. However, differences emerge thereafter and especially during the peak season of ENSO [i.e., NDJ(+1)]. For the NPMM accompanied by opposite-signed SPMM, the SSTA span the entire equatorial Pacific strip (Fig. 3.12l), unlike the central Pacific ENSO-like conditions seen in reanalysis (Fig. 3.12d). For the SPMM accompanied by opposite-signed NPMM, the equatorial Pacific strip is nearly devoid of any positive SSTA (Fig. 3.12p). Models' deficiency in simulating the flavors of ENSO likely factors into this MME results (e.g., *Kim et al.*

2012), suggesting caution should be used when studying predictability or projections of ENSO activity using these models.

3.5.2 Sensitivity of PMMs' Influence on ENSO Variability Compared to WWV

Inherent to the recharge oscillator theory (*Jin et al.* 1997), the upper ocean heat content, which leads ENSO by a quarter cycle, is often considered a necessary precondition to the development of an ENSO event (e.g., *Meinen and McPhaden* 2000; *McPhaden* 2003; *Larson and Kirtman* 2013). Consistent with previous studies (e.g., *Anderson* 2007; *Deser et al.* 2012), we next explore the sensitivity of the PMMs' influence on the tropical Pacific to that of the upper ocean heat content, represented here by WWV.

Figure 3.14 is like Fig. 3.11 except this time considering the conditional relationship between each PMM and WWV. Here, positive (negative) WWV values indicate when tropical Pacific upper ocean heat content is anomalously positive (negative). When the $NPMM_{FMAM}$ and WWV_{FMAM} have the opposite sign (e.g., positive WWV_{FMAM} but a negative $NPMM_{FMAM}$), the correlation between WWV_{FMAM} and $CTI_{NDJ(+1)}$ is small and insignificant (r = -0.15; Fig. 3.14a). Moreover, the difference in correlations for cases with anomalously high WWV with and without a positive NPMM is 0.87 (Fig. 3.14b). Hence, WWV alone seems insufficient as a precursor to an ENSO event as there is a strong dependence on NPMM-wind forcing and the TWC mechanism (e.g., *Anderson and Perez* 2015). The NPMM thus contains additional information needed for predicting an ENSO event over WWV alone (e.g., *Anderson* 2007; *Anderson and Perez* 2015).

The SPMM, by contrast, has a negligible relationship with the concurrent WWV (r = 0.07). The SPMM-related wind curl is directed eastward and thus favors Sverdrup transport toward the South American coast (not shown). As such, the SPMM is not associated with the TWC mechanism. Nonetheless, same-signed WWV anomalies appear important for the SPMM to initiate ENSO events (*corr_diff* = 0.44; Figs. 3.14c), while the importance of the SPMM forcing to the connection between WWV and ENSO is relatively weaker (*corr_diff* = 0.23; Fig. 3.14d).

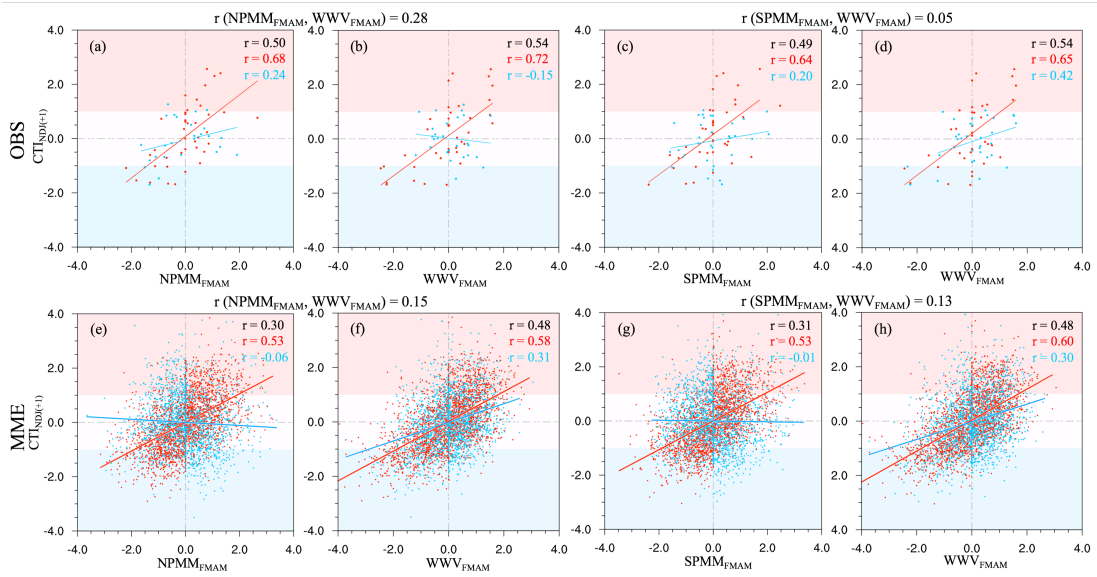

Figure 3.14 (a) Scatterplot between the observed NPMM$_{FMAM}$ and CTI$_{NDJ(+1)}$ indices when the NPMM$_{FMAM}$ is of the same (red dots) and opposite (blue dots) sign with the WWV$_{FMAM}$ anomaly. Threshold values for each case shown with the red and blue background shading. Corresponding colored lines denote the least squares fit line of the respectively-colored dots. Correlation for all points (black) and the conditional correlations for each case (red and blue) included. (b) As (a) but for the WWV$_{FMAM}$ and CTI$_{NDJ(+1)}$ indices. (c)-(d) as (a)-(b) but for the observed SPMM$_{FMAM}$ and CTI$_{NDJ(+1)}$ indices when the SPMM$_{FMAM}$ is of the same (red dots) and opposite (blue dots) sign with the WWV$_{FMAM}$ anomaly. (e)-(h) as (a-d) but for the CMIP5 models.

The CMIP5 models seemingly do not reproduce the TWC mechanism, as the correlations between either PMM and WWV are both low (r = 0.15 for NPMM; r = 0.13 for SPMM; Figs. 3.14e-h). Interestingly, the relationship between the PMMs and

ENSO (*corr_diff* ~ 0.5) is more sensitive to the state of WWV (*corr_diff* ~ 0.5) than the actual sensitivity between WWV and ENSO (*corr_diff* ~ 0.3; Figs. 3.14e-h). The WWV dominates ENSO predictability in the models, as models simulate ENSO variability with a too-short, highly regular period compared to nature (e.g., *Bellenger et al.* 2014). As such, ENSO behaves as more of self-sustained regular oscillatory mode in the CMIP5 MME with WWV modulating that variability.

3.5.3 A Simple Statistical Model for Predicting Boreal Winter Pacific SSTA

Thus far, we have presented evidence of the relationship between both PMMs and ENSO along with the roles of the PMMs versus ocean subsurface memory (i.e., WWV) in driving ENSO variability. To quantify the relative importance of the NPMM, SPMM, and WWV in long-lead ENSO predictions, we construct a multivariate statistical model of the form:

$$\mathrm{SSTA_{NDJ(+1)}[x,t] = a[x] * NPMM_{FMAM}[t] + b[x] * SPMM_{FMAM}[t] + c[x] * WWV_{FMAM}[t]} \quad (3.4)$$

where *x* is the spatial coordinate, *t* is time, and *a*, *b*, and *c* are the regression coefficients determined by least-squares fitting. This model is run using one, two, and all three predictors to examine the sensitivity of our hindcasts to each predictor. Forecast skill (relative to climatology) of the statistical model hindcasts is quantified through the anomaly correlation coefficient (ACC; *Miyakoda et al.* 1972), i.e.,

$$\mathrm{ACC} = \frac{\sum_{t=1}^{T} f_t v_t}{\sqrt{\sum_{t=1}^{T} f_t^2} \sqrt{\sum_{t=1}^{T} v_t^2}} \quad (3.5)$$

where f_t is the forecast value and v_t is the observed (or model's) value at time *t*. The leave-one-out cross-validation scheme is applied to lessen the overfitting problem (*Elsner and Schmertmann* 1994).

Figure 3.15 summarizes the performance of the statistical prediction model. In reanalysis, when using only the $NPMM_{FMAM}$ index as a predictor, high ACC values prevail in the subtropical North Pacific and the central tropical Pacific with lower ACC values in the far eastern tropical Pacific (Fig. 3.15a). Conversely, when using the $SPMM_{FMAM}$ index only, high predictability regions are located over the eastern equatorial and subtropical Pacific (Fig. 3.15b). These areas of maximized ACC concur with our earlier analysis on how tropical Pacific SSTA correlate with each PMM. Using both the $NPMM_{FMAM}$ and $SPMM_{FMAM}$ captures a significant fraction of the tropical and subtropical Pacific $SSTA_{NDJ(+1)}$ variance versus using a single PMM (Fig. 3.15c). As such, combining the two PMMs brings a statistically significant enhancement to the forecast skill in the Pacific basin (Fig. 3.15c). Considering only WWV_{FMAM} restricts forecast skill to a very narrow belt over the equatorial Pacific (Fig. 3.15d). Although WWV_{FMAM} alone would fare poorly as a predictor for extratropical Pacific SSTA, it elevates ACC values in the central-to-eastern tropical Pacific when combined with the two PMMs (Fig. 3.15e). The prediction skill of the empirical model is comparable to the linear inverse modeling and is higher compared to a univariate first-order autoregressive scheme (*Alexander et al.* 2008). Overall, the results from reanalysis indicate that the NPMM and SPMM together are the most significant predictors of the three for ENSO variability.

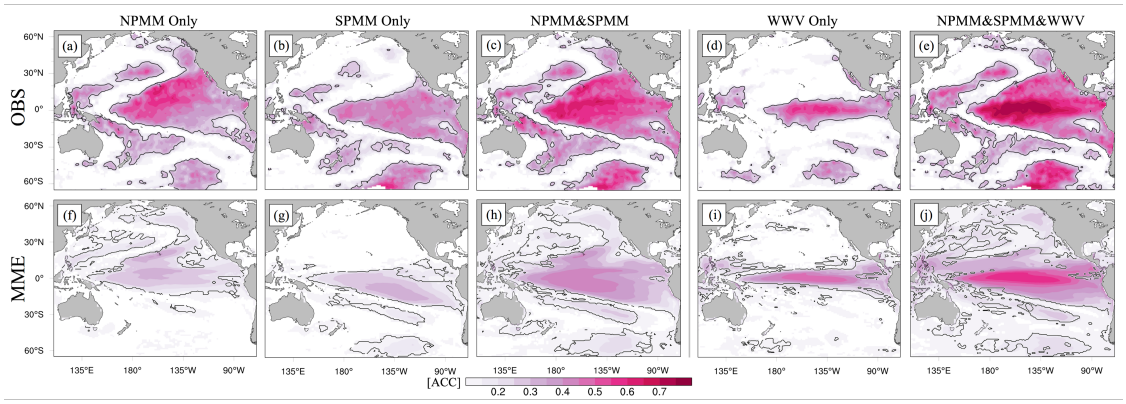

Figure 3.15 (a) Anomaly correlation coefficient (ACC) for the hindcasts of observed $SSTA_{NDJ(+1)}$ using a multivariate linear regression model (see text) when using (a) only the $NPMM_{FMAM}$, (b) only the $SPMM_{FMAM}$, (c) both the $NPMM_{FMAM}$ and $SPMM_{FMAM}$, (d) only WWV_{FMAM}, and (e) $NPMM_{FMAM}$, $SPMM_{FMAM}$, WWV_{FMAM} as predictors. (f)-(j) As in (a)-(e) but for the CMIP5 MME. Black contours outline where ACC values are significant at the 95% confidence level.

Applying the same statistical model to the CMIP5 models, the predictive power of the model is overall lower compared to reanalysis (Figs. 3.15f-j). This lowered ACC calues could in part be because of the larger sample size in the models, but other important differences are also evident. For example, using only the $SPMM_{FMAM}$ index as a predictor, the significant ACC values (ACC ~0.3) reside from the central equatorial Pacific southward to about 10-15°S (Fig. 3.15g). Although the forecast skill increases when using both the $SPMM_{FMAM}$ and $NPMM_{FMAM}$ indices as predictors, the ACC values in the MME are half of that of from observations. (Fig. 3.15h). Instead, the prediction skill for the models comes when using WWV_{FMAM} as a predictor, whose sole contribution is greater than the combination of the two PMMs used together (Fig. 3.15i). This result strongly suggests that the CMIP5 models are overly sensitive to conditions in the tropical Pacific themselves for ENSO predictability rather than capturing the extratropical precursors (i.e., PMMs). Thus, ENSO behaves more like a self-sustained oscillatory mode and there may be actual important coupled ocean-

atmosphere dynamics originating from the extratropics missing from the models, potentially limiting their use for ENSO predictability. Whether the underestimation of the PMM's influences is caused by the model bias in the atmospheric internal variability or the atmosphere-ocean thermodynamic coupling warrants further investigation through numerical experiments.

To provide a rigorous test to the empirical models, we proceed one step further to examine the predictions of several unusual ENSO episodes in the past decade (i.e., 2012/2013, 2014/2015, and 2017/2018), which have been documented in several recent studies (i.e., *Su et al.* 2014; *Min et al.* 2015; *Hu and Fedorov* 2016). Figure 3.16 shows the predictions of SSTA in those years using just the PMMs and the complete model (PMMs and WWV). For comparison, Figure. 3.17 shows the NMME forecasts initialized at almost the same time as the statistical model predictors. The discussion of each event is below.

- 2012/2013 event. During the summer 2012, there was a clear signal of the developing El Niño over the equatorial Pacific corresponding to strong positive SPMM (*Su et al.* 2014; see the SPMM index in Fig. 3.2d). However, the warming juxtaposed with an extremely negative NPMM (Fig. 3.16a) and thus the warm event was not favored based on our prediction scheme. Note that including WWV into the model actually change the sign of the forecasted eastern equatorial SSTA (Figs. 3.16a and 3.16b), suggesting that the NPMM's influence was much more important than pre-existing warm water in the tropical pacific.

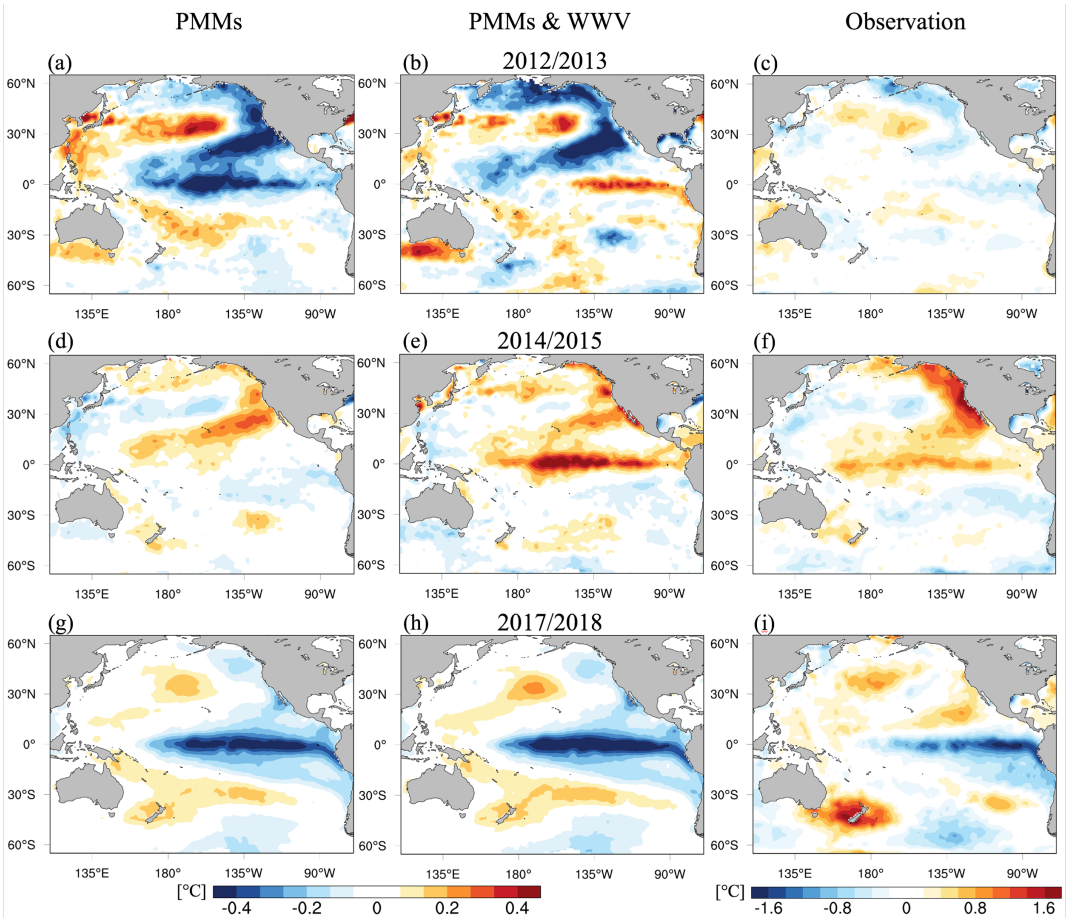

Figure 3.16 Predictions of the NDJ(+1) Pacific SSTA (shading, °C) in (a-c) 2012/2013, (d-f) 2014/2015, and (g-i) 2017/2018 with (a, d, g) PMMs, PMMs and WWV (b, e, h) as predictors. Note the color bars for the prediction and observation are different.

- 2014/2015 event. This event was identified as a CP type. The prediction based on our scheme (Figs. 3.16d-e) is very close to the observed SSTA (Fig. 3.16f). Physically, the extremely negative SPMM (Fig. 3.2d) hampered the development of tropical SSTA excited by the concurrent positive NPMM and WWV. In the equatorial Pacific, the influences of the out-of-phase PMMs canceled each other out (Fig. 3.16d). Thereby the boreal winter warming residing in the narrow equatorial band was primarily driven by the positive WWV. Furthermore, the SSTA in the extratropical Pacific are successfully predicted with the statistical model, especially the South Pacific

SSTA dipole and the North Pacific SSTA elongating from the west coast of North America into the central tropics (Figs. 3.16e-f). By contrast, the dynamical models predicted a super warm event though with large ensemble spread (Figs. 3.17c-d).

- 2017/2018 event. During spring 2017, the SPMM-induced super warming off the Peruvian coast (see Fig. 3.2d for SPMM index) suggested that an El Niño event would develop during the following winter (Figs. 3.17e-f). However, the SPMM switched into neutral and even negative values during late boreal spring and summer. This, combining with a negative NPMM, a La Niña event was instead favored (Figs. 3.16g-i).

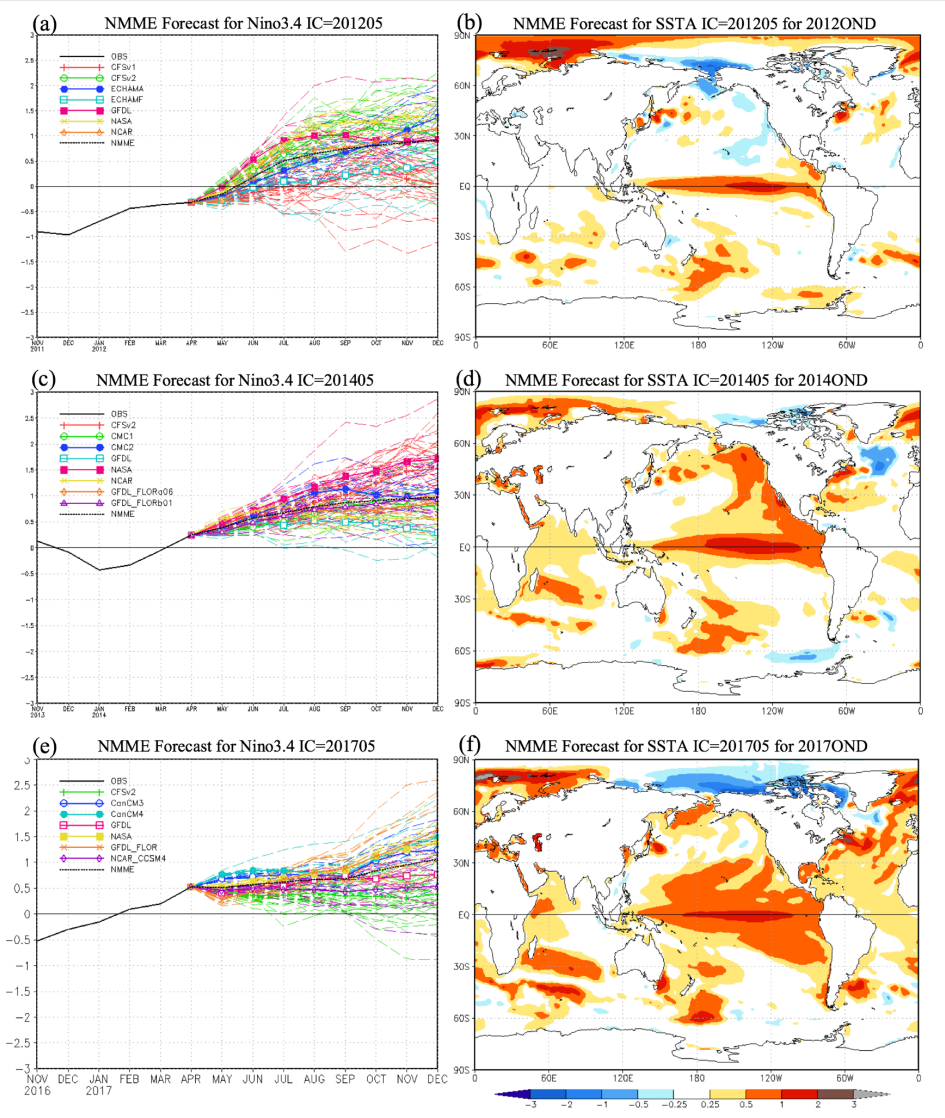

Figure 3.17 (a, c, e) The Niño3.4 index (SSTA averaged over 5°S~5°N and 170°W~120°W) and (b, d, f) the OND SSTA forecasts by NMME models initialized in (a-b) May 2012, (c-d) May 2014, and (e-f) May 2017, respectively. The plots are downloaded from the NMME website (http://www.cpc.ncep.noaa.gov/products/NMME/archive/; NMME Realtime Forecasts Archive).

3.6 Chapter Summary and Discussion

This chapter explored the characteristics of the South Pacific Meridional Mode (SPMM) and its influence on tropical Pacific climate variability, specifically the El Niño-Southern Oscillation (ENSO) phenomenon. The SPMM emerges as a robust

thermodynamically-coupled mode driven by the South Pacific atmospheric internal variability (Figs. 3.2-3.3). The seasonality of the SPMM wind and SST components vary out of phase with the maximum SST variance occurring in austral summer, while the strongest wind variance occurs in austral winter. The response of South Pacific SSTA to the surface wind anomalies during the austral winter is weaker than expected due to a deeper mixed layer (Figs. 3.4-3.5). Nevertheless, the SPMM operates as an effective conduit for South Pacific austral summer atmospheric variability to propagate into the tropics and thereafter contribute to the initiation of ENSO events. The constructive and destructive interference between the NPMM and SPMM through the austral fall shapes and regulates the temporal evolution, intensity of the final event, and also the flavors of the ensuing ENSO events. Incorporating the two PMMs into a simple statistical predictive model substantially enhances ENSO prediction skill with a 6-12 month lead time (Figs. 3.15-3.17), potentially reducing the existing spring predictability barrier currently plaguing ENSO seasonal forecasts.

Aside from the SPMM, two major differences between the North and South Pacific atmospheric variability associated with the PMMs are also noted. First, the amplitude of the mean seasonal cycle in the Southern Hemisphere atmospheric variability is lower (Figs. 3.4, 3.7; e.g., *Kiladis and Mo* 1999; *Cai and Watterson* 2002), which allows the SSTA and wind anomalies associated with the SPMM to vary out of phase (Fig. 3.2c), making the SPMM a candidate to initiate ENSO events (Fig. 8). As recent studies have highlighted the impacts of the austral winter South Pacific variability on 2-year La Niña (*DiNezio et al.* 2017) and on El Niño flavors (*Meehl et al.* 2017), advancing ENSO prediction skill may stem from observing the South Pacific.

Second, akin to the NPO, the internal atmospheric modes exciting the SPMM features a large-scale dipole (*Okumura* 2013; *Zhang et al.* 2014a), which may be termed the South Pacific Oscillation (SPO). As the tropically forced variability projects onto this dipole structure as well (Figs. 3.3, 3.6; e.g., Cai and Watterson 2002), the SPMM-induced tropical Pacific SSTA, in turn, reinforce the SLPA driver pattern, potentially forming a fast positive feedback and explaining why the SLPA pattern associated with the SPMM decays slowly compared to the NPO (Figs. 3.1-3.12).

The close correspondence of the major features of the SPMM and the associated seasonal evolutions of Pacific oceanic and atmospheric variability related to the SPMM in reanalysis products and CMIP5 models bolster our findings and conclusions. Hence, these results provide an additional benchmark for testing and evaluating tropical Pacific climate prediction in other coupled climate models. The CMIP5 MME captures the spatiotemporal characteristics and physical mechanisms of the SPMM reasonably well (Figs. 3.6-3.9), but seemingly underestimate (overestimate) the impacts of the PMMs (WWV) on ENSO variability (Figs. 3.14-3.15).

This study also contributes to an emerging and growing body of literature on the role of the PMMs in linking the extratropical and tropical Pacific variability. The SSTA pattern associated with the PMMs closely resembles the optimal initial condition SSTA pattern that precedes ENSO by 6~7 months (*Penland and Sardeshmukh* 1995; *Alexander et al.* 2008; *Newman et al.* 2011; *Vimont et al.* 2014; *Capotondi et al.* 2015b). While either meridional mode alone can excite ENSO events, we propose the possibility that the interplay between the PMMs regulates the ENSO diversity. Geographically, the SPMM regulates the anomalies in the eastern Pacific cold tongue while the NPMM-

related anomalies extend into the western Pacific warm pool. In contrast to the suppressed thermocline feedback, the zonal advection feedback intensifies in the vicinity of the western Pacific warm pool, contributing to the central Pacific-like SSTA when the NPMM is accompanied by opposite-signed SPMM cases (Fig. 3.12-3.13). In other words, when ocean dynamics are involved, the impacts of the two PMMs on the tropics are comparable.

Finally, the results presented in this chapter do not downplay the contributions of other processes involved with ENSO complexity, e.g., westerly wind bursts (*Chen et al.* 2015). Analogous to the connection between the NPMM and westerly wind bursts (*Nakamura et al.* 2006, 2007; *Alexander et al.* 2010), the linkage between the SPMM and the so-called high-frequency easterly wind surges in the central-eastern tropical Pacific (*Hu and Fedorov* 2016; *Zhu et al.* 2016; *Levine and McPhaden* 2016; *Chiodi and Harrison* 2015, 2017) deserves further investigation. Also note that stochastic processes during the boreal spring have caused prediction failure in many ENSO forecasts from statistical and dynamical models (e.g., *Landsea and Knaff* 2000). Our hypothesis on the significant role of the SPMM on contributing to the evolution of ENSO events may shed light on past unusual (and misforecasted) ENSO episodes, including the failure of the highly-anticipated 2014-2015 El Niño event (Figs. 3.16-3.17; e.g., *Su et al.* 2014; *Min et al.* 2015; *Hu and Fedorov* 2016; *Imada et al.* 2016).

Chapter 4: Austral winter South Pacific atmospheric internal variability and its role in the development of ENSO events[3]

4.1 Background and Motivation

As discussed in Chapter 3, the WES feedback involved with the SPMM maximizes during the austral summer and fall (i.e., February-May), indicating that South Pacific atmospheric variability creates favorable conditions for the ENSO occurrence. Although combining the two PMMs and WWV enhances ENSO prediction, where the maximum equatorial Pacific SSTA resides remains uncertain.

On the other hand, the boreal winter NPMM appears to be a precursor for both EP and CP events (Figure 4.1; see also *Penland and Sardeshmukh* 1995; *Ding et al.* 2015a). As the South Pacific variability is most energetic during austral winter, whether it inserts any significant impact and provides additional information for the prediction of ENSO flavor are left as an open question. *Jin and Kirtman* (2009) suggest that the South Pacific SLPA, which leads ENSO maturity by one to two seasons, is actually a response to the developing ENSO event due to the local seasonality.

In this chapter, we employ both reanalysis and the North American Multimodel Ensemble (NMME) Phase-II models designed for subseasonal-to-seasonal predictions. Compared to AGCM simulations with prescribed SSTA, the full ocean-atmosphere coupling in NMME allows us to examine the two-way interactions between the tropical Pacific SSTA and South Pacific circulation anomalies. Based on the results shown

[3] Results presented in this chapter are part of two peer-reviewed journal manuscripts.
You, Y., and J. C. Furtado, 2017: The role of South Pacific atmospheric variability in the development of different types of ENSO. *Geophys. Res. Lett.*, 44, 7438–7446, doi: 10.1002/2017GL073475
You, Y., and J. C. Furtado, 2018b: Relationship between South Pacific atmospheric internal variability and ENSO in the North American Multimodel Ensemble Phase-II Models. *Geophys. Res. Lett.*, in prep.

below, we argue that the response of the austral winter South Pacific extratropical circulation to tropical Pacific forcing is strongly modulated by the atmospheric intrinsic variability, which thereafter contributes the development of ENSO events. Results also indicate that the austral winter South Pacific atmospheric variability offers potential implications for the prediction of ENSO flavor, which is currently limited to less than one-season lead time in dynamical models (e.g., *Hendon et al.* 2009).

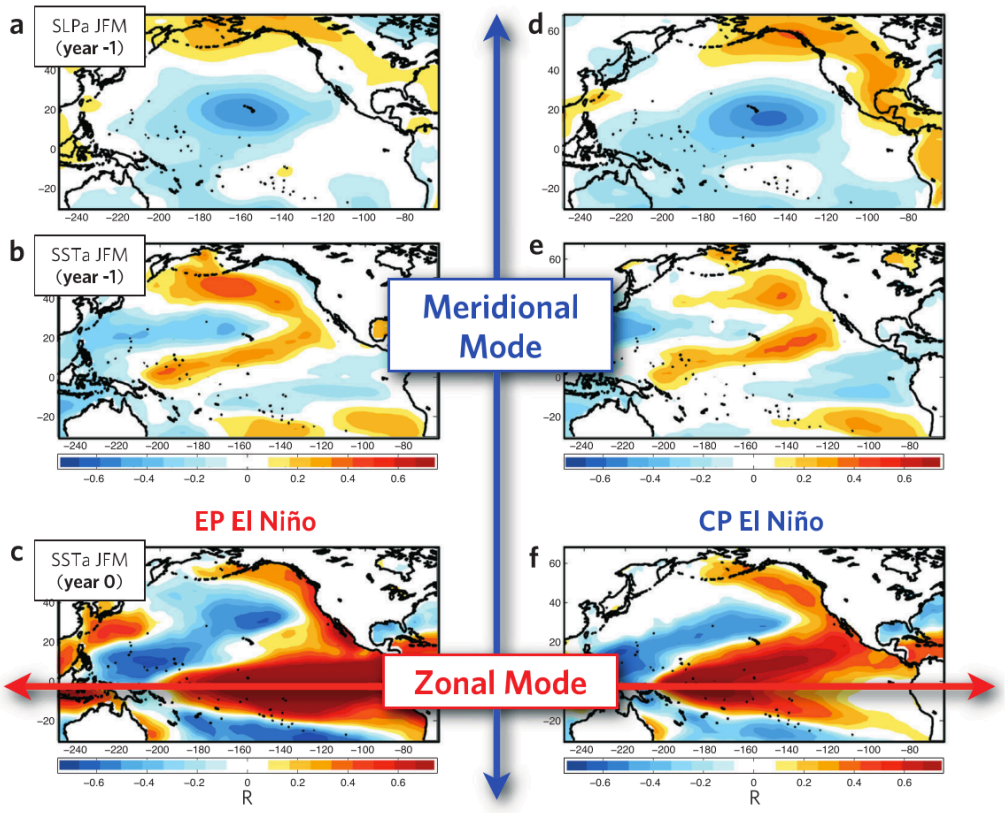

Figure 4.1 Correlation map between winter (January-March) EP ENSO index and (a) SLPA in the prior winter, (b) SSTA in the prior winter, and (c) with concurrent SSTA associated with the EP ENSO. (e)-(g) The same analysis done with the CP ENSO index. Adapted from *Di Lorenzo et al.* (2015).

This chapter is organized as follows. Section 4.2 documents the reanalysis datasets, model outputs, and the statistical methods employed. Section 4.3 presents the dominant mode of the austral wintertime South Pacific atmospheric variability, and its

influences on the development of the ensuing ENSO events. Discussion and conclusions of this chapter follow.

4.2 Data and Methods

To better understand ENSO diversity, we use multiple indices based on the SSTA averaged over given regions as shown in Figure 4.2. The Niño3 (Niño4) index, calculated by averaging SSTA from 5°S-5°N and 150°W-90°W (5°S-5°N and 160°E-150°W), characterizes the eastern (central) equatorial Pacific SSTA state. In defining events, a(n) El Niño (La Niña) year is defined as a year in which the December-February (DJF) Niño3 or Niño4 index exceeds (falls below) 0.5°C (-0.5°C). Following *Yeh et al.* (2009), an El Niño event is classified as a(n) CP (EP) type if the Niño4 index is greater (less) than the Niño3 index.

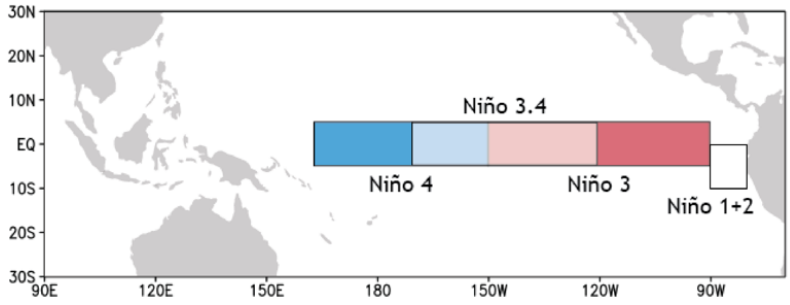

Figure 4.2 Locations of Niño regions for measuring SSTs in the tropical Pacific Ocean. Adapted from https://climatedataguide.ucar.edu/climate-data/nino-sst-indices-nino-12-3-34-4-oni-and-tni.

In investigating oceanic pathways linking the South Pacific to the tropical Pacific, we compute the depth-integrated meridional velocity V (i.e., Sverdrup transport; e.g., *Anderson and Perez* 2015):

$$\mathrm{V} = \frac{1}{\beta\rho}\left[\frac{\partial \tau_{\mathrm{y}}}{\partial \mathrm{x}} - \frac{\partial \tau_{\mathrm{x}}}{\partial \mathrm{y}}\right] \tag{4.1}$$

where τ_x and τ_y are the eastward and northward components of the wind stress, respectively, β is the latitudinal gradient of Coriolis parameter, and ρ = 1025kg/m^3 is the density of sea water. The wind stresses are computed as $\tau = C_D \rho_{air} U^2$, where C_D = 0.0013 is the drag coefficient, ρ_{air} = 1.2kg/m^3 is the density of air, and U is the 10-m wind speed.

For some analyses, we are interested in removing the linear dependence of a time series $y(t)$ with some other climate mode or variable $x(t)$ to examine residual variability. Calling this residual $y_{\text{-}rx}$: $y_{\text{-}rx}(t) = y(t) - [\alpha + \beta * x(t)]$, where α and β are found through least-squares fitting. Thus, $y_{\text{-}rx}(t)$, is, by definition, uncorrelated with $x(t)$.

A complete description of NMME Phase-II models was presented in Chapter 2. In order to isolate the austral winter internal variability, we utilize the models initialized on June 1st. We note that the forecast models experience drift toward their own climatology at long forecast lead times. As such, we bias-correct the NMME monthly-mean output by removing the forecast (which is lead-time dependent) 29-year climatology of each model separately. The ensemble-mean statistics are computed first by averaging the fields in the 10 ensemble members to suppress the atmospheric internal variability. The ensemble spread is then represented as the deviation of that member's field from the ensemble mean (i.e., $x' = x - \bar{x}$). Then the various patterns related to a given ensemble spread index are computed by regression analysis.

In the NMME models, major warm and cold events during austral winter are defined when the JJA Niño3 (Niño3$_{\text{JJA}}$) exceeds (falls below minus) 0.8σ. This procedure yields 6 warm$_{\text{JJA}}$ and 7 cold$_{\text{JJA}}$ events. Likewise, 7 El Niño (1982, 1986, 1987, 1991, 1997, 2002, 2009) and 6 La Niña (1984, 1988, 1999, 2005, 2007, 2010)

events are identified when the NDJ Niño3 ($Niño3_{NDJ}$) exceeds (falls below minus) 0.8σ. In reanalysis, 13 $warm_{JJA}$ and 15 $cold_{JJA}$ events are identified accordingly. Note the conclusions hold when using a threshold of 0.5σ. The selected events are listed in Table 4.1.

Table 4.1 The selected $warm_{JJA}$ and $cold_{JJA}$ events based on the criteria in the text.

Year	Observation
$warm_{JJA}$ (13)	1951, 1957, 1963, 1965, 1969, 1972, 1976, 1982, 1983, 1987, 1997, 2009, 2015
$cold_{JJA}$ (15)	1954, 1955, 1964, 1970, 1973, 1975, 1978, 1984, 1985, 1988, 1999, 2000, 2007, 2010, 2013
Year	NMME
$warm_{JJA}$ (6)	1982, 1983, 1987, 1991, 1997, 2009
$cold_{JJA}$ (7)	1984, 1985, 1988, 1999, 2000, 2007, 2010

4.3 Results

4.3.1 Reanalysis

We begin by examining the dominant mode of the South Pacific atmospheric variability via EOF analysis of monthly-mean South Pacific SLPA field over the domain 10°S-45°S and 160°W-70°W. Figure 4.3a shows the regressions of monthly-mean SLPA (line contours), SSTA (shading), and 10-m wind anomalies (vectors) onto the standardized leading principal component (PC1) time series of monthly-mean South Pacific SLPA. The leading mode explains about 46% of the total variance in South Pacific SLPA, is significantly separated from higher order modes according to the *North et al.* (1982) criteria, and is robust to reasonable variations in the domain size (not shown). Similar to the SLPA signature associated with the SPMM (Figure 3.2), the positive phase, as defined in Fig. 4.3a, features a meridional SLPA dipole between the

subtropics (cyclonic anomalies) and mid-to-high latitudes (anticyclonic anomalies) with an equivalent barotropic structure throughout the troposphere (not shown). We call this SLPA pattern the South Pacific Oscillation (SPO), owing to its analogous structure to the NPO, and its associated time series (i.e., PC1) the SPO index. The cyclonic SLPA loading center generally overlaps the location of the South Pacific High and thus weaken the climatological southeasterly trade winds (Fig. 4.3a, vectors). The positive phase of the SPO covaries strongly with warm SSTA throughout the central and eastern tropical Pacific (Fig. 4.3a, shading). Indeed, the SPO is significantly correlated with the CTI (r = 0.56; p < 0.01) with the maximum correlation occurring when the SPO leads the CTI by 3-4 months (Fig. 4.3b). The SPO variability spans a wide range of time scales (intraseasonal, interannual and even decadal; Fig. 4.3c) with seasonal variability maximized during austral winter (i.e., JJA; Fig. 4.3d).

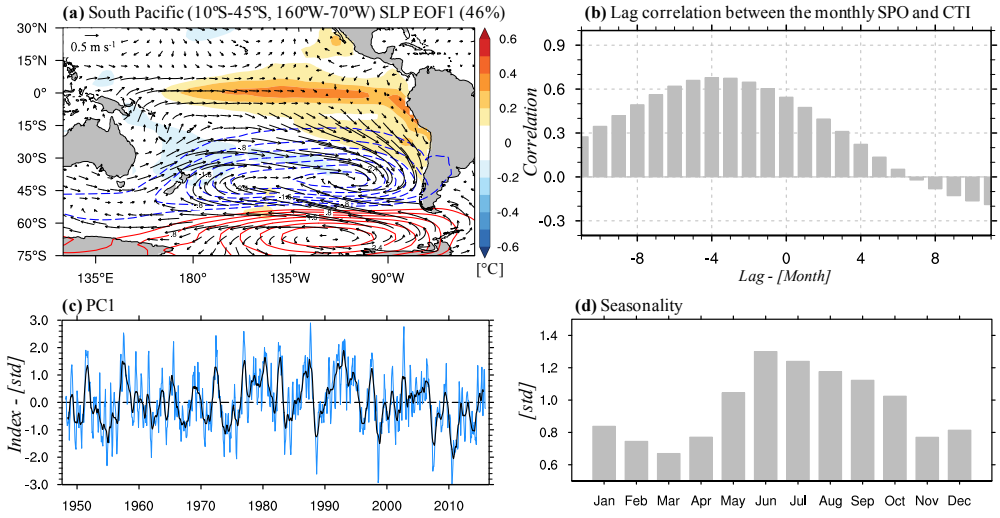

Figure 4.3 (a) Regression of SLPA (contour, hPa), SSTA (shading, °C), and 10-m wind anomalies (vector, m/s) onto the standardized PC1 time series of monthly-mean South Pacific SLPA (i.e., the SPO index). Contour interval 0.4 hPa (line contours) and 0.1°C (shading). Reference wind vector 0.5 m/s. Solid (dashed) line contours indicate positive (negative) values. Zero contour omitted. (b) The lag correlation between the SPO index and the CTI. Negative (positive) lags indicate the SPO index leads (lags) the CTI. (c) The standardized SPO index (blue) and its 9-month running-mean (black). (d) Seasonality of the SPO index expressed by the standard deviation as a function of calendar month.

To elucidate the connections between the SPO and the tropical Pacific, we focus on the austral winter (JJA) when the SPO is most variable. Figure 4.4 shows the lagged-regression maps of SLPA, SSTA, and 10-m wind anomalies onto the standardized JJA SPO (SPO_{JJA}) index from MAM through DJF+1 (i.e., the peak season for ENSO). During MAM, (Fig. 4.4a), the characteristic SSTA and wind anomaly patterns associated with the NPO/NPMM are apparent (*Chiang and Vimont* 2004). By JJA, a canonical (i.e., EP) El Niño is established with the maximum SSTA over the central-eastern tropical Pacific (Fig. 4.4b; shading) concomitant with a positive SPO (Fig. 4.4; line contours). From JJA to SON, the anomalous wind stresses associated with the SPO promote anomalous equatorial divergence of water west of 150°W in both hemispheres, as shown by the regression of V onto the SPO_{JJA} index (Figs. 4.4f-g). By contrast, anomalous equatorward mass transport is centered south of the equator between 150°W-90°W (Figs. 4.4f-g), co-located with warmest SSTA (Figs. 4.4b-c), thereby charging the eastern equatorial Pacific, in accordance with the TWC mechanism (*Anderson et al.* 2013; *Anderson and Perez* 2015). Hence, positive ocean heat content builds in the central tropical Pacific and eventually discharges to the east from JJA to DJF (Figs. 4.4f-g), resulting in a warm EP ENSO event (Fig. 4.4d).

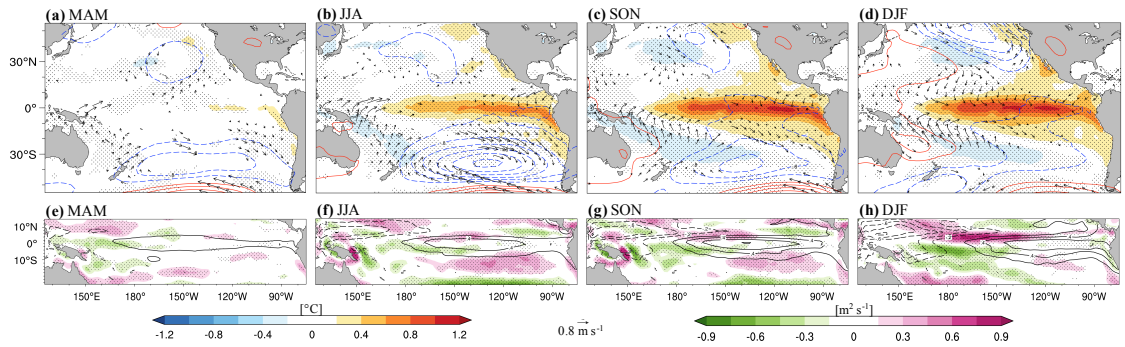

Figure 4.4 (a)-(d) Lag regression of SLPA (contours, hPa), SSTA (shading, °C), and 10-m wind anomalies (vector, m/s) onto the standardized SPO_{JJA} index for (a) March-May (MAM), (b) June-August (JJA), (c) September-November (SON), and (d) December-February (DJF). For (a), the fields lead the SPO_{JJA} index, while for (c) and (d), the SPO_{JJA} index leads the fields. Contour interval 0.2°C for SSTA and 0.4 hPa for SLPA. Reference wind vector 0.8 m/s. Wind vectors plotted only where significant at the $p<0.05$ level. (e)-(h) As (a)-(d) except for the anomalous vertically-integrated meridional oceanic mass transport (V; shading, m^2/s) and ocean heat content (vertically-averaged temperature integrated from 0 to 300m; contour, °C). Contour internal 0.15 m^2/s for V, and 0.2 °C for ocean heat content. Solid (dashed) line contours indicate positive (negative) values. Zero contour omitted. Stippling indicates statistically significant SSTA regression coefficients at the $p < 0.05$ level according to a two-tailed Student's t test.

Is the SPO merely a response to tropical Pacific forcing, or does it contain significant internal variability that can impact tropical Pacific SSTA? To answer this question, Figure 4.5a shows the regression of JJA SLPA (contours), SSTA (shading), and 10-m wind anomalies (vectors) onto the CTI_{JJA} index. The SLPA field clearly displays a SPO-like structure in the South Pacific, indicating that at least a portion of its variability covaries with tropical Pacific SSTA. Next, to examine the potential stochastic component of the SPO, we conduct EOF analysis on the residual South Pacific SLPA field - i.e., the SLPA field after linearly removing the CTI_{JJA} index: $SLPA_{res}$= SLPA-(α+β*CTI_{JJA}). Therefore, $SLPA_{res}$ has uncorrelated with tropical Pacific SSTA in the CTI region. The leading mode of $SLPA_{res}$ (i.e., the spatial pattern $EOF1_{res}$ and its associated time series $PC1_{res}$) accounts for 48% of the variance in $SLPA_{res}$ and resembles strongly the SPO (Fig. 4.5b, line contours; r (SPO_{JJA}, $PC1_{res}$) =

0.79; $p < 0.01$). Therefore, we suggest that the SPO cannot be viewed only as a response to forcing form tropical Pacific SSTA but instead contains significant (and independent) internal variability that can subsequently play a role in the development of an ENSO event.

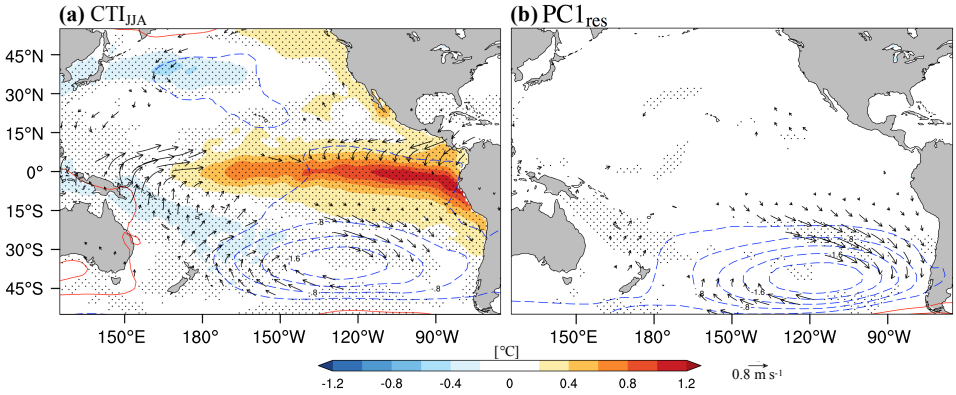

Figure 4.5 (a) Regression of JJA SLPA (contour, hPa), SSTA (shading, °C), and 10-m wind anomalies (vector, m/s) onto the standardized CTI_{JJA} index. (b) As in (a), except for regression onto the standardized $PC1_{res}$ index (see text for details). Contour interval 0.2°C for SSTA and 0.4 hPa for SLPA. Reference wind vector 0.8 m/s. Solid (dashed) line contours indicate positive (negative) values. Zero contour omitted. Wind vectors plotted only where significant at the $p < 0.05$ level. Stippling as in Fig. 4.4.

We now examine how important the SPO_{JJA} variability is relative to the austral fall (boreal spring) NPO (NPO_{MAM}) in the development of an ENSO event. The NPO index is traditionally defined as the second leading EOF of SLPA poleward of 15°N in the North Pacific (*Linkin and Nigam* 2008). However, it is the Hawaiian node that is most important for seasonal (and longer) linkages to the tropical Pacific (e.g., *Vimont et al.* 2003a; *Anderson et al.* 2003, 2007; *Di Lorenzo et al.* 2010; *Furtado et al.* 2011, 2012). Therefore, for this study, we define the NPO index as the SLPA averaged over 13°N-24°N and 158°W-135°W (i.e., SLPA associated with the node near Hawaii). Figure 4.6 shows the lag regression of SLPA (line contours), SSTA (shading), and 10-m wind anomalies (vectors) onto three different indices:

- The NPO_{MAM} index (Figs. 4.6a-d)
- The $NPO_{MAM\text{-}rNiño3}$ index, found by linearly removing the $Niño3_{JJA}$ index from NPO_{MAM} index: $NPO_{MAM\text{-}rNiño3} = NPO_{MAM} - [\alpha_1 + \beta_1 * Niño3_{JJA}]$ (Figs. 4.6e-h)
- The $NPO_{MAM\text{-}rSPO}$ index, found by linearly removing the SPO_{JJA} index from the NPO_{MAM} index: $NPO_{MAM\text{-}rSPO} = NPO_{MAM} - [\alpha_2 + \beta_2 * SPO_{JJA}]$ (Figs. 4.6i-l)

The lag regressions on the NPO_{MAM} index (Figs. 4.6a-d) illustrate the ENSO lifecycle as expected from the seasonal forecasting mechanism framework (*Vimont et al.* 2003; *Chiang and Vimont* 2004; *Chang et al.* 2007): (1) the SSTA and wind anomalies extend from the subtropical North Pacific into the central-western tropical Pacific during MAM (Fig. 4.6a); (2) the SSTA subsequently expand into the eastern tropical Pacific and (3) finally grow into an ENSO event during DJF (Figs. 4.6b-d). When examining lag regressions of the same fields onto the $NPO_{MAM\text{-}rNiño3}$ index (Figs. 4.5e-4.5h), we see that, by construction, the tropical Pacific SSTA do not expand into the Niño3 region during JJA (Fig. 4.6f). Nonetheless, significant positive SSTA encompass the eastern tropical Pacific during the following DJF (Figs. 4.6g-h). This finding suggests that JJA Niño3 region positive SSTA are not necessary to result in an EP-type ENSO event (Fig. 4.6d). By contrast, upon removing SPO_{JJA} variability linearly from the NPO_{MAM} index (Figs. 4.6i-l), the positive SSTA are now confined to the central equatorial Pacific throughout the period and develop *in situ* into a CP ENSO event, resembling the evolution of a CP ENSO event shown by *Kug et al.* (2009) and *Kao and Yu* (2009). Similar conclusions are found when examining ocean heat content anomalies (not shown). Note that while these lag regression analyses cannot prove

definitively the exact influence of the SPO on ENSO, they provide clues as to its contribution relative to the current paradigm involving the NPO.

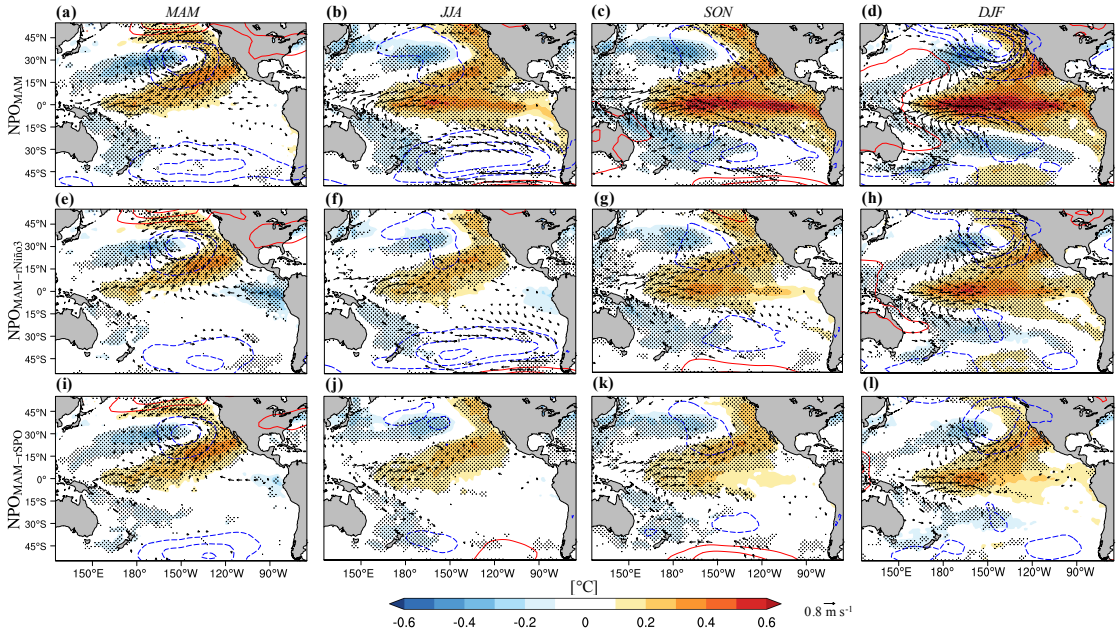

Figure 4.6 (a)-(d) As in Figs. 4.3(a)-(d) except for regressions onto the standardized NPO_{MAM} index. (e)-(h) As in (a)-(d) except for regressions onto the standardized $NPO_{MAM\text{-}rNiño3}$ (see text for details). (i)-(l) As in (a)-(d) except for regressions onto the standardized $NPO_{MAM\text{-}rSPO}$ (see text for details). Contour interval 0.1°C (shaded contours) and 0.4 hPa (line contours). Reference wind vector 0.8 m/s. Solid (dashed) line contours indicate positive (negative) values. Zero contour omitted. Stippling as in Fig. 4.4.

4.3.2 NMME Hindcasts

The above analyses suggest that SPO_{JJA} cannot be viewed only as a response to forcing form tropical Pacific SSTA but instead contains significant internal variability (Fig. 4.5). Henceforth, we utilize the NMME hindcasts initialized on June 1st to isolate the role of the atmospheric internal variability in the scenario of similar JJA SSTA forcing. Although the period covered is relatively short (i.e., 1982-2010), the 10 ensemble members increase the sample size.

To set the stage, first we check if the models reasonably reproduce the relationship between the South Pacific SLPA and tropical Pacific SSTA during JJA. Figure 4.7a displays box-whisker diagrams of the correlation coefficients between $\text{Niño3}_{\text{JJA}}$ and the northern node of the JJA SPO (i.e., $\text{SPO}_{\text{JJA}}^{\text{NP}}$; SLPA averaged over 15°S-40°S and 180-90°W). We focus on the $\text{SPO}_{\text{JJA}}^{\text{NP}}$ as it regulates the South Pacific subtropical high and is most important for linkages to the following ENSO events. The correlations are shown for each model, their ensemble members, and the ensemble-mean. Consistent with previous analyses, the overall correlation is negative (i.e., a positive $\text{Niño3}_{\text{JJA}}$ anomaly favors a weaker South Pacific subtropical high). Meanwhile, the large amount of spread among ensemble members and the surpassing correlation of the ensemble-mean in both models (Fig. 4.7a, diamonds; $r \sim -0.7$ for CESM1 and $r \sim -0.8$ for CanCM4) support the presence of the internal variability. The member spread in correlation includes the correlation from reanalysis ($r \sim -0.55$; Fig. 4.7a, black cross markers). However, the observed value falls between the highest value and upper quartile in CanCM4 and between the median value and lower quartile in CESM1, suggesting the relationship between the $\text{Niño3}_{\text{JJA}}$ and $\text{SPO}_{\text{JJA}}^{\text{NP}}$ is overestimated (underestimated) in the CanCM4 (CESM1) model.

To further qualify the level of South Pacific variability that is intrinsic versus a response to tropical Pacific SSTA, composites of JJA SLPA and SSTA during the warm_{JJA} and cold_{JJA} events are evaluated. For the NMME models, this contrast can be accomplished simply by comparing the 10 ensemble members. For reanalysis, however, we have only one realization. As such, we employ a random sampling method, or the "bootstrapped composites", following *Deser et al.* (2017). The method goes as follows:

Synthetic composites are formed by randomly sampling with replacement from among the 13 $warm_{JJA}$ and 15 $cold_{JJA}$ events, retaining the same sample size for either category. This sampling is then repeated for 2,000 times. The resulting composites thus yield an estimate of the degree to which sampling variability influences the single "real-world" composite. The observed bootstrapped composites are then ranked by the SPO_{JJA}^{NP}.

Figs. 4.7b and 4.7c display the observed bootstrapped composites of the 10th and 90th percentiles, respectively. The specific events used for the composites are listed in Table 4.2. Although the intensity and spatial structure of the tropical Pacific SSTA are similar in the two composites, the spatial pattern and magnitude of the SPO_{JJA} vary considerably. Although both composites exhibit somewhat similar structure to the SPO_{JJA}, the southern node of the SPO is less coherent in the two composites due to the stronger stochastic variability present at higher latitudes. As to the NMME models, Figs. 4.7d-e (4.7f-g) exhibit the composites of JJA SSTA (shading) and SLPA (contours) based on the same set of the $warm_{JJA}$ (6) and $cold_{JJA}$ (7) events for the CESM1 (CanCM4). Only the ensemble member that simulates the weakest and strongest SPO_{JJA}^{NP} are shown. As seen, the SLPA dipole is reasonably reproduced while remarkable diversity similar to the observed bootstrapped composites is also apparent. Although the composites yield below-normal SLPA in the extratropical South Pacific, the amplitude of the SLPA varies greatly, indicating the SPO_{JJA}^{NP} is substantially influenced by the intrinsic variability. In line with Fig. 4.7a, the overall response of South Pacific circulation to the tropical SSTA is stronger in CanCM4 model than CESM1 model.

Table 4.2 The $warm_{JJA}$ and $cold_{JJA}$ events for the observed bootstrapped composites.

Year	Bootstrapped $warm_{JJA}$ and $cold_{JJA}$ composites – 10%
$warm_{JJA}$ (13)	1957(2), 1963(2), 1965(2), 1969, 1972, 1976, 1982, 1987, 2009, 2015
$cold_{JJA}$ (15)	1954(2), 1955(2), 1970(2), 1973(2), 1978, 1988, 2000, 2007, 2010(2)
Year	Bootstrapped $warm_{JJA}$ and $cold_{JJA}$ composites – 90%
$warm_{JJA}$ (13)	1951, 1957, 1963(3), 1969, 1972, 1982(2), 1997(2), 2009, 2015
$cold_{JJA}$ (15)	1954(2), 1955, 1964, 1970(2), 1975(2), 1978, 1985(2), 1999(2), 2000(2)

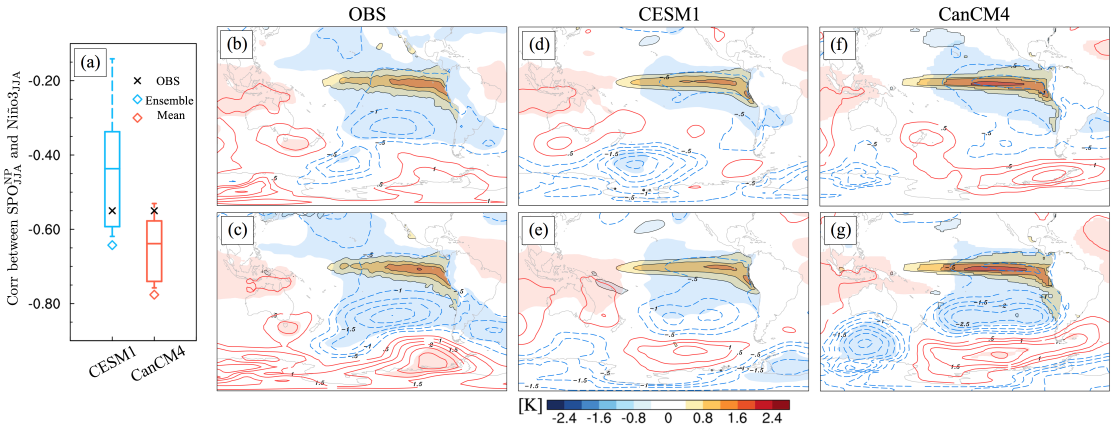

Figure 4.7 (a) Box plots for correlations between the SPO^{NP}_{JJA} and $Niño3_{JJA}$ for the CESM1 (blue) and (red) CanCM4 ensemble members. Bootstrapped $warm_{JJA}$ and $cold_{JJA}$ composites of JJA SLPA (contour, hPa) and SSTA (color shading, °C) for (b) 10th percentile and (c) 90th percentile based on the SPO^{NP}_{JJA} index in reanalysis (see text). The $warm_{JJA}$ and $cold_{JJA}$ composites of JJA SLPA (contour, hPa) and SSTA (color shading, °C) for the CESM1 ensemble members simulating the (d) weakest and (e) strongest SPO^{NP}_{JJA}, respectively. (f, g) As in (d, e) but for the CanCM4. Positive (Negative) SLPA values represented by solid (dashed) contours. Zero contour omitted. Contour interval 0.5hPa. Light blue and light red shading denote where negative and positive SLPA are significant at 95% confidence level, respectively, based on a two-tailed Student's *t* test.

To isolate the JJA atmospheric internal variability in the models, we subtract the ensemble average SLPA (i.e., the "forced" response, as the tropical SSTA boundary condition is similar in each member) from each ensemble member's SLPA field (i.e., $SPO'^{NP}_{JJA} = SPO^{NP}_{JJA} - \overline{SPO^{NP}_{JJA}}$, in which the overbar denotes the ensemble average). To facilitate more commonality amongst the models for this particular analysis, we only consider JJA periods preceding major ENSO events in the following analysis. The

caveat to this approach is that the tropical SSTA are not fixed during JJA so that other high-frequency processes, such as the westerly wind bursts, might be involved, which may cause more uncertainty in the relationship between the SPO'^{JJA}_{NP} and ENSO.

The caveat is addressed by evaluating the relationship between the SPO'^{NP}_{JJA} and $Niño3'_{JJA}$ (i.e., the ensemble spread in $Niño3_{JJA}$; $Niño3'_{JJA} = Niño3_{JJA}-\overline{Niño3_{JJA}}$). The impact of the tropical SSTA forcing is evident in the autocorrelation characteristics of the SPO^{NP} time series shown in Figures 4.8a and 4.8b. The decorrelation timescale for the SPO^{NP}_{June} is longer than 1 month and the autocorrelation exhibits a period in accordance with the ENSO life cycle (red lines). After removing the ensemble average, the e-folding timescale of the SPO'^{NP}_{June} drops to less than one month (black lines), consistent with the white-noise process. Figs. 4.8c and 4.8d relate the $Niño3'_{JJA}$ to SPO'^{NP}_{JJA}. The variance of the SPO'^{NP}_{JJA} is comparable in the two models, ranging from -2~2 hPa and following a Gaussian distribution. The SPO'^{NP}_{JJA} is inversely proportional to the $Niño3'_{JJA}$. To clarify the causality link, the spatial structure of the SPO'^{NP}_{JJA} is examined by regressing the spread of the JJA oceanic and atmospheric variables against the non-standardized SPO'^{NP}_{JJA} time series (Figs. 4.8e-h). The suppressed South Pacific subtropical high weakens the climatological trade winds, reducing upwelling in the eastern tropical Pacific and inducing warm SSTA in the subtropical southeastern and eastern equatorial Pacific (Figs. 4.8e-f).

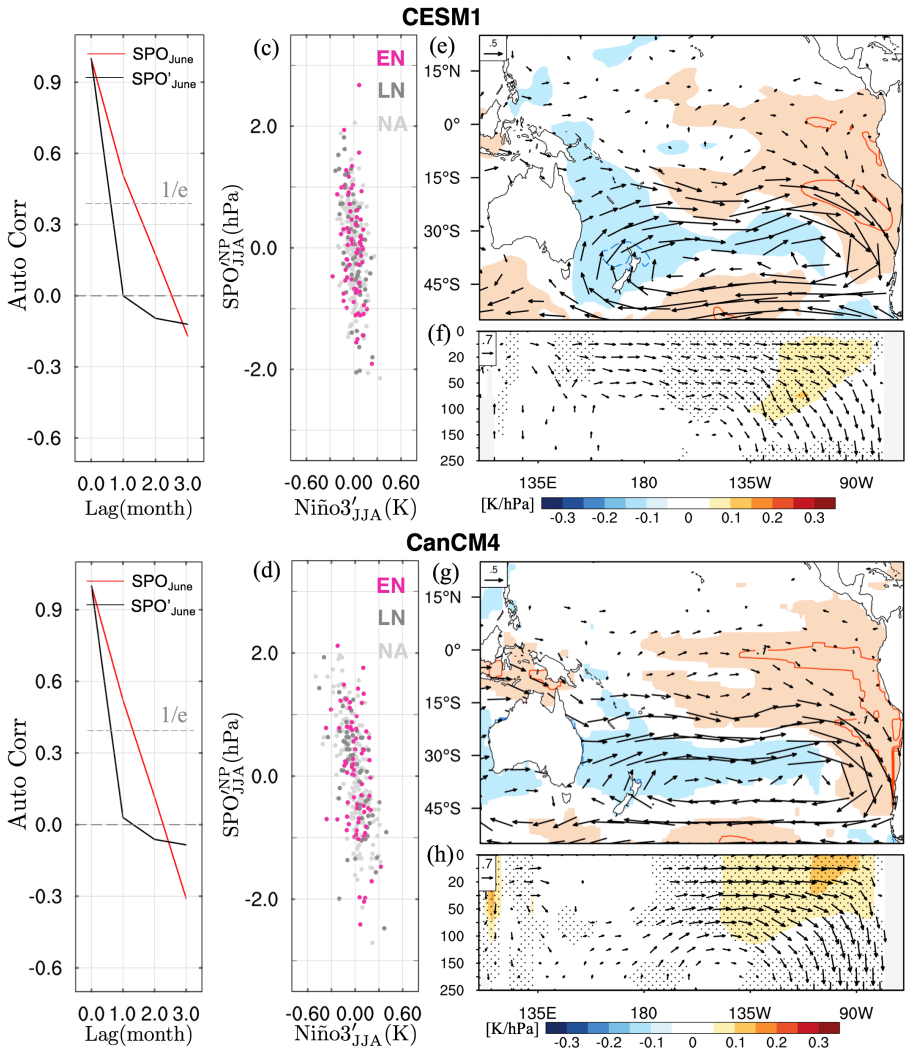

Figure 4.8 (a) Autocorrelation for SPO^{NP}_{June} (red line) and SPO'^{NP}_{June} (black line). (b) Scatter plot of the $Niño3'_{JJA}$ versus SPO'^{NP}_{JJA}. Regressions of JJA (e) SSTA′ (shading, °C/hPa) and U_{850}' (vector, m/s hPa), (g) equatorial (5°N-5°S) T_{sub}' (shading, °C/hPa) and subsurface velocity (u', w'; vector, cm/s hPa) onto the non-standardized SPO'^{NP}_{JJA} in CESM1. The w' is scaled by $3*10^4$ for visual clarity. The purple, dark gray, and light gray dots in (c, d) represent the events preceding the major El Niño, La Niña, neutral events, respectively. (b, d, g, h) are the same as (a, c, e, f) but for CanCM4. The shading in (e, g) and stippling in (f, h) indicate the SSTA′ and T_{sub}' significant at 95% confidence level, respectively. Positive (Negative) values represented by solid (dashed) contours. Zero contour omitted. Only the significant wind vectors are drawn.

The mechanisms responsible for the SSTA over the eastern equatorial and southeastern Pacific are likely different. In the southeastern Pacific, the SSTA evolution likely results from a combination of anomalously downward latent heat flux, suppressed

upwelling, and the increased shortwave radiation feedback from low stratiform clouds (e.g., *Zhang et al.* 2014a). While in the eastern equatorial Pacific, since the thermocline is climatologically shallow and the vertical temperature gradient is strong in the upper 50 meters over this region, the thermocline feedback via the suppressed upwelling and the deepened thermocline is most likely responsible for the surface warming. Figs. 4.8f and 4.8h support this assertion as the subsurface warming is co-located with the suppressed upwelling near the thermocline ($w'\partial\bar{T}/\partial z$). The zonal advection feedback induced by the anomalous eastward ocean currents ($u'\partial\bar{T}/\partial x$) could also contribute.

To bring out the role of the internal variability on ENSO, the evolution of the anomalous field is visualized by regressing the member spread of atmospheric and oceanic fields in the following seasons against the $\mathrm{SPO}'^{\mathrm{NP}}_{\mathrm{JJA}}$ index (Figure 4.9). In addition to the concurrent changes in the state of the tropical and southeastern Pacific Ocean, the SSTA associated with the $\mathrm{SPO}'^{\mathrm{NP}}_{\mathrm{JJA}}$ grow into an ENSO-like structure in the following boreal winter. In CESM1, although the subtropical wind stress anomalies associated with the $\mathrm{SPO}'^{\mathrm{NP}}_{\mathrm{JJA}}$ signature diminish rapidly after JJA, the Bjerknes feedback amplifies the initial eastern equatorial Pacific SSTA and T_{sub}, promoting warming along the equator and giving rise to an ENSO-like pattern in the boreal winter (Figs. 4.9c-d). Driven by the wind-evaporation-SST (WES) feedback (*Xie and Philander* 1994), the SSTA and wind anomalies in the southeastern Pacific could also propagate northwestward into the central equatorial Pacific. This lagged evolution of the atmospheric and oceanic fields associated the $\mathrm{SPO}'^{\mathrm{NP}}_{\mathrm{JJA}}$ is largely linear as the composites yield similar results to the linear regressions (not shown). As such, the $\mathrm{SPO}'^{\mathrm{NP}}_{\mathrm{JJA}}$ modulates the ensemble spread of the ENSO prediction (i.e., $\mathrm{Niño3}'_{\mathrm{NDJ(+1)}}$ =

$\text{Niño3}_{\text{NDJ(+1)}}$-$\overline{\text{Niño3}_{\text{NDJ(+1)}}}$) as suggested by the negative correlation between the $\text{SPO}'^{\text{NP}}_{\text{JJA}}$ and $\text{Niño3}'_{\text{NDJ(+1)}}$ (r = -0.57 for CESM1; Fig. 4.9a). That said, the member with a more negative (positive $\text{SPO}'^{\text{NP}}_{\text{JJA}}$) tends to predict a stronger (weaker) El Niño (La Niña) event. A similar relationship is found in the CanCM4 model (r = -0.45; Figs. 4.9b, 4.9e, and 4.9f). Nonetheless, the relationship is somewhat weaker and uncertainty is greater as indicated by the larger scatter between the $\text{SPO}'^{\text{NP}}_{\text{JJA}}$ and $\text{Niño3}'_{\text{NDJ(+1)}}$ indices versus those in the CESM1 (compare Fig. 4.9a and Fig. 4.9b).

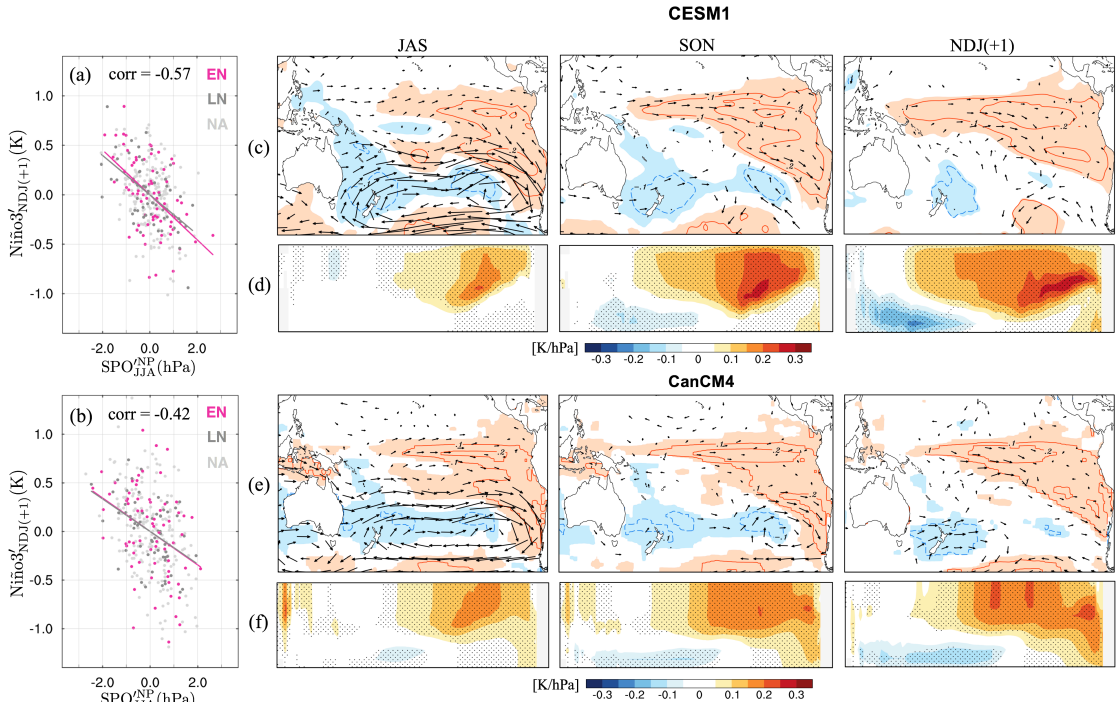

Figure 4.9 (a) Scatter plot of the $\text{SPO}'^{\text{NP}}_{\text{JJA}}$ versus $\text{Niño3}'_{\text{NDJ(+1)}}$. Regressions of the JJA, September-November (SON), and NDJ(+1) (c) SSTA′ (shading, °C/hPa) and U_{850}' (vector, m/s hPa), (d) equatorial (5°N-5°S) T_{sub}' (shading, °C/hPa) onto the non-standardized $\text{SPO}'^{\text{NP}}_{\text{JJA}}$ in CESM1. (b, e, f) are the same as (a, c, d), but for CanCM4. Only the $\text{SPO}'^{\text{NP}}_{\text{JJA}}$ precedes the major ENSO events are included in (c)-(f). Positive (negative) values represented by solid (dashed) contours. Zero contour omitted. Stippling and shading as in Fig. 4.8.

In order to check how much of the ENSO ensemble spread is forced by the $\text{SPO}'^{\text{NP}}_{\text{JJA}}$ or driven by other processes, regressions of the JJA member spread of

atmospheric and oceanic fields onto the non-standardized $\text{Niño3}'_{\text{NDJ(+1)}}$ index are shown in Figure 4.10. The conspicuous agreement of the SLPA pattern with the $\text{SPO}'^{\text{NP}}_{\text{JJA}}$ is yet another confirmation that the spread of ENSO forecast can be reasonably explained by the $\text{SPO}'^{\text{NP}}_{\text{JJA}}$ (Figs. 4.10a and 4.10b). However, compared to the $\text{SPO}'^{\text{NP}}_{\text{JJA}}$-driven pattern shown in Fig. 4.9, the spatial structure of the SSTA′ is different in the CanCM4 (Figs. 4.10c and 4.10d). The stronger loading in the eastern equatorial Pacific indicates an increasing possibility for the ensemble member simulating a greater equatorial warming in JJA to predict a stronger El Niño event in the following winter. While this does not rule out the influence of the $\text{SPO}'^{\text{NP}}_{\text{JJA}}$, the subsurface T_{sub}' dipole indicates the contribution of the oceanic Kelvin waves (Fig. 4.10f), accounting for the greater uncertainty in the CanCM4 (Fig. 4.9b).

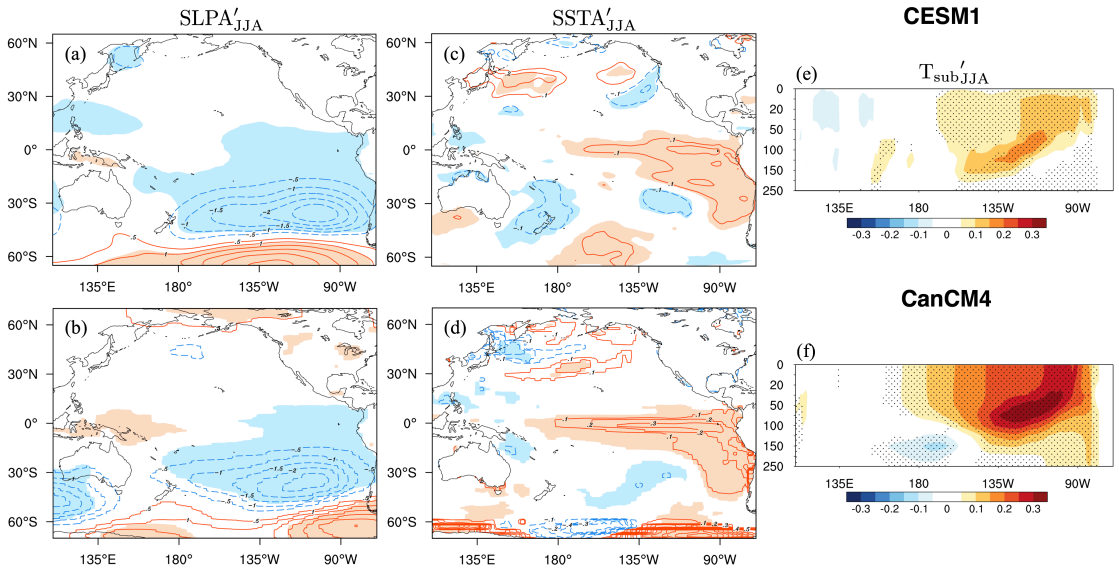

Figure 4.10 Regressions of the JJA (a) SLPA′ (hPa/°C), (c) SSTA′ (°C/°C), and (e) equatorial (5°N-5°S) T_{sub}' (°C/°C) onto the non-standardized $\text{Niño3}'_{\text{NDJ(+1)}}$ in CESM1. (b, d, f) are the same as (a, c, e), but for CanCM4. Only the major ENSO events are included. Positive (Negative) values represented by solid (dashed) contours. Zero contour omitted. Stippling and shading as in Fig. 4.8.

4.3.3 Role of SPO in ENSO Predictability and Asymmetry

The above analyses suggest that although tropical SSTA during austral winter remotely forces the SPO_{JJA}, the magnitude and pattern of the SPO_{JJA} are strongly regulated by extratropical South Pacific internal variability (Figs. 4.5, 4.7, 4.8). The SPO is capable of modulating of the climatological southeasterly trade winds (Fig. 4.4) and exciting stochastic equatorial wind stresses and initiate coupled instability that grows into ENSO-like structure by the Bjerknes feedback (Fig. 4.9). The greatest influence of the SPO_{JJA} is located in the eastern equatorial Pacific (Fig. 4.9). Differing from the North Pacific where the ENSO-forced pattern (i.e., Pacific-North American pattern; PNA) and the internal mode modulating the tropical Pacific (i.e., NPO) are orthogonal, the ENSO-forced and the internal mode in the South Pacific (i.e., SPO) project onto similar spatial structure and account for comparable amount of variability (Fig. 4.5). Thus, the tropical Pacific SSTA forcing and the forced South Pacific SLPA could produce a fast positive feedback. Given that the forecast models suffer from a common systematic bias whereby the SSTA associated with the EP-type El Niño shift westward with increasing lead time (e.g., *Hendon et al.* 2009; *Zhao and Hendon* 2009), the magnitude of the full SPO_{JJA} may offer a plausible pathway to improve the prediction of subsequent ENSO development and particularly the flavor of ENSO with 6-month lead in real world.

To test this assertion, we conduct a simple prediction exercise. For all El Niño identified since 1948 using our definition (see Section 4.2), the strength and phase of the full SPO_{JJA} index is used to predict if an EP or CP event would ensue. That is, if the SPO_{JJA} index is greater (less) than 1σ, an EP (a CP)-type event is predicted. The verification for our prediction follows the characterization of ENSO events as in *Yeh et*

al. (2009), though the overall results are insensitive to other designations (e.g., those used in *Yu et al.* 2012). Table 4.3 indicates that our simple prediction scheme identifies correctly the types of 74% (17 out of 23) of all observed El Niño events since 1948. This finding suggests that the SPO is a reliable (but not absolute) predictor for the type of ENSO event that will ensue with a 3-6 month lead.

Table 4.3 All major El Niño events (23 events, first column), their types (second column; see text for definition) and their types predicted by SPO (third column). Specifically, when the SPO_{JJA} index is greater (less) than 1σ, then a(n) EP (CP) El Niño is predicted.

Year	Type	Predicted by SPO_{JJA}	Year	Type	Predicted by SPO_{JJA}
1951	EP	√	1987	EP	√
1957	EP	√	1990	CP	√
1963	EP	×	1991	EP	×
1965	EP	√	1994	CP	√
1968	CP	√	1997	EP	√
1969	EP	×	2002	CP	×
1972	EP	√	2004	CP	√
1976	EP	√	2006	EP	×
1977	CP	√	2009	CP	√
1979	EP	√	2014	CP	√
1982	EP	√	2015	EP	×
1986	EP	√	Total		17/23 = 74%

Aside from identifying the flavor of warm ENSO events, the SPO may also play a role for La Niña events and the observed spatial asymmetries between El Niño and La Niña events. To examine this, we compute the asymmetric pattern between El Niño and La Niña (*Larkin and Harrison* 2002; *Anderson et al.* 2013) - i.e., the composite difference between SSTA during El Niño events and the inverse (i.e., multiplied by -1) of SSTA during La Niña events. Figure 4.12 shows the results of the composite differences for all events (Fig. 4.12a) and events conditioned by the phase and strength

of the SPO (Figs. 4.12b-c). When examining all events, the spatial difference in SSTA is minimal and statistically insignificant (Fig. 4.12a). But, when we examine the composite difference for events where magnitude of the SPO_{JJA} is greater than 1σ, the asymmetry between El Niño and La Niña is clearly visible with statistically significant differences in the easternmost tropical Pacific and near the dateline (Fig. 4.12b; stippling). For cases when the magnitude of the SPO is less than 1σ, the spatial patterns of the El Niño and La Niña SSTA match fairly well (i.e., small differences) with significant differences restricted to the far eastern tropical Pacific (Fig. 4.12c). Hence, along with being a potential discriminant for the flavor of a warm ENSO event, the SPO may also play a role in the asymmetrical structure of warm and cold ENSO events.

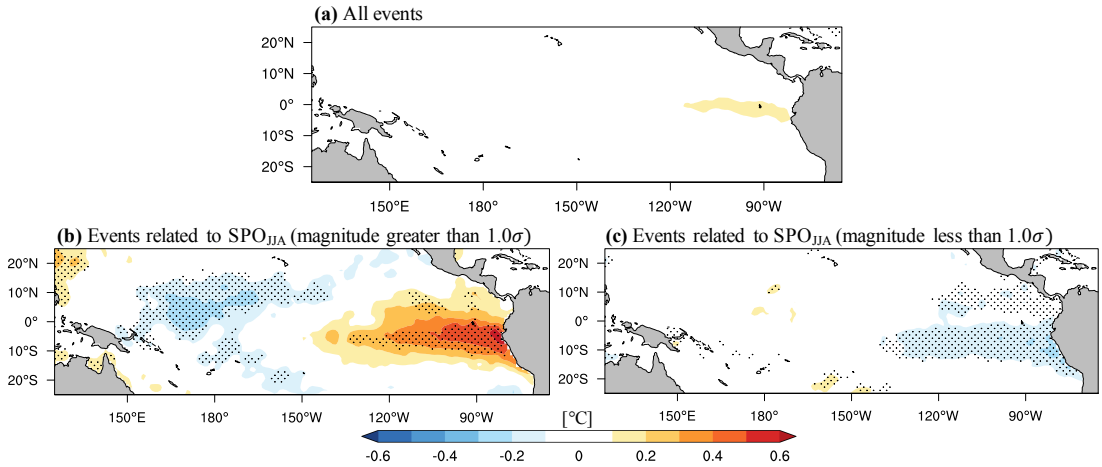

Figure 4.11 (a) Difference between the DJF-mean SSTA (°C) for all El Niño events and the inverted DJF-mean (i.e., multiplied by -1) for all La Niña events. (b) As in (a) but for only El Niño (La Niña) events when the SPO_{JJA}>1σ (SPO_{JJA}<1σ). (c) As in (a) but for El Niño and La Niña events when SPO_{JJA}<1σ. Contour interval 0.1°C. Stippling indicates composite differences that are significantly different from each other at the p<0.05 level according to a two-tailed Student's *t* test.

4.4 Chapter Summary and Discussion

In this chapter, we present evidence that although the tropical SSTA in the austral winter can remotely influence SLPA in the extratropical South Pacific, the

magnitude and pattern of the SLPA are strongly regulated by the inherently atmospheric noise (Figs. 4.5, 4.7). The South Pacific atmospheric internal variability associated with the South Pacific Oscillation (SPO), featuring by a large-scale meridional SLPA seesaw between the subtropics and higher-latitudes (Fig. 4.3), contributes significantly to the development of the following ENSO events (Figs. 4.6, 4.9) and provides great implications for the seasonal prediction of the flavors of ENSO events (Fig. 4.11; Table 4.3). Furthermore, the $\mathrm{SPO}'^{\mathrm{NP}}_{\mathrm{JJA}}$ is a primary source of uncertainty for ENSO prediction in the NMME hindcasts explored here (Fig. 4.10). Given that internal variability is, by definition, unpredictable even with a perfect model, the SPO variability might serve as a natural limit for ENSO prediction.

Analogous to the westerly wind bursts (*Chen et al.* 2015), the synoptic-scale surface easterly wind bursts in the central equatorial Pacific were suggested by several recent studies to play an important role in the onset of La Niña events (*Choidi and Harrison* 2015) and in the stalling of the some El Niño events (e.g., *Min et al.,* 2014; *Hu and Fedorov* 2016; *Levine and McPhaden* 2016; *Choidi and Harrison* 2017). *Hu and Fedorov* (2016) used model experiments to illustrate that a surplus of westerly wind bursts during boreal spring and the balance between westerly and easterly wind bursts (yielding small net wind stress anomaly) during boreal summer accounts for the early development and mid-year reversal of El Niño-like SSTA development during the 2014/2015 event. The connections between the various characteristics of the easterly wind bursts (i.e., occurrence, strength, timing, persistence, zonal extent) and $\mathrm{SPO}_{\mathrm{JJA}}$ thus warrant further study.

Chapter 5: Conclusion and Future Work

5.1 Conclusion

The El Niño-Southern Oscillation (ENSO) phenomenon, a coupled climate mode characterized by anomalies sea surface temperature (SST) anomalies (SSTA) across the equatorial pacific and changes in tropical convection patterns, considerably modulates global atmospheric circulations and influences both local and remote climates. The effects of the temporal and spatial structures of the tropical Pacific SSTA on the global teleconnections call for better understanding and predictability of the occurrence, intensity, and spatial structure of ENSO events.

This main finding of this work illustrates that greater seasonal prediction of ENSO state is possibly achieved by incorporating certain South Pacific ENSO precursors. We have presented evidence from reanalysis products and a collection of state-of-the-art climate models that the South Pacific atmospheric internal variability imposes substantial influences on the various behaviors of ENSO events. Differing from the North Pacific where ENSO teleconnections (i.e., Pacific-North American pattern; PNA) and the atmospheric internal mode (i.e., North Pacific Oscillation; NPO) are nearly orthogonal to each other, the South Pacific atmospheric tropically-forced and internal modes project onto a similar SLPA structure, termed the South Pacific Oscillation (SPO) in the present thesis (Figs. 3.3, 4.3). Akin to the NPO, the SPO is characterized by a large-scale meridional SLPA seesaw between the subtropics and higher-latitudes. The northern node of SPO physically modulates the strength and location of the South Pacific subtropical High. Detailed conclusions for each chapter are provided below.

In Chapter 3, we assessed the seasonality of the atmosphere-ocean coupled mode intrinsic to the extratropical South Pacific – i.e., South Pacific Meridional Mode (SPMM; Fig. 3.2). The seasonality is of great importance for the SPMM's role in influencing tropical Pacific variability. The response of the South Pacific subtropical SSTA to the atmospheric forcing [i.e., the wind-evaporation-SST (WES) feedback] is most energetic during the austral summer owing to the seasonal cycle of the oceanic mixed layer depth and the overall lower amplitude of the mean seasonal cycle in South Hemisphere atmospheric variability compared to that of the Northern Hemisphere (Fig. 3.4). As a result, the seasonality of the wind and SST components of the SPMM vary out of phase (Fig. 3.2c). The WES feedback and associated SPMM dynamics thus are most active during the austral summer/fall, providing a favorable timing for subtropical SST and wind anomalies initiated by the SPO (Fig. 3.3) to propagate equatorward into the cold tongue region (Fig. 3.10). The resulting tropical anomalies may interact constructively or destructively with the concurrent North Pacific Meridional Mode-(NPMM-)induced anomalies in the warm pool region, subsequently shaping the occurrence, temporal evolution, amplitude, and potentially the longitudinal position of the maximum SSTA of the resulting ENSO events (Figs. 3.11-3.13). Both Pacific Meridional Modes (PMMs) appear to be most efficient at triggering El Niño when the subsurface is preconditioned with the buildup of heat content during the austral fall and winter (Fig. 3.14). The boreal winter Pacific SSTA can be feasibly forecasted when using the boreal spring PMMs as predictors (Figs. 3.15-3.16). Although the PMMs are captured reasonably by the state-of-art climate models, the contributions of the slowly

evolving ocean heat content dominants over the PMMs in the equatorial Pacific (Fig. 3.15).

Although combining the two PMMs and WWV enhances ENSO prediction, where the maximum equatorial Pacific SSTA resides remains uncertain. Hence, we investigated the South Pacific austral winter climate variability in Chapter 4, as this is the time when the South Pacific atmospheric variability is strongest. Using reanalysis and NMME hindcasts, we tested the previously-published argument that the austral winter SLPA are actually a response to the developing tropical Pacific SSTA due to the local seasonality. Instead, our analyses indicated that both the spatial structure and amplitude of the austral winter ENSO teleconnections in the South Pacific are strongly regulated by the atmospheric internal variability, namely the SPO (Figs. 4.3, 4.5, 4.7). By regulating the discharge of the ocean heat content over the eastern tropics (Figs. 4.4, 4.6) and exciting stochastic equatorial westerly wind stress (Fig. 4.8), the positive phase of the austral winter SPO initiates coupled instability that thereafter grows into ENSO-like structure via the Bjerknes feedback (Fig. 4.9). Furthermore, the austral winter SPO provides great implications for the seasonal prediction of the ENSO flavors. In NMME hindcasts, the austral winter SPO is the main atmospheric pattern responsible for the ensemble spread of ENSO prediction (Fig. 4.10). Given the internal variability is unpredictable even with a perfect model, the austral winter SPO might serve as an intrinsic limit for ENSO prediction.

Collectively, we extend the North Pacific-tropical Pacific framework put forth by *Di Lorenzo et al.* (2015) to include the South Pacific, providing a new framework to understand the relationship between the extratropical Pacific internal variability and

ENSO events (Figure 5.1). Given the uncertainties in NPMM-ENSO relationship (Larson and Kirtman 2014, 2015) and the fact that the NPMM appears to be a precursor for both EP and CP events (Fig. 4.1), this paradigm incorporates the South Pacific ENSO precursors in the austral summer and winter to enhance the prediction of the occurrence, intensity, evolution, and flavors of ENSO events.

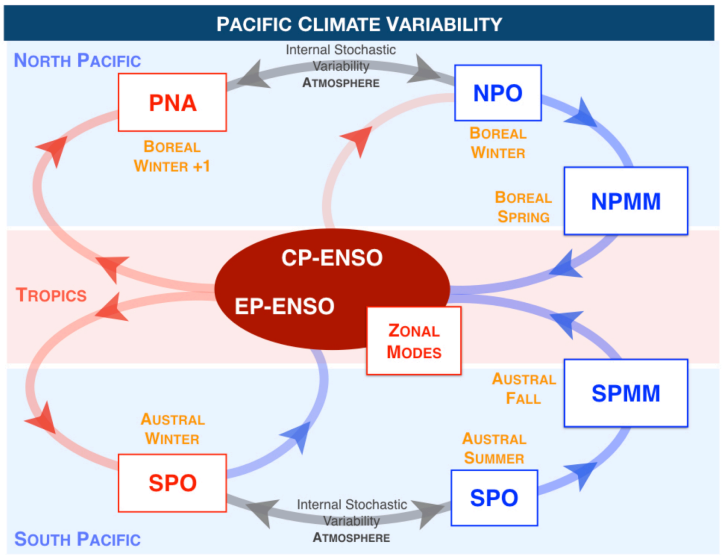

2 ENSO Amplification: Interferences between NPMM- and SPMM-induced tropical anomalies and the tropical preconditioning (e.g., WWV) shape the ENSO diversity and predictability

3 ENSO Intensity and Flavor: Although significantly modulated by the tropical Pacific SSTA, SPO during austral winter contains a great portion of internal variability that modulates the development of the subsequent ENSO events

1 Extratropical Stochastic Forcing: SPO energizes the SPMM during the austral summer to transport the subtropical anomalies into the central-eastern tropics and trigger ENSO events

Figure 5.1 Diagram of ENSO variability. The North Pacific framework is put forth by *Di Lorenzo et al.* (2015).

5.2 Future Work

The results presented in previous chapters are important for understanding and predicting the tropical Pacific variability on interannual scales. They also provide more interesting and important questions for future studies. In particular, two key topics are highlighted below.

Impact of the SPMM on Pacific decadal variability

Given that the dynamics of the PMMs are consistent with a red noise process without any preferential timescales, the PMMs may also play an important role in energizing the decadal and multi-decadal energy in the tropical Pacific (*Vimont et al.* 2002; *Clement et al.* 2011; *Di Lorenzo et al.* 2015; *Newman et al.* 2016). Additionally, as we did not apply any filtering in the analyses, the high correlation between the un-filtered PMMs and ENSO (Fig. 3.14) indicates that the bulk of Pacific variability is possibly caused by the same mechanism on interannual and decadal timescales.

To examine this a little further, we perform the power spectral and cross-spectral analyses on the PMMs and CTI time series to check the frequency of the PMMs and their relationship to tropical Pacific variability. As shown in Figure 5.2, power spectrum analysis reveals that the dynamics of the PMMs could play a role in tropical Pacific variability at lower frequencies. At the lower frequencies, the observed PMMs show significant periodicities at and longer than ~5 years (Figs. 5.2a-b). The increasing power of PMMs at low-frequencies arises partly from mid-latitude air-sea coupling (*Barsugli and Battisti* 1998; *Vimont et al.* 2002) and partly from tropical Pacific remote forcing (*Furtado et al.* 2012; *Stuecker* 2018). The highly-significant squared coherence between the PMMs and CTI on the interannual timescale (2-4 years) and periods exceeding 6 years suggests that a great amount of the CTI variance at these bands is related to the PMMs (Figs. 5.2e-f, i). The CMIP5 MME agrees with observation but with reduced coherence (Figs. 5.2c-d, g-h). However, the lead time for the PMMs at low-frequency timescales is confined to ~1 year (Figs. 5.2i-j; e.g., *Vimont et al.* 2002; *Okumura* 2013;

Di Lorenzo et al. 2015), suggesting limited predictability. Actual qualification is warrant for future studies.

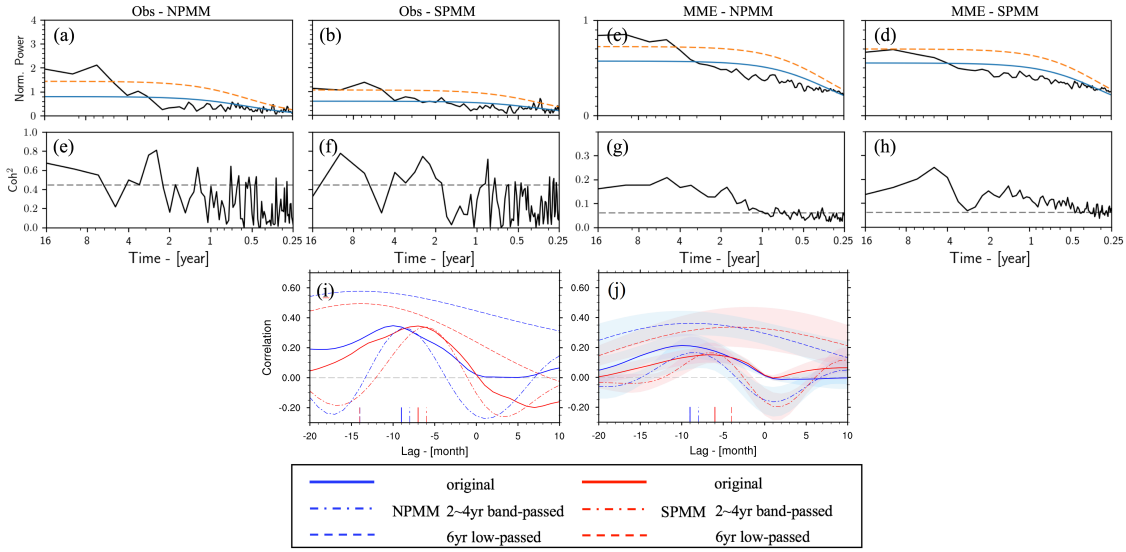

Figure 5.2 (a) Power spectrum (plotted as percent variance; black line) of normalized observed monthly-mean NPMM index. Blue line represents the theoretical red noise power spectrum, and the dashed red line represents the 95% significance curve. (b) As in (a) but for the observed monthly-mean SPMM index. (c) As in (a) but for the CMIP5 MME. (d) As in (b) but for the CMIP5 MME. (e) Squared coherence from the cross-spectral analysis of the monthly-mean NPMM index and the CTI. Dashed grey line denotes the 95% significance level for the squared coherence. (g, h) As in (e, f) but from the cross-spectral analysis of the monthly-mean SPMM index and the CTI. Note the differences of the *y*-axis for the CMIP5 MME versus the reanalysis plots. (i) Lag correlation between the raw (solid), 2~4 yr band-passed (dot-dashed), and 6 yr low-passed (dashed) versions of the NPMM index (blue) and SPMM index (red) and the CTI. Negative (positive) lags indicate that the NPMM/SPMM index leads (lags) the CTI. Corresponding vertical lines on the *x* axis represent the lag with the maximum correlation. (j) As in (i) but for the CMIP5 MME. Red/blue shading in (j) denotes the unit standard deviation across models.

The Sensitivity of SPMM-ENSO relationship to mean state

While we primarily concentrate on the CMIP5 MME in Chapter 3, individual models display a variety with regard to the relation between $SPMM_{FMAM}$ and ENSO. We briefly address the inter-model spread here. We grouped the models analyzed in this study into two groups based on the correlation between the $SPMM_{FMAM}$ and $CTI_{NDJ(+1)}$ within each model compared to the MME correlation. The two groups included

$model_{high\_corr}$ (CanESM2, CNRM-CM5, CSIRO-Mk3-6-0, GFDL-ESM2G, GISS-E2-R, NorESM1-ME) and $model_{low\_corr}$ (CCSM4, HadGEM2-CC, INMCM4, MIROC5, IPSL-CM5A-MR, MPI-ESM-P). We then repeated the analysis in Fig. 3.9 (i.e., lagged regressions of SLPA, SSTA, and wind anomalies onto the $SPMM_{FMAM}$ index) and averaged the results per subset. Figures 5.3a-h display these lag regressions. The most evident differences between the $model_{high\_corr}$ and the $model_{low\_corr}$ models emerge during and after MJJ, when the SSTA and the deepening of thermocline in the eastern tropical Pacific have been established in the $model_{high\_corr}$ models (Fig. 5.3b) but not in the $model_{low\_corr}$ models (Fig. 5.3f). The $model_{high\_corr}$ ($model_{low\_corr}$) exhibit strengthened (weakened) responses of the thermocline slope and equatorial zonal wind anomalies to the SPMM-related forcing, indicating the tropical coupled system is relatively unstable (damped) and the SSTA growth rate is thus greater (weaker). Additionally, we examined the biases in the SST (Fig. 5.3i) and precipitation mean state (Fig. 5.3j). The inter-model spread for these dynamics is likely also associated with the well-documented "cold-tongue" bias in the models, as the system tends to be more unstable where the eastern equatorial SST mean state is warmer and the ascending branch of the Walker circulation shifts eastward (Figs. 5.3i, j; see also *Lübbecke and McPhaden* 2014).

The above analysis highlights the effect of model biases in tropical Pacific SST climatology. On the other hand, this also suggests that the influence of the SPMM on ENSO events is sensitive to the tropical mean state. The WES feedback that controls the growth rate of the PMMs-related SSTA (*Vimont et al.* 2009), exhibits an exponential increase in amplitude because of the nonlinear relationship between SSTA and

evaporation in a warming climate. The increase in the amplitude of NPMM leads to an increase in the coupling between NPMM and ENSO, contributing to the variance of Pacific variability (*Liguori and Di Lorenzo* 2018). Similar analysis can be applied to the SPMM to facilitate the understanding of ENSO variability under different climate state.

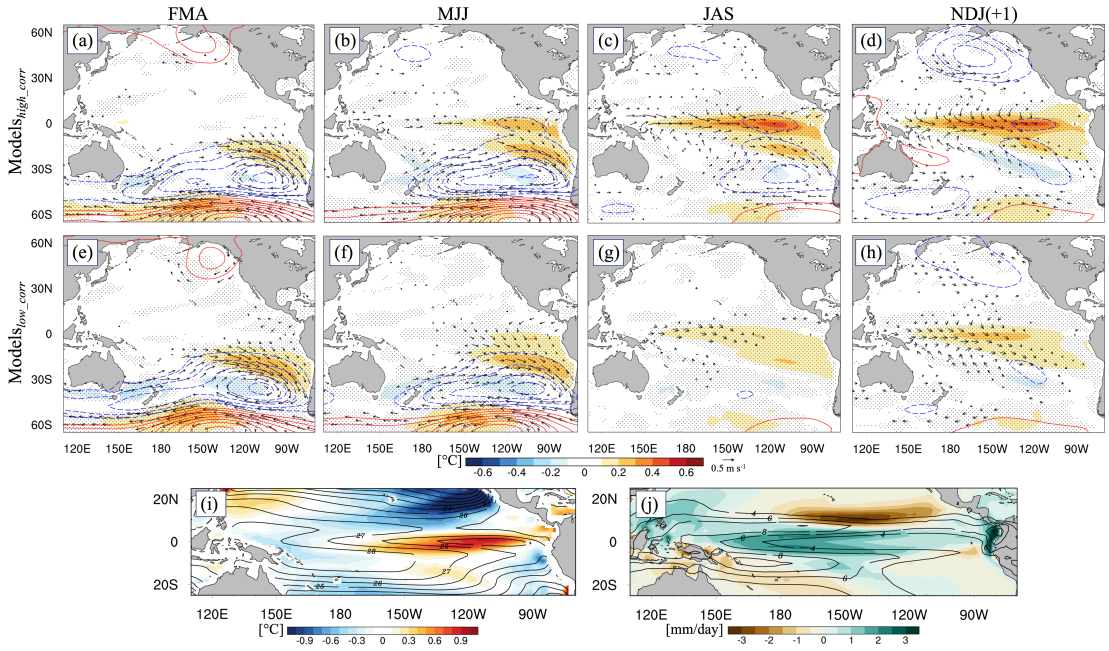

Figure 5.3 (a)-(d) As in Fig. 3.10e-h, but for the ensemble-mean of the model$_{high_corr}$ subset. (e)-(h) Same as (a)-(d) but for the model$_{low_corr}$. Stippling indicates where the SSTA regression coefficients are considered significant ($p < 0.05$ for reanalysis; 4 out of 6 models have the same sign of the regression). (i) Mean February-July SST climatology (black contour, °C) for the model$_{high_corr}$ models and the difference (shading, °C) of the February-July SST climatology between the model$_{high_corr}$ and model$_{low_corr}$ models. (j) As in (i) but for the precipitation (mm/day).

References

Alexander, M. A., I. Blade, M. Newman, J. R. Lanzante, N. C. Lau, and J. D. Scott, 2002: The atmospheric bridge: The influence of ENSO teleconnections on air-sea interaction over the global oceans. *J. Climate*, **15**, 2205–2231, doi:10.1175/1520-0442(2002)015⟨2205:TABTIO⟩2.0. CO;2.

Alexander, M. A., L. Matrosova, C. Penland, J. D. Scott, and P. Chang, 2008: Forecasting Pacific SSTs: Linear inverse model predictions of the PDO. *J. Climate*, **21**, 385–402, doi:10.1175/2007JCLI1849.1.

Alexander, M. A., D. J. Vimont, P. Chang, and J. D. Scott, 2010: The impact of extratropical atmospheric variability on ENSO: Testing the seasonal footprinting mechanism using coupled model experiments. *J. Climate*, **23**, 2885–2901, doi:10.1175/2010JCLI3205.1.

An, S.-I., 2008: Interannual variations of the tropical ocean instability wave and ENSO. *J. Climate*, **21**, 3680–3686, doi:10.1175/ 2008JCLI1701.1.

Anderson, B. T., 2007: On the joint role of subtropical atmospheric variability and equatorial subsurface heat content anomalies in initiating the onset of ENSO events. *J. Climate*, **20**, 1593–1599, doi:10.1175/JCLI4075.1.

Anderson, B. T., and R. C. Perez, and A. Karspeck, 2013: Triggering of El Niño onset through trade wind-induced charging of the equatorial Pacific. *Geophys. Res. Lett.*, 40, 1212–1216, doi:10.1002/grl.50200.

Anderson, B. T., and R. C. Perez, 2015: ENSO and non-ENSO induced charging and discharging of the equatorial Pacific. *Clim. Dyn.*, **45**, 2309–2327, doi:10.1007/s00382-015-2472-x.

Ashok, K., S. K. Behera, S. A. Rao, H. Weng, and T. Yamagata, 2007: El Niño Modoki and its possible teleconnection. *J. Geophys. Res.*, **112**, C11007, doi:10.1029/2006JC003798.

Balmaseda, M. A., K. E. Trenberth, and E. Kallen, 2013: Distinctive climate signals in reanalysis of global ocean heat content. *Geophys. Res. Lett.*, **40**, 1754–1759, doi:10.1002/grl.50382.

Barnston, A. G., M. K. Tippett, M. L. L'Heureux, S. Li, and D. G. DeWitt, 2012: Skill of real- time seasonal ENSO model predictions during 2002-11: Is our capability increasing? *Bull. Amer. Meteor. Soc.*, **93**, 631–651, doi:10.1175/BAMS-D-11-00111.1.

Barsugli, J. J., and D. S. Battisti, 1998: The basic effects of atmosphere-ocean thermal coupling on midlatitude variability. *J. Atmos. Sci.*, **55**, 477–493.

Barsugli, J. J., and P. D. Sardeshmukh, 2002: Global atmospheric sensitivity to tropical SST anomalies throughout the Indo-Pacific basin. *J. Climate*, **15**, 3427–3442.

Bellenger, H., E. Guilyardi, J. Leloup, M. Lengaigne, and J. Vialard, 2014: ENSO representation in climate models: from CMIP3 to CMIP5. *Climate Dyn.*, **42**, 1999–2018, doi: 10.1007/s00382-013-1783-z.

Bretherton, C. S., C. Smith, and J. M. Wallace, 1992: Distinctive climate signals in reanalysis of global ocean heat content. *J. Climate*, **5**, 541–560, doi: 10.1175/1520-0442(1992)005⟨0541:AIOMFF⟩2.0.CO;2.

Bretherton, C. S., M. Widmann, V. P. Dymnikov, J. M. Wallace, and I. Blade, 1999: The effective number of spatial degrees of freedom of a time-varying field. *J. Climate*, **12**, 1990-2009, doi: 10.1175/1520-0442(1999)012⟨1990:TENOSD⟩2.0.CO;2.

Cai, W., I. G. Watterson, 2002: Modes of Interannual Variability of the Southern Hemisphere Circulation Simulated by the CSIRO Climate Model. *J. Climate*, **15**, 1159-1174, doi: 10.1175/1520-0442(2002)015<1159:MOIVOT>2.0.CO;2.

Capotondi, A., and Coauthors, 2015a: Understanding ENSO diversity. *Bull. Amer. Meteor. Soc.*, **96**, 921–938, doi: 10.1175/BAMS-D-13-00117.1.

Capotondi, A., and P. D. Sardeshmukh, 2015b: Optimal precursors of different types of ENSO events. *Geophys. Res. Lett.*, **42**, 9952-9960, doi: 10.1002/2015GL066171.

Carton, J. A., and B. S. Giese, 2008: A reanalysis of ocean climate using Simple Ocean Data Assimilation (SODA). *Mon. Wea. Rev.*, **136**, 2999–3017.

Chang, P., L. Ji, H. Li, and M. Flugel, 1996: Chaotic dynamics versus stochastic processes in El Niño-Southern Oscillation in coupled ocean–atmosphere models. *Physica D*, **98**, 301–320.

Chang, P., L. Zhang, R. Saravanan, D. J. Vimont, J. C. H. Chiang, L. Ji, H. Seidel, and M. K. Tippett, 2007: Pacific meridional mode and El Niño-Southern Oscillation. *Geophys. Res. Lett.*, **34**, n/a–n/a, doi:10.1029/2007GL030302.

Chen, D., and Coauthors, 2015: Strong influence of westerly wind bursts on El Niño diversity. *Nat. Geosci.*, **8**, 339–345, doi:10.1038/ ngeo2399.

Chiang, J. C. H., and D. J. Vimont, 2004: Analogous Pacific and Atlantic meridional modes of tropical atmosphere-ocean variability. *J. Climate*, **17**, 4143–4158.

Chiodi, A. M., D. E. Harrison, 2015: Equatorial Pacific easterly wind surges and the onset of La Niña events. *J. Climate*, **28**, 776–792, doi:10.1175/JCLI-D-14-00227.1

Chiodi, A. M., D. E. Harrison, 2017: Observed El Niño SSTA development and the effects of Easterly and Westerly Wind events in 2014-2015. *J. Climate*, **30**, 1505-1519, doi: 10.1175/JCLI-D-16-0385.1.

Clement, A., P. DiNezio, and C. Deser, 2011: Rethinking the ocean's role in the Southern Oscillation. *J. Climate*, **24**, 4056–4072, doi:10.1175/2011JCLI3973.

Compo, G. P., and Coauthors, 2011: The twentieth century reanalysis project. *Quart. J. Roy. Meteor. Soc.*, **137**, 1–28, doi:10.1002/qj.776.

Dayan H., J. Vialard, T. Izumo 2014, Does sea surface temperature outside the tropical Pacific contribute to enhanced ENSO predictability?. *Climate Dyn.*, **43**, 1311-1325, doi:10.1007/s00382-013-1946-y.

Dee, D. P., and Coauthors, 2011: The ERA-Interim reanalysis: Configuration and performance of the data assimilation system. *Quart. J. Roy. Meteor. Soc.*, **137**, 553–597, doi:10.1002/qj.828.

Deser, C., and J. M. Wallace, 1990: Large-scale atmospheric circulation features of warm and cold episodes in the tropical Pacific. *J. Climate*, **3**, 1254–1281.

Deser, C., and Coauthors, 2012: ENSO and Pacific decadal variability in the Community Climate System Model version 4. *J. Climate*, **25**, 2622–2651, doi:10.1175/JCLI-D-11-00301. 1.

Deser, C., I. R. Simpson, K. A. Mckinnon, and A. S. Phillips, 2017: The northern hemisphere extratropical atmospheric circulation response to ENSO: how well do we know it and how do we evaluate models accordingly?. *J. Climate*, **30**, 5059-5082, doi: 10.1175/JCLI-D-16-0844.1.

Di Lorenzo, and Coauthors, 2010: Central Pacific El Niño and decadal climate change in the North Pacific. *Nat. Geosci.*, **3**, 762–765.

Di Lorenzo, E., G. Liguori, N. Schneider, J. C. Furtado, B. T. Anderson, and M. A. Alexander, 2015: ENSO and meridional modes: A null hypothesis for Pacific climate variability. *Geophys. Res. Lett.*, **42**, 9440–9448, doi:10.1002/2015GL066281.

DiNezio, P. N., C. Deser, Y. Okumura, and A. Karspeck, 2017: Predictability of 2-year La Niña events in a coupled general circulation model. *Climate Dyn.*, **49**, 4237–4261, doi:10.1007/ s00382-017-3575-3.

Ding, R., J. Li, Y.-H. Tseng, 2015a: The Victoria mode in the North Pacific linking extratropical sea level pressure variations to ENSO. *J. Geophys. Res.*, **120**, 27-45, doi: 10.1002/2014JD022221.

Ding, R., J. Li, and Y.-H. Tseng, 2015b: The impact of South Pacific extratropical forcing on ENSO and comparisons with the North Pacific. *Climate Dyn.*, **44**, 2017–2034, doi:10.1007/ s00382-014-2303-5.

Elsner, J. B., and C. P. Schmertmann, 1994: Assessing forecast skill through cross validation. *Wea. Forecasting*, **9**, 619–624.

Fedorov, A. V., 2002: The response of the coupled tropical ocean–atmosphere to westerly wind bursts. *Quart. J. Roy. Meteor. Soc.*, **128**, 1–23, doi:10.1002 /qj.200212857901.

Feldstein, S. B., 2000: The timescale, power spectra, and climate noise properties of teleconnection patterns. *J. Climate*, **13**, 4430–4440.

Furtado, J. C., E. Di Lorenzo, B. T. Anderson, and N. Schneider, 2012: Linkages between the North Pacific Oscillation and central tropical Pacific SSTs at low frequencies. *Climate Dyn.*, **39**, 2833– 2846, doi:10.1007/s00382-011-1245-4.

Furtado, J. C., E. D. Lorenzo, N. Schneider, and N. A. Bond, 2011: North Pacific decadal variability and climate change in the IPCC AR4 models. *J. Climate*, **24**, 3049–3067, doi:10.1175/2010JCLI3584.1.

Gebbie, G., I. Eisenman, A. Wittenberg, and E. Tziperman, 2007: Modulation of westerly wind bursts by sea surface temperature: A semistochastic feedback for ENSO. *J. Atmos. Sci.*, **64**, 3281–3295, doi:10.1175/JAS4029.1.

Hendon, H. H., E. Lim, G. Wang, O. Alves, and D. Hudson, 2009: Prospects for predicting two flavors of El Niño, *Geophys. Res. Lett.*, **36**, L19713, doi:10.1029/2009GL040100.

Horel, J. D., and J. M. Wallace, 1981: Planetary-scale atmospheric phenomena associated with the Southern Oscillation. *Mon. Wea. Rev.*, **109**, 813–829, doi:10.1175/1520-0493(1981)109,0813: PSAPAW.2.0.CO;2.

Hoskins, B. J., and D. J. Karoly, 1981: The steady linear response of a spherical atmosphere to thermal and orographic forcing. *J. Atmos. Sci.*, **38**, 1179–1196, doi: 10.1175/ 1520-0469(1981)038,1179:TSLROA.2.0.CO;2.

Hu, S., and A. V. Fedorov, 2016: Exceptionally strong easterly wind burst stalling El Niño of 2014. *Proc. Natl. Acad. Sci. U.S.A.*, **113**, 2005–2010, doi:10.1073/pnas.1514182113.

Imada, Y., H. Tatebe, M. Watanabe, M. Ishii, and M. Kimoto, 2016: South Pacific influence on the termination of El Niño in 2014. *Sci. Rep.*, **6**, 30341, doi:10.1038/srep30341.

Jin, F.-F., 1997: An equatorial ocean recharge paradigm for ENSO. Part I: Conceptual model. *J. Atmos. Sci.*, **54**, 811–829.

Jin, E. K., and Coauthors, 2008: Current status of ENSO prediction skill in coupled ocean–atmosphere models. *Climate Dyn.*, **31**, 647–664, doi: 10.1007/s00382-008-0397-3.

Jin, D., and B. P. Kirtman, 2009: Why the Southern Hemisphere ENSO responses lead ENSO. *J. Geophys. Res.,* **114**, doi:10.1029 /2009JD012657.

Johnson, N. C., 2013: How many ENSO flavors can we distinguish?, *J. Climate.*, **26**, 4816–4827, doi:10.1175/JCLI-D-12-00649.1.

Kalnay, E., and Coauthors, 1996: The NCEP/NCAR 40-year reanalysis project. *Bull. Amer. Meteor. Soc.*, **77**, 437–471, doi:10.1175/1520-0477(1996)077⟨0437:TNYRP⟩2.0.CO;2.

Kao, H.-Y., and J.-Y. Yu, 2009: Contrasting Eastern-Pacific and Central-Pacific types of ENSO. *J. Climate*, **22**, 615–632, doi:10.1175/2008JCLI2309.1.

Kara, A. B., P. A. Rochford, and H. E. Hurlburt, 2003: Mixed layer depth variability over the global ocean. *J. Geophys. Res.*, **108**, 3079, doi:10.1029/2000JC000736.

Karnauskas, K. B., 2013: Can we distinguish canonical El Niño from Modoki?, *Geophys. Res. Lett.*, **40**, 5246–5251, doi:10.1002/grl.51007.

Kidson, J. W., and J. A. Renwick, 2002: The Southern Hemisphere evolution of ENSO during 1981-99. *J. Climate*, **15**, 847–863, doi: 10.1175/1520-0442(2002)015⟨0847: TSHEOE⟩2.0.CO;2.

Kiladis, G. N., and K. C. Mo, 1999: Interannual and intraseasonal variability in the Southern Hemisphere. *Meteorology of the Southern Hemisphere*, D. J. Karoly and D. G. Vincent, Eds., Amer. Meteor. Soc., 307–336.

Kim, S. T., and J.-Y. Yu, 2012: The two types of ENSO in CMIP5 models. *Geophys. Res. Lett.*, **39**, L11704, doi:10.1029/2012GL052006.

Kirtman, B. P., and Coauthors, 2014: The North American Multimodel Ensemble: Phase-1 seasonal-to-interannual prediction; phase-2 toward developing intraseasonal prediction. *Bull. Amer. Meteor. Soc.*, **95**, 585–601, doi:10.1175/BAMS-D-12-00050.1.

Kug, J.-S., and F.-F. Jin, and S.-I. An, 2009: Two types of El Niño events: Cold tongue El Niño and warm pool El Niño. *J. Climate*, **22**, 1499–1515, doi:10.1175/2008JCLI2624.1.

Kleeman, R., and A. M. Moore, 1997: A theory for the limitation of ENSO predictability due to stochastic atmospheric transients, *J. Atmos. Sci.*, **54**, 753–767, doi:10.1175/1520-0469(1997)054<0753:ATFTLO>2.0.CO;2.

Lai W. C., M. Herzog, H. F. Graf, 2017: ENSO forecasts near the spring predictability barrier and possible reasons for the recently reduced predictability. *J. Climate,* 31, 815-838, doi: 10.1175/JCLI-D-17-0180.1.

Landsea, C. W., and J. A. Knaff, 2000: How much skill was there in forecasting the very strong 1997–98 El Niño?, *Bull. Am. Meteorol. Soc.*, **15**, 1203–1215.

Larkin, N. K., and D. E. Harrison, 2002: ENSO warm (El Niño) and cold (La Niña) event life cycles: Ocean surface anomaly patterns, their symmetries, asymmetries, and implications. *J. Climate*, **15**, 1118–1140, doi:10.1175/1520-0442(2002)015,1118: EWENOA.2.0.CO;2.

Larkin, N. K., and D. E. Harrison, 2005: On the definition of El Niño and associated seasonal average U.S. weather anomalies. *Geophys. Res. Lett.*, **32**, L13705, doi:10.1029/2005GL022738.

Larson, S., and B. Kirtman, 2013: The Pacific Meridional Mode as a trigger for ENSO in a high- resolution coupled model. *Geophys. Res. Lett.*, **40**, 3189–3194, doi:10.1002/grl.50571.

Larson, S., and B. Kirtman, 2014: The Pacific meridional mode as an ENSO precursor and predictor in the North American multimodel ensemble. *J. Climate*, **27**, 7018–7032, doi:10.1175/JCLI-D-14-00055.1.

Larson, S., and B. Kirtman, 2015: An alternate approach to ensemble ENSO forecast spread: Application to the 2014 forecast. *Geophys. Res. Lett.*, **42**, 9411–9415, doi:10.1002/2015GL066173.

Latif, M., T. P. Barnett, M. A. Cane, M. Flügel, N. E. Graham, H. von Storch, J.-S. Xu, and S. E. Zebiak, 1994: A review of ENSO prediction studies. *Climate Dyn.*, **9**, 167–179, doi:10.1007/BF00208250.

Lee, S. K., H. Lopez, E. S. Chung, P. DiNezio, S. W. Yeh, A. T. Wittenberg, 2018: On the fragile relationship between El Niño and California rainfall. *Geophys. Res. Lett.*, **45**, 907-915, doi: 10.1002/2017GL076197.

Levine, A. F. Z., and M. J. McPhaden, 2016: How the July 2014 easterly wind burst gave the 2015–2016 El Niño a head start. *Geophys. Res. Lett.,* **43**, 6503–6510, doi:10.1002/2016GL069204.

Lin, C. Y., J. Y. Yu, and H. H. Hsu, 2015: CMIP5 model simulations of the Pacific meridional mode and its connection to the two types of ENSO. *Int. J. Climatol.*, **35**, 2352–2358, doi:10.1002/joc.4130.

Linguori, G., and E. Di Lorenzo, 2018: Meridional Modes and Increasing Pacific Decadal Variability Under Anthropogenic Forcing. *Geophys. Res. Lett.,* **45**, 1944–8007, doi: 10.1002/2017GL076548.

Linkin, M. E., and S. Nigam, 2008: The North Pacific Oscillation-West Pacific teleconnection pattern: Mature-phase structure and winter impacts. *J. Climate*, **21**, 1979–1997, doi:10. 1175/2007JCLI2048.1.

Liu, Z., and M. Alexander, 2007: Atmospheric bridge, oceanic tunnel, and global climatic teleconnections. *Rev. Geophys.*, **45**, RG2005, doi:10.1029/2005RG000172.

Lübbecke, J. F., and M. J. McPhaden, 2014: Assessing the Twenty-First-Century Shift in ENSO Variability in Terms of the Bjerknes Stability Index. *J. Climate*, **7**, 2577-2587, doi:10.1175/JCLI-D-13-00438.1.

Luo, J. J., S. Masson, S. Behera, P. Delecluse, S. Gualdi, A. Navarra, and T. Yamagata, 2003: South Pacific origin of the decadal ENSO-like variation as simulated by a coupled GCM. *Geophys. Res. Lett.*, **30**, 2250, doi:10.1029/2003GL018649.

McGregor, S., N. J. Holbrook, and S. B. Power, 2009a: The response of a stochastically forced ENSO model to observed off-equatorial wind stress forcing, *J. Climate.*, **22**, 2512–2525, doi:10.1175/2008JCLI2387.1.

McGregor, S., A. S. Gupta, N. J. Holbrook, and S. B. Power, 2009b: The modulation of ENSO variability in CCSM3 by extratropical Rossby waves, *J. Climate*, **22**, 5839–5853, doi:10.1175/2009JCLI2922.1.

McPhaden, M. J., 2003: Tropical Pacific Ocean heat content variations and ENSO persistence barriers. *Geophys. Res. Lett.*, **30**, 1480, doi:10.1029/2003GL016872.

Matei, D., N. Keenlyside, M. Latif, and J. Jungclaus, 2008: Subtropical forcing of tropical Pacific climate and decadal ENSO modulation. *J. Climate*, **21**, 4691–4709, doi:10.1175/2008JCLI2075.1

Meehl, G. A., H. Loon, and J. M. Arblaster, 2017: The role of the Southern Hemisphere semiannual oscillation in the development of a precursor to central and eastern Pacific Southern Oscillation warm events. *Geophys. Res. Lett.*, **44**, 6959-6965, doi: 10.1002/2017GL073832.

Meinen, C. S., and M. J. McPhaden, 2000: Observations of warm water volume changes in the equatorial Pacific and their relationship to El Niño and La Niña. *J. Climate*, **13**, 3551–3559, doi:10.1029/2003GL016872, 1480.

Merryfield, W. J., and Coauthors, 2013: The Canadian seasonal to interannual prediction system. Part I: Models and initialization. *Mon. Wea. Rev.*, **141**, 2910–2945.

Min, Q., J. Su, and R. Zhang, 2017: Impact of the South and North Pacific Meridional Modes on the El Niño-Southern Oscillation: Observational analysis and comparison. *J. Climate*, **30**, 1705–1720, doi:10.1175/JCLI-D-16-0063.1.

Min, Q., J. Su, R. Zhang, and X. Rong, 2015: What hindered the El Niño pattern in 2014? *Geophys. Res. Lett.*, **42**, 6762–6770, doi:10.1002/2015GL064899.

Miyakoda, K., G. D. Hembree, R. F. Strickler, and I. Shulman, 1972: Cumulative results of extended forecast experiments I. Model performance for winter cases. *Mon. Wea. Rev.*, **100**, 836–855, doi:10.1175/JCLI-D-16-0063.1.

Mo, K. C., and R. W. Higgins, 1998: The Pacific–South American modes and tropical convection during the Southern Hemisphere winter. *Mon. Wea. Rev.*, **126**, 1581–1598, doi:10.1175/ 1520-0493(1998)126,1581:TPSAMA.2.0.CO;2.

Mo, K. C., 2000: Relationships between interdecadal variability in the Southern Hemisphere and sea surface temperature anomalies. *J. Climate*, **13**, 3599–3610, doi:10.1175/1520-0442(2000)013,3599:RBLFVI.2.0.CO;2.

Mo, K. C., and J. N. Paegle, 2001: The Pacific-South American modes and their downstream effects. *Intl. J. Climatol.*, **21**, 1211–1229, doi:10.1002/joc.685.

Moore, A. M., and R. Kleeman, 1999: Stochastic forcing of ENSO by the intraseasonal oscillation. *J. Climate*, 12, 1199–1220.

Nakamura, T., Y. Tachibana, M. Honda, and S. Yamane, 2006: Influence of the Northern Hemisphere annular mode on ENSO by modulating westerly wind bursts. *Geophys. Res. Lett.*, **33**, L07709, doi:10.1029/2005GL025432.

Nakamura, T., Y. Tachibana, and H. Shimoda, 2007: Importance of cold and dry surges in substantiating the NAM and ENSO relationship. *Geophys. Res. Lett*., **34**, L22793, doi:10.1029/2007GL031220.

Newman, M., M. A. Alexander, and J. D. Scott, 2011: An empirical model of tropical ocean dynamics. *Climate Dyn.*, **37**, 1823, doi:10.1007/s00382-011-1034-0.

Newman, M., and Coauthors, 2016: The Pacific decadal oscillation, revisited. *J. Climate*, **29**, 4399–4427, https://doi.org/10.1175/ JCLI-D-15-0508.1.

North, G. R., T. L. Bell, R. F. Cahalan, and F. J. Moeng, 1982: Sampling errors in the estimation of empirical orthogonal functions. *Mon. Wea. Rev.*, **110**, 699–706.

Okumura, Y. M., 2013: Origins of tropical Pacific decadal variability: Role of stochastic atmospheric forcing from the South Pacific. *J. Climate*, **26**, 9791–9796, doi:10. 1175/JCLI-D-13-00448.1.

Penland, C., and P. D. Sardeshmukh, 1995: The optimal growth of tropical sea surface temperature anomalies. *J. Climate*, **8**, 1999–2024, doi:10.1175/1520-0442(1995)008<1999:TOGOTS>2.0.CO;2.

Poli, P., and Coauthors, 2016: ERA-20C: An atmospheric reanalysis of the twentieth century. *J. Climate*, **29**, 4083–4097, doi:10.1175/JCLI-D-15-0556.1.

Rayner, N. A., D. E. Parker, E. B. Horton, C. K. Folland, L. V. Alexander, D. P. Rowell, E. C. Kent, and A. Kaplan, 2003: Global analyses of sea surface temperature, sea ice, and night marine air temperature since the late nineteenth century. *J. Geophys. Res.*, **108**, 4407, doi:10.1029/2002JD002670.

Rogers, J. C., 1981: The North Pacific Oscillation. *J. Climatol.*, **1**, 39–57, doi: 10.1002/joc.3370010106.

Sardeshmukh, P. D., and B. J. Hoskins, 1988: The generation of global rotational flow by steady idealized tropical divergence. *J. Atmos. Sci.*, **45**, 1228–1251.

Smith, T. M., R. W. Reynolds, T. C. Peterson, and J. Lawrimore, 2008: Improvements to NOAA's historical merged land–ocean temperature analysis (1880–2006). *J. Climate*, **21**, 2283– 2296, doi:10.1175/2007JCLI2100.1.

Stuecker, M. F., 2018: Revisiting the Pacific Meridional Mode. *Sci. Rep.*, **8**, 3216, doi: 10.1038/s41598-018-21537-0.

Su, J., B. Xiang, B. Wang, and T. Li, 2014: Abrupt termination of the 2012 Pacific warming and its implication on ENSO prediction. *Geophys. Res. Lett.*, **41**, 9058–9064, doi:10.1002/ 2014GL062380.

Suarez, M. J., and P. S. Schopf, 1988: A delayed action oscillator for ENSO. *J. Atmos. Sci.*, **45**, 3283–3287.

Tatebe, H., Y. Imada, M. Mori, M. Kimoto, and H. Hasumi, 2013: Control of decadal and bidecadal climate variability in the tropical Pacific by the off-equatorial South Pacific Ocean. *J. Climate*, **26**, 6524–6534.

Taylor, K. E., R. J. Stouffer, and G. A. Meehl, 2012: An overview of CMIP5 and the experiment design. *Bull. Amer. Meteor. Soc.*, **93**, 485–498, doi:10.1175/BAMS-D-11-00094.1.

Thomas, E. E., and D. J. Vimont, 2016: Modeling the mechanisms of linear and nonlinear ENSO responses to the Pacific meridional mode. *J. Climate*, **29**, 8745–8761, doi:10.1175/JCLI-D-16-0090.1.

Thompson, C. J., and D. S. Battisti, 2000: A linear stochastic dynamical model of ENSO. Part I: Model development. *J. Climate*, **13**, 2818–2832.

Thompson, C. J., and D. S. Battisti, 2001: A linear stochastic dynamical model of ENSO. Part II: analysis. *J. Climate*, **14**, 445–466.

Torrence, C., and G. P. Compo, 1998: A practical guide to wavelet analysis. *Bull. Amer. Meteor. Soc.*, **79**, 61–78, doi:10.1175/1520-0477(1998)079⟨0061:APGTWA⟩2.0.CO;2.

Trenberth, K. E., G. W. Branstator, D. Karoly, A. Kumar, N.-C. Lau, and C. Ropelewski, 1998: Progress during TOGA in understanding and modelling global teleconnections associated with tropical sea surface temperatures. *J. Geophys. Res.*, **103**, 14 291–14 324.

Trenberth, K. E., and L. Smith, 2009: Variations in the three-dimensional structure of the atmospheric circulation with different flavors of El Niño. *J. Climate*, **22**, 2978– 2991, doi:10.1175/2008JCLI2691.1.

van Loon, H., and D. J. Shea, 1985: The Southern Oscillation. Part IV: The precursors south of 158Stothe extremes of the oscillation. *Mon. Wea. Rev.*, **113**, 2063–2074.

Vecchi, G. A., and D. E. Harrison, 2000: Tropical Pacific sea surface temperature anomalies, El Niño, and equatorial westerly wind events. *J. Climate*, 13, 1814–1830, doi:10.1175/ 1520-0442(2000)013,1814:TPSSTA.2.0.CO;2.

Vimont, D. J., D. S. Battisti, and A. C. Hirst, 2001: Footprinting: A seasonal connection between the tropics and mid-latitudes. *Geophys. Res. Lett.*, **28**, 3923–3926.

Vimont, D. J., D. S. Battisti, and A. C. Hirst, 2002: Pacific interannual and interdecadal equatorial variability in a 1000-yr simulation of the CSIRO coupled general circulation model. *J. Climate*, **15**, 160–178.

Vimont, D. J., J. M. Wallace, and S. Battisti, 2003a: The seasonal footprinting mechanism in the Pacific: Implications for ENSO. *J. Climate*, **16**, 2668–2675.

Vimont, D. J., J. M. Wallace, and S. Battisti, 2003b: The seasonal footprinting mechanism in the CSIRO general circulation models. *J. Climate*, **16**, 2653–2667.

Vimont, D. J., M. Alexander, and A. Fontaine, 2009: Midlatitude excitation of tropical variability in the Pacific: The role of thermodynamic coupling and seasonality. *J. Climate*, **22**, 518–534, doi: 10.1175/2008JCLI2220.1.

Vimont, D. J., M. Alexander, and M. Newman, 2014: Optimal growth of central and East Pacific ENSO events. *Geophys. Res. Lett.*, **41**, 4027–4034, doi: 10.1002/2014GL059997.

Wallace, J. M., and D. S. Gutzler, 1981: Teleconnections in the geopotential height field during the Northern Hemisphere winter. *Mon. Wea. Rev.*, **109**, 784–812, doi:10.1175/ 1520-0493(1981)109,0784:TITGHF.2.0.CO;2.

Weng, H., S. K. Behera, and T. Yamagata, 2009: Anomalous winter climate conditions in the Pacific rim during recent El Niño Modoki and El Niño events. *Climate Dyn.*, **32**, 663–674, doi: 10.1007/s00382-008-0394-6.

Wilks, D. S., 2006: Statistical Methods in the Atmospheric Sciences. 2d ed., Elsevier Inc., 627 pp.

Xie, S.-P., and S. G. H. Philander, 1994: A coupled ocean-atmosphere model of relevance to the ITCZ in the eastern Pacific. *Tellus*, **46**, 340–350, doi:10.1034/j.1600-0870.1994. t01-1-00001.x.

Yeh, S.-W., J.-S. Kug, B. Dewitte, M.-H. Kwon, B. Kirtman, and F.-F. Jin, 2009: El Niño in a changing climate. *Nature*, **461**, 511–514, doi:10.1038/nature08316.

You, Y., and J. C. Furtado, 2017: The role of South Pacific atmospheric variability in the development of different types of ENSO. *Geophys. Res. Lett.*, **44**, 7438–7446, doi: 10.1002/2017GL073475.

You, Y., and J. C. Furtado, 2018a: The South Pacific Meridional Mode and its role in ENSO variability and predictability. *J. Climate.*, in revision.

You, Y., and J. C. Furtado, 2018b: Relationship between South Pacific atmospheric internal variability and ENSO in the North American Multimodel Ensemble Phase-II Models. *Geophys. Res. Lett.*, in prep.

Yu, J.-Y., and S. T. Kim, 2010: Identification of Central-Pacific and Eastern-Pacific types of ENSO in CMIP3 models. *Geophys. Res. Lett.*, **37**, L15705, doi:10.1029/2010GL044082.

Yu, J.-Y., and S. T. Kim, 2011: Relationships between extratropical sea level pressure variations and the central Pacific and eastern Pacific types of ENSO. *J. Climate*, **24**, 708–720, doi:10.1175/2010JCLI3688.1.

Yu, J.-Y., Y. Zou, S. T. Kim, and T. Lee, 2012: The changing impact of El Niño on US winter temperatures. *Geophys. Res. Lett.*, **39**, L15702, doi:10.1029/2012GL052483.

Zhang, H., A. Clement, and P. DiNezio, 2014a: The South Pacific Meridional Mode: A mechanism for ENSO-like variability. *J. Climate*, **27**, 769–783, doi:10.1175/JCLI-D-13-00082.

Zhang, H., C. Deser, A. Clement, and R. Tomas, 2014b: Equatorial signatures of the Pacific meridional modes: Dependence on mean climate state. *Geophys. Res. Lett.*, **41**, 568–574, doi:10.1002/2013GL058842.

Zhao, M., and H. H. Hendon, 2009: Representation and prediction of the Indian Ocean dipole in the POAMA seasonal forecast model, *Q. J. R. Meteorol. Soc.*, **135**, 337–352, doi:10.1002/qj.370.

Zhu, J., A. Kumar, B. Huang, M. A. Balmaseda, Z.-Z. Hu, L. Marx, and J. L. Kinter III, 2016: The role of off-equatorial surface temperature anomalies in the 2014 El Niño prediction. *Sci. Rep.,* **6**, 19677, doi:10.1038/srep19677.